A Remotely Operated Hydrokinetic Turbine to Reduce the Levelized Cost of Energy of Marine Turbines

by

Armin Hamta

A Thesis submitted to the Faculty of Graduate Studies of
The University of Manitoba
in partial fulfilment of the requirements of the degree of

MASTER OF SCIENCE

Department of Mechanical and Manufacturing Engineering
The University of Manitoba
Winnipeg

Abstract

A novel hydrokinetic turbine system is proposed to address key commercialization challenges facing the marine energy industry. Challenges include addressing icing issues by eliminating equipment that pierce the water/air interface; reducing the levelized cost of energy by simplifying demanding deployment and retrieval procedures; and positioning the turbine in the water column to maximize annual power production. Results of the experimental test matrix shows successful operation of the scaled counter-torque mechanism which operates with a 20 cm diameter rotor and is stabilized from the reactive nature of two point masses located at opposite ends of a spoke connected to the nacelle. Static and dynamic analytical modeling, computer aided design, manufacturing, and experimental testing of the prototype is the methodology that validates the operation of the counter-torquing mechanism. The prototype turbine is tested in a laboratory water tunnel at Reynolds numbers of 94×10^3, 104×10^3, and 115×10^3; with the generator loads ranging from free-wheeling to 6.2 W; and available counter-torque capacity varying from 0% to 40%. The maximum power coefficient obtained during the tests is 48.3% at a rotor tip speed ratio of 4.5. This research advances the Technology Readiness Level of the proposed novel turbine system from a level one to a level four based on the U.S. Department of Energy definition for technology development.

Acknowledgements

Contents

List of Tables

List of Figures

Abbreviations

TSR   Tip Speed Ratio

HKT   Hyrdokinetic Turbine

CHTTC   Canadian Hydrokinetic Turbine Test Center

CTC   Counter Torque Capacity

PMDC   Permanent Magnet Direct Current

RPM   Revolution per Minute

EMF   Electromotive Force

IMU   Inertial Measurement Unit

TRL   Technology Readiness Level

MSOP   Maximum Safe Operating Point

CTFC   Counter Torque Flow Coefficient

CTRC   Counter Torque Rotor Coefficient

FOS   Factor of Safety

LCOE   Levelized Cost of Energy

Nomenclature

α	Turbine yaw angle in relation to mean flow
β	Buoy force distribution
$\ddot{\theta}$	Angular acceleration of support structure
$\dot{\theta}$	Angular velocity of support structure
η_g	Gearbox efficiency
η_g	Generator efficiency
$\forall_H$	Heavy buoy volume
$\forall_L$	Light buoy volume
λ	Tip speed ratio
ν	Kinematic viscosity
ω	Rotor angular velocity
ρ	Water density
ρ_H	Density of heavy buoy contents
ρ_L	Density of light buoy contents
θ	Inclination angle of support structure
A	Swept blade area
b	System's frictional coefficient
C_f^c	Counter-torque coefficient with respect to flow torque
C_p	Power coefficient
C_r^c	Counter-torque coefficient with respect to rotor torque
C_t	Torque coefficient
D_b	Largest diameter of buoy
E_a	DC generator excitation voltage
F_H	Negative buoyant force

F_L Positive buoyant force

F_T Total force to counter-torque

I Current drawn

I_m Moment of inertia of support structure

L Spoke arm length

L_b Length of buoy

P_f Power available in flow

P_r Power extracted by rotor

P_o Power output

R Applied load on generator

r Rotor radius

R_a Armature and commutator resistance

T_f Torque available in flow

T_g Torque output from gearbox

T_H Heavy buoy counter torque

T_L Light buoy counter torque

T_r Torque extracted by rotor

T_T Total counter torque

$u_c(y)$ Combined standard uncertainty

v Free stream velocity

1   Introduction

The development of a novel counter-torque mechanism for a single-rotor hydrokinetic turbine (HKT) is presented as a part of the solution to address the pressing challenges facing the application of marine energy with a particular focus on cold climate issues. These challenges are discussed in the literature [1, 2, 3, 4], and in particular from testing HKT prototypes at the Canadian Hydrokinetic Turbine Test Center (CHTTC) on the Winnipeg River in Manitoba. Experience testing HKTs in cold climates at the CHTTC is presented in Appendix A. Marine HKT challenges identified includes:

- surface ice formation that sinks floating turbines in cold climates operations;

- unoptimized positioning of the turbine in the water column, necessary for maximizing the power coefficient and avoiding surface obstructions such as debris and ice floes; and

- a high Levelized Cost of Energy (LCOE) resulting from the significant cost of deployment and retrieval procedures.

1.1   Global energy trends and marine energy potential

According to the International Energy Outlook published by the U.S. Energy Information Administration [5, 6], liquid fuels will continue to be the largest source of energy for the near future with nuclear and renewable energy undergoing the highest percentage increase for new generation. Overall energy consumption world-wide is projected to increase by 56% by the year 2040 [7]. These studies predict that based on global energy consumption trends, the use of renewable energy sources will increase from 11% in 2010 to 15% by 2040. While the major source of energy derived from liquids, such as petroleum and other fluids, will drop from 34% to 28% between 2010 and 2040. Figure 1 illustrates the amount of energy consumption estimate over the course of 50 years from 1990 based on different available energy resources predicated by these studies. In contrast, some European Union countries

have implemented policies that will see their energy generation to be obtained by more that 50% from diverse renewable source [8].
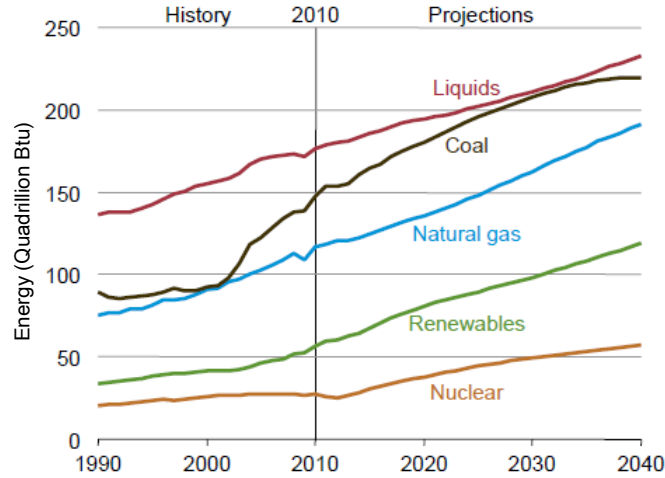
Figure 1: Global energy trends indicate a 11% to 15% rise in the consumption of renewable energy by 2010 and 2040 respectively. This sector represents the greatest increase in energy consumption compared to alternative sources [5].

Reducing the LCOE of marine energy is critical to this emerging industry. The LCOE allows for a standardized method of comparing the economic competitiveness of energy resources against each other. The factors that contribute to the cost per kilowatt includes the capital costs, fuel costs, fixed and variable operations and maintenance costs, financing costs, the capacity factor, and the load utilization rate [9]. Figure 2 shows the LCOE of various energy resources as estimated in 2013 according to the World Energy Council and Bloomberg New Energy Finance, marine energy LCOE is shown to vary from $0.30 to $1.00 per kWh—such high LCOE is characteristic of an emerging technology. However, over time the cost of renewable energy technologies like solar photovoltaics and on-shore wind energy have fallen considerably due to the continued technological development and government financial incentives [10]. Note the LCOE for river marine applications may not be directly indicative of the LCOE presented in Figure 2 which includes tidal energy. It is expected that marine energy will attract similar incentives due to (1) its predictability to address base loads with renewable energy [11], and (2) the abundant river and tidal resources which can exceed the power generation needs in some counties [12, 13]. According to Gadonneix and Meyers

[10], the cost of energy generation should decrease at the same rate of its deployment cost, a trend referred to as the *experience curve* which has been observed in established renewable energy technologies. As a result, it becomes increasingly apparent that the development of an integrated deployment and operational method for HKTs is essential for the future of marine energy applications. The review of the marine literature in Section 2 reinforces this important perspective.
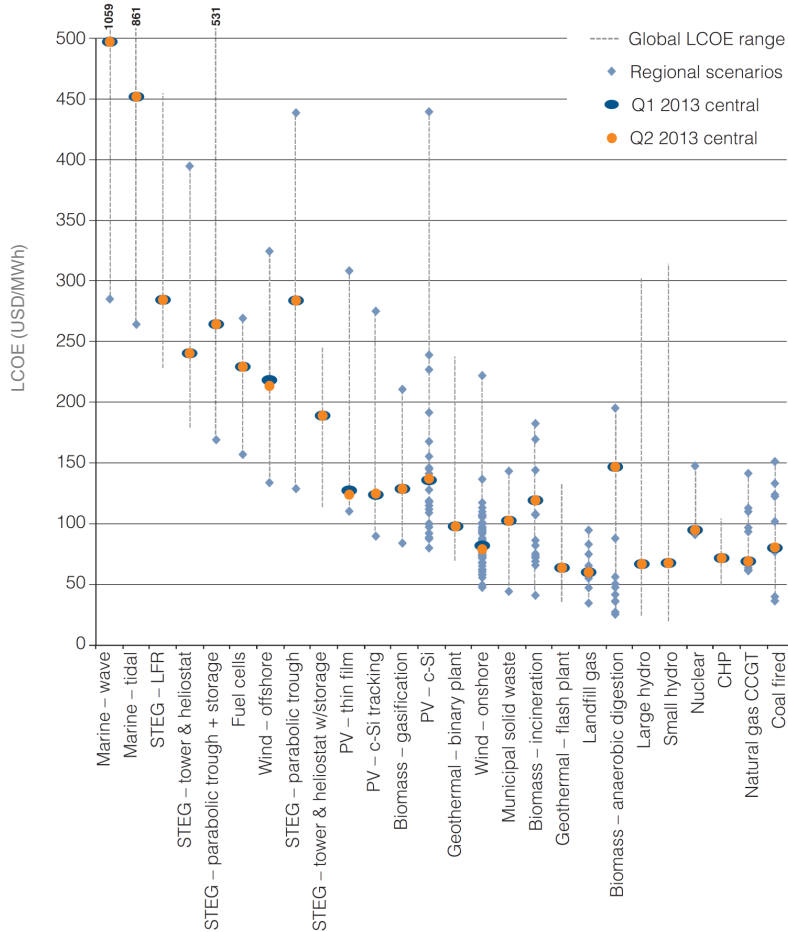
Figure 2: The LCOE in 2013 of relevant energy resources indicates the high cost of marine energy . The dash lines indicate the range of LCOE for the resource which is reinforced by specific case scenarios. The technological development and financial incentives towards an energy resource tends to decrease its LCOE [10].

One of the first stages in harnessing an energy resource is mapping its theoretical and recoverable potential. The theoretical estimation of the available river energy in a region can be calculated by measuring the change in the hydraulic head. The U.S. Environment Pro-

tection Agency applied this method to develop the U.S. National Hydrography Dataset [14]. This dataset indicates that 1,381 TWh/year is theoretically available, with 120 TWh/year being technically recoverable [14]. Note the socio-economic involvement in the technically recoverable resource is not considered herein, the dataset is based only on the technological constraints and physical limitations imposed by turbine blade size. Canada's theoretical potential assessment evaluated by National Research Council of Canada [15] consists of a series of geospatial datasets of channel geometries and 80,000 separate flow measurements across 900 measurement stations in Canada. From the compiled dataset, Canada's riverine theoretical potential is approximately 300 GW at a 95% confidence interval [13, 15]. Based on the U.S. Department of Energy Marine, Canada is ranked third in the world for marine energy conversion technologies [16, 17]. Canada has several initiatives to develop its expertise in marine energy applications, such as the Marine Renewable Energy Technology Roadmap [18] established to guide Canada on developing hydrokinetic marine technologies and applications. The roadmap calls for the development of river, tidal, and ocean energy to achieve an operating capacity of 75 MW by 2016, 250 MW by 2020, and 2000 MW by 2030 [18]. Canada aims at becoming a foremost expert in water-to-wire marine systems by 2020 [14]. As a response the CHTTC was set up to foster this effort.

With Canada's large recoverable marine potential, its focus on marine technology development presents opportunities to decrease the LCOE of marine energy and make contributions to finding new ways to address marine energy challenges.

1.2   A novel approach to address marine energy challenges

1.2.1   Specific marine challenges

Literature review from the marine energy industry and field tests conducted at the CHTTC, presented in Section 2 and Appendix A, identify three pressing HKTs challenges.

Ice formation Shore and surface ice formation can inhibit HKT deployment and dam-

age surface mounted structures. Conversely, bottom mounted turbines are capable of operating autonomously underwater, even for the duration of the icing season, with mechanical maintenance typically postponed until spring. Safety regulations can restrict on water operations when temperatures are below freezing. This aspect limits the operation of HKTs in cold climates to approximately 6 to 8 months per year while also posing a risk to the structural integrity of surface mounted turbines during spring and fall.

Turbine position in water column Power density in the water column, turbine survivability impacted by ice in cold climates, and seasonal variations of flows in river environments, point to the fact that turbines should ideally not be surface mounted, nor located at the bottom.

- The maximum power density occurs relatively close to the water surface as the maximum flow velocity is found at 20% of the water depth for riverine applications; ocean applications have the maximum power density occurring within an optimal region as well.

- Turbine components that pierce the air-water interface form ice that will sink turbine assemblies in cold climates.

- For bottom mounted turbines the power density decrease can have a significant impact on capacity factors, especially in riverine applications in winter months when flows are significantly reduced, as experienced at the CHTTC and discussed in Appendix A.3.

- Similar to wind energy, the power density is related to the velocity cubed which makes positioning the turbine at the maximum flow velocity in the water column important.

High LCOE due to deployment/retrieval HKT operating during winter months in riverine environments must be located below the waterline for survivability. Their deploy-

ment procedures can require up to a dozen experienced operators and a few boats over several days, as shown for example in Table 13 in Appendix A.3 for a bottom mounted turbine. High deployment costs not only contribute to increase the LCOE of the HKT [19, 20], but also contribute to an increase in the requirements for safety and training. For present turbine design configurations, there is simply not enough funds to cover demanding deployment and retrieval procedures: a 25 kW unit operating at a capacity factor of 60% will generate a yearly revenue of \$19,170 with a \$0.25/kW power purchase agreement.

Chapter 2 and Appendix A further detail these marine energy challenges.

1.2.2   Design considerations

HKT consists of functional components, including the rotor, the support structure, generator, power electronics, and remote monitoring systems [21]. The design of these components need to be optimized for high power generation efficiency, survivability of applied loads, and to be able to operate with a long service life and minimal maintenance [4]. However, even turbines with well designed components may not be commercially viable as they must address major water-to-wire requirements to obtain a favorable LCOE. This becomes even more apparent in cold climate applications. Given these considerations for HKT designs, the research focus herein is not on the optimization of turbine components like rotor efficiency, but rather on addressing identified marine challenges that need a new approach to reduce the currently high LCOE as identified in Figure 2 for marine energy. A new Remote Hydrokinetic Turbine (RHT) method is proposed as a viable solution for the identified challenges. The RHT consists of an integrated turbine support structure that is employed during deployment, retrieval and water-to-wire operations that may fulfill a technology gap currently preventing the growth of long-term marine energy applications—specifically those applicable to cold climates.

1.2.3   HKT in riverine environment

Before discussing the RHT system, the HKT water-to-wire riverine application is introduced as shown in Figure 3. An anchor is first installed at the river bottom [22]. A mooring line connects this anchor to a surface buoy. For bottom mounted turbines, a crane loads the turbine onto a pontoon vessel located near the shoreline. The turbine is then motored to the anchor buoy and secured in place. Alternatively, surface mounted turbines are directly deployed next to the shoreline as they utilize a pontoon structure to keep the turbine on the surface after which they are motored and secured to the anchor point. The turbine is then lowered into the water column with the use of winches after which the pontoon vessel is returned to shore. Mooring lines connected to the support structure of the bottom mounted HKT relieves the flow drag. Retrieval procedures require to reverse the procedures. Summer operations for surface mounted HKTs allow easy access for maintenance, while bottom mounted HKTs require retrieval and re-deployment increasing the LCOE. However, winter operations for surface mounted HKT is not feasible due to ice accretion on above water structures. Appendix A.3 further details the deployment and operational procedures for a large-scale bottom mounted prototype HKT tested at the CHTTC.
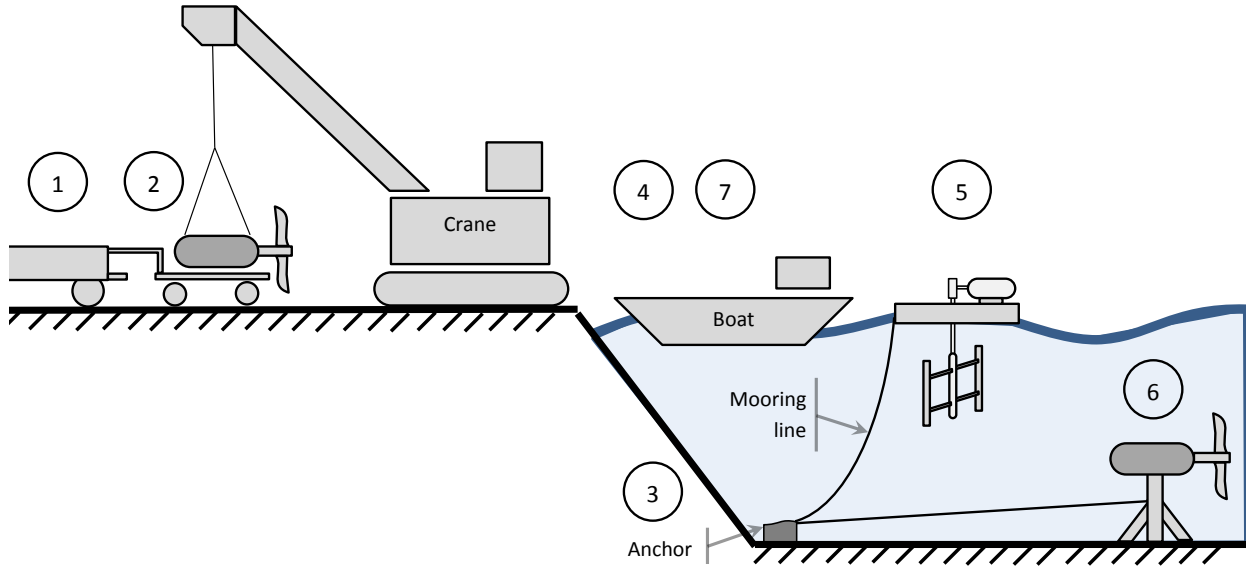
Figure 3: Applications of the HKT procedure for riverine applications involves (1) delivery of the turbine to the site location; (2) setup of the HKT; (3) fixing an anchor point; (4) deployment of the HKT in the river using a launch ramp or a crane; (5) securing HKT to the anchor for operation; (6) bottom mounted turbines are suitable for annual operation although prove to be costly for maintenance due to deployment/retrieval procedures; (7) retrieval of the turbine can be done with the use of a boat for surface turbines or a pontoon for bottom mounted HKTs. Further details are provided in Table 1

1.2.4   RHT in riverine environment

The RHT method introduced is shown in Figure 4 and utilizes:

1. A ballast in the nacelle to deploy, retrieve, and remotely position the turbine in the water column.

2. A passive counter-torquing mechanism based on Newton's third law of motion in a rotational reference frame to balance the variable generator torque (sometimes referred to as rotor torque). Two point mass buoys are located at a fixed distance from the rotor axis—a buoy with positive buoyancy (light buoy) has a constant specific density less than one, and a buoy with variable negative buoyancy (heavy buoy) that allows mass transfer in and out of the buoy to control its specific density.

   - The torque absorbed by the loaded generator inclines the point masses such that

an equal but opposite counter-torque is passively produced to establish a steady-state operating point when subject to changes in consumer power demands and in river flow velocities.

- The two buoys are designed to replace the need for the transport boat by performing a similar function. Simplification and reduction of the number of deployment procedures reduces the LCOE.

The nacelle ballast and the specific gravity of the point masses are configured to locate the turbine within the water column to control turbine power production and respond to seasonal constraints such as debris, boat traffic, and ice breakup.
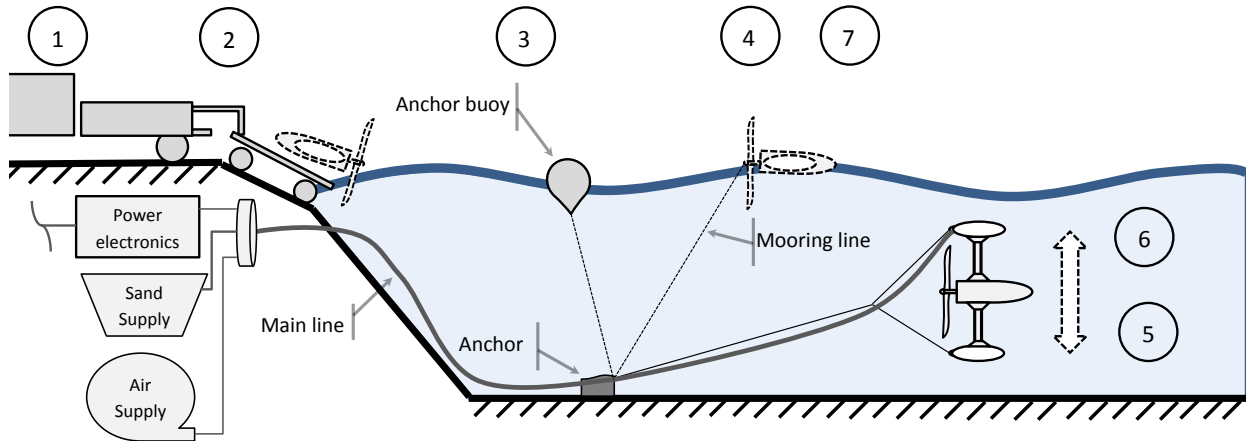
Figure 4: Proposed RHT reduces the need for on-site personnel and costly procedures the reduce the LCOE, with steps correspond to Table 1. The procedure involve: (1) delivery of the turbine to the site location; (2) setup of RHT; (3) setting the anchor point in the river while temporarily attaching an anchor buoy for securing the mooring line; (4) floating the RHT to the site location by pulling on the mooring line with an on-shore winch, once at the site locations the nacelle ballast is filled with water and the heavy buoy is filled with sand to counter-torque the generator torque; (5-6) summer and winter operations sees the RHT at different positions in the water column based on degree of debris and icing; (7) retrieval of the turbine is done through filling the nacelle ballast with air and disposing of the sand in the heavy buoy to reduce the overall specific density of the RHT. Further details are shown in Table 1.

As shown in Figure 4, the procedures involved in the deployment of the RHT begin with the turbine set in the water with the point mass configured for turbine transportation: the two buoys are designed to act as a pontoon vessel to eliminate the need for a pontoon boat

to transport the turbine to the anchor buoy. This configuration is accomplished by setting the specific density of the heavy buoy to be approximately equal to the light buoy such that the RHT is aligned horizontally when floating during transport. During this phase, the turbine brake is activated for safety and turbine stability. The turbine's anchor is set on the river bottom and temporarily attached to the anchor buoy on the surface for accessing the mooring line. The anchor supports the RHT by taking all of the drag connected through the mooring line. It also acts as a relay point for the RHT main line coming to shore. The main line consists of (1) a marine power cable, (2) a compressed air line for adjusting the nacelle ballast tank, (3) optionally a supply line to deliver sand to the heavy buoy, and (4) an instrumentation line for monitoring the operation of the turbine and counter-torque mechanism. After the mooring line and the main line are secured to the RHT by the shoreline, the flow is allowed to take the turbine to its equilibrium position on the river surface. The central ballast tank is then remotely filled with water allowing the turbine to descend into the water column. At the optimal position in the water column the counter-torque system is activated by filling the heavy buoy with sand causing it to align vertically with the light buoy. The light buoy point mass fabricated of closed cell insulator foam has a density 30 times less than that of water [23]. The heavy buoy point mass is filled with sand-air mixture using the main line or manually by using a boat [24], while adjusting the nacelle buoyancy keeping the turbine in the desired position in the water column. The air which delivers the sand to the heavy buoy is then evacuated through a check-valve to prevent excessive pressure build-up.

During operation the torque induced by the flow causes the point masses to incline with respect to the vertical axis which increases the moment arm of the point masses inducing a counter-torque reaction. This reactive system will always produce the required balancing torque necessary to stabilize the generator torque given the required minimum amount of sand is present in the heavy buoy. The passive counter-torque control can account for the seasonal variations of applied loads and velocity variations.

Resurfacing procedures involves breaking the rotor followed by the disposal of the locally obtained sand into the water; the heavy buoy cavity is then filled with air until it approaches the same density as the light buoy. With both the buoy cavities at the same density, the system inclines horizontally after which the central nacelle ballast tank is filled with air and the turbine resurfaces. Retrieval of the turbine can be done either with a small boat which removes the main line and drags the RHT to shore for docking, or by using an additional line connected from shore directly to the RHT which pulls the floating RHT back to shore.

1.2.5   Comparison of HKT and RHT for deployment, retrieval, and operation for riverine applications

Description of deployment techniques for HKT and their costs are limited in the literature due to their confidentiality and the infancy of the marine energy industry. This is evident from the recent deployment of the first large scale commercial tidal turbine in June 2003 by Marine Current Turbines Ltd [20]. The 300 kW Seaflow turbine presented the first large scale mono-pile deployment in the Bristol Channel off North Devon, England [20]. Given the limited literature available, the field experience for deploying HKTs at the CHTTC gives an opportunity to establish a basis for deployment procedures for HKTs in riverine environments. Table 1 outlines several key stages of a typical HKT life-cycle in comparison to the proposed RHT method.

Table 1: RHT application compared to current HKT procedures. Labels correspond to Figures 3 and 4.

Order	Operation	Current technique	Proposed technique
1	Delivery	Turbine delivery requires the use of large trailers or special shipping containers for their support structure or pontoon boat.	Turbine delivered on a flat bed trailer, reduced shipping needs due to lack of support structure and the integrated generator within the nacelle.
2	Setup	Assembly of the turbine at site location typically requires extensive power tools, lifting cranes, and power electronics before deployment.	No assembly required for riverine turbine, pre-diagnostic tests should be performed.
3	Site Preparation	Anchors located on the river bottom can be employed for both surface mounted turbines and bottom mounted turbines. A anchor buoy is fixed to the mooring line to ensure line will always have one point accessible on the river surface	A bottom mounted anchor is set to take all of the drag load on the mooring line; kitting the turbine while also acting as a relay point for the main line which supplies the power, sand, compressed air, and instrumentation line between the turbine and the shore.
4	Deployment	A crane or large lifting loader is typically required for large HKTs. Boats are typically employed for small scale surface deployments while pontoons are used for larger bottom mounted turbines.	The turbine deployment requires a launching site and possibly one delivery boat depending on the distance between the launching site and the anchoring locations.

Order	Operation	Current technique	RHT
5	Operation and maintenance (summer)	Surface mounted turbine's operation poses minimal issues with easy maintenance due to surface access. Bottom mounted turbines are not maintainable without a retrieval and redeployment procedure which can contribute significantly to the LCOE.	Operation of the turbine is similar to a bottom mounted turbine which is concealed underwater with the benefit of a surface mounted access since it can be retrieved remotely by simply changing the buoyancy of the ballast tanks and emptying the content's of the heavy buoy.
6	Operation and maintenance (winter)	Winter operation for surface mounted turbines is typically not possible due to ice accretion at the water-to-air interface of the turbine; bottom mounted turbines operate as they are completely submerged underwater although maintenance is challenging due to cold climate conditions as experienced by Bibeau et al. in [22] and [25].	During operation the turbine is submerged underwater which allows it to eliminate ice accretion and avoid run-off ice and debris. Maintenance should be delayed if possible until spring.
7	Retrieval	Surface mounted retrieval are done by using either a vessel to transport the HKT from the mooring line connection to shore or by using a winch from shore to pull the turbine. Bottom mounted turbines typically require a pontoon vessel for withstanding the high drag loads from the flow and provide enough space for the turbine transport.	The retrieval procedure involves preparing the buoys for transport by adjusting their specific density to be almost equal and filling the nacelle ballast with air to surface the turbine. A boat would transport the floating RHT to shore or an additional line connecting the RHT to shore can be used to pull the turbine to shore.

1.3   Objectives

The objectives of this research in marine energy are:

LCOE Reduce the LCOE of marine energy by combining the deployment, retrieval, and water-to-wire operations using the proposed RHT system to:

- position turbines in the water column to maximize power production;

- avoid debris/ice often located close to the water surface; and

- reduce deployment/retrieval costs such that the LCOE can become competitive with alternative renewable energy resources.

System dynamics Investigate the performance of the proposed RHT counter-torque mechanism through analytical derivation of the governing equations, evaluation of the dynamic stability, and optimal configuration of a scaled prototype.

Testing Design and fabricate a passive counter-torquing, tethered, single-rotor, scaled, horizontal-axis HKT. Perform experimental tests to validate the passive counter-torquing mechanism and evaluate its performance metrics.

Scaling Establish a set of scaling parameters for large-scale applications of the counter-torque mechanism used in the RHT system.

1.4   Contribution and impact

Research contributions made towards marine renewables is the development of a novel passive counter-torque mechanism for a new RHT system. This system increases the technology readiness level from a TRL-1, where the basic principles of the concept is observed and reported, to a TRL-4, where the validation of the RHT concept is performed in a laboratory environment and results reported. These contributions may impact the marine energy industry by addressing key challenges that are inhibiting the commercialization of HKT due

to high LCOE. Specific contributions include:

- **Development** of a novel RHT to address marine technology challenges resulting in a high LCOE;

- **Validating** a passive counter-torque stability mechanism for remotely operating the single rotor tethered RHT; and

- **Identifying** the scaling parameters relevant to the large scale operation of a RHT.

These contributions are aimed to accelerate the implementation of HKTs for river and tidal applications by decreasing the LCOE of marine energy applications. The proposed RHT design accomplishes this by providing anticipated lower the costs for deployment and maintenance procedures, improved personnel safety, maximization of the power generated in any season, and avoid seasonal debris. The proposed RHT is well adapted to distributive generation for off-grid communities to harness marine energy.

2 Literature review

Literature review provides the supporting argument for the challenges identified in Section 1 and the incentive for addressing these challenges. This is accomplished through a review on the following areas:

Hydrokinetic turbine development Harnessing power from the kinetic energy of water has matured thanks in part to the historical development of wind energy and the recent renewable incentives establish globally within the past several decades.

Challenges of riverine turbines Review of the literature on the identified challenges of:

- icing and cold climate perturbations;

- HKT positioning in the water column; and the

- impact on the levelized cost of energy.

Hydrokinetic resource assessment Assessments into the resource potential of hydrokinetic energy provides the incentive for further developing technology to deal with the presented challenges.

Hydrokinetic turbine technology Comparing existing and derived technologies from alternative industries, such as oil platforms and wind turbines, gives a scope for further development and research.

Anchoring techniques Current methods of anchoring HKTs for riverine sites and the difficulties that are encountered.

Background theory into the design and analytical calculations preformed in this project are conducted through known fundamental equations in the fields of dynamics, fluid mechanics, and electromechanics. These equations are reviewed in Appendix B.1.

2.1 Hydrokinetic turbine development

Development of hydrokinetic technologies is inspired by hydro-dams and wind turbines, both of which are mature technologies [21]. All of the technologies developed operate under the same fundamental principles, namely harnessing the flow's kinetic energy by first converting it to mechanical motion which is then transformed to electrical energy by an electromechanical machine [26]. The primary conversion of the fluid's kinetic energy is accomplished by either, traditional turbines which are classified based on their orientation with respect to the mean flow or alternative non-traditional methods. Traditional methods include:

- horizontal axis turbine,

- vertical axis turbine,

- cross-stream turbine, and

- gravitational vortex induced turbines.

Non-traditional methods employ involve one of the following:

- flutter vane,

- piezoelectric systems,

- vortex induced vibrations,

- oscillating airfoils, and

- drag sails.

The various systems have inherent uncertainties in their delivery, deployment, and maintenance procedures that present novel challenges unlike those seen in similar matured industries, such as wind turbines or oil platforms [3]. The design of wind turbines components have been adopted by HKTs due to the similarity of both of them extracting the kinetic energy of a fluid flow [27]. HKT components are illustrated in Figure 5 in which the term turbine is used to represent any harnessing technique [28]:

Turbine A method of converting the kinetic energy of the flow to a linear or rotary motion that can be transformed to electrical energy through a generator.

Nacelle Houses the generator, and in certain designs the drive train

Drive train Consists of all of the mechanical components that modify the rotary or linear motion of the turbine to a usable form for the generator, including:

- shafts,

- gearbox (optional),

- coupling, and

- mechanical brake.

Yawing mechanism (Optional) Aligns the turbine with respect to the flow direction to maximize the power extraction.

Support structure The foundation and structural components which fix the system in one location given the applied loads from the fluid flow and the applied electrical loads.
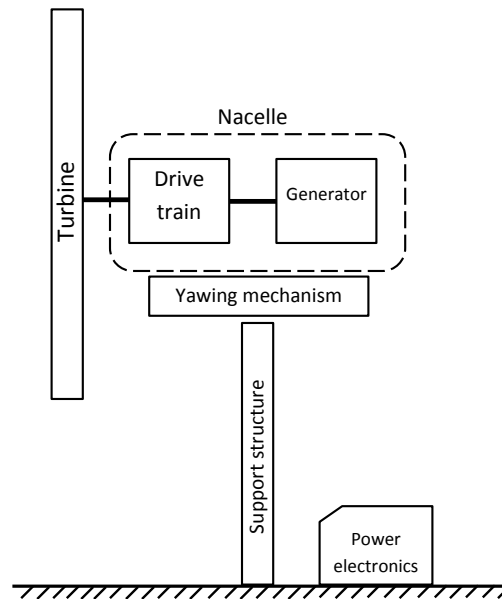
Figure 5: Major design components of wind turbines and HKTs

The practice of capturing the kinetic energy of the wind has been around since 200 B.C.. The first windmills were found near the Persian-Afghan boarder [29]. From there, the development of windmill technology evolved during the 19th century when the United States employed a mass number of them for extracting water from wells. Then in 1891 Paul LaCour, a professor at the Askov School of Engineering in Denmark, performed the first experimental tests for generating electricity using a wind turbine which marked a new era in renewable technology [30]. During the 1980's further research and development into the technology led to a reduction in its levelized cost from \$0.91/kWh to \$0.06/kWh in current Canadian dollar currency [31] [32].

Coupled alongside the use of wind energy, marine hydro energy has also been historically employed since 202 B.C. during the Han Dynasty in China [11]. Similar to wind energy, developments in the 19th century brought hydro power to its modern state from the work employed by James Francis in 1849, Viktor Kaplan in 1913, and Lester Allen Pelton in the 1870's. All of which have made significant contributions that still have an impact today as seen from the Francis turbine, the Pelton wheel, and the Kaplan turbine [11]. The development of hydrokinetic energy emerged from a combination of hydro and wind energy in the 1970's and picked up in the 1990's when countries with marine resources began to see the potential in harnessing hydrokinetic energy [33]. The top contributing countries to the progress of this technology, in order of the number systems developed, include the United Kingdom, the United States, Canada, and Norway [16]. Primary areas of research are being conducted in ocean tide, ocean wave, and marine current [16]. Ocean tide technology can appear in several forms, from building dams near the shore that collect water during the changes in the tide and then releasing the water through turbines, to placing vertical or horizontal turbines directly in the water and generating power from the flood and ebb of the tide. Ocean wave involves the placement of turbines offshore where stronger flow metrics can be found and higher power outputs can be generated [16].

2.2   Challenges of riverine turbines

The substantial resource potential available in riverine environments, investigated in Section 2.3, provides incentive for addressing the challenges of:

- damaged incurred to HKTs due to surface ice formation on the turbine and its structural support;

- optimizing the positioning of the HKT in the water column to maximize the power generated; and

- reducing the impact of deployment and retrieval procedures to the LCOE.

Experience from the CHTTC, described in Appendix A, provides insight into these challenges along with literature.

2.2.1   Icing and winter perturbation

One of the main challenges in cold climate conditions is the reduction in the power output during winter due to icing conditions and a reduced flow velocity. Investigating the annual reports from the Lake of the Woods Control Board for the Seven Sisters generating station [34] indicates an approximate percent difference between the high summer inflow rate and lower winter inflow rate of 80% for 2014, 33% for 2013, 35% for 2012, and 60% for 2011. This drop in flow rate is consistent with other locations along the Winnipeg River in Manitoba [34] which results in a significant loss in the power output during winter months. The power output is a function of the flow velocity cubed which is reviewed in Appendix B.1. Winter operation of hydrokinetic turbines become hindered additionally by ice accretion on components above the water surface. Ice accretion on the surface is dependent on nine parameters which are illustrated in Figure 6 [35]. Birjandi et al. [36] were able to identify potential hydrokinetic turbine sites by observing the patterns in the ice formation and seasonal water velocities which creates openings in the surface ice during winter for potential

sites. Figure 7 illustrates one such opening on the Winnipeg River.
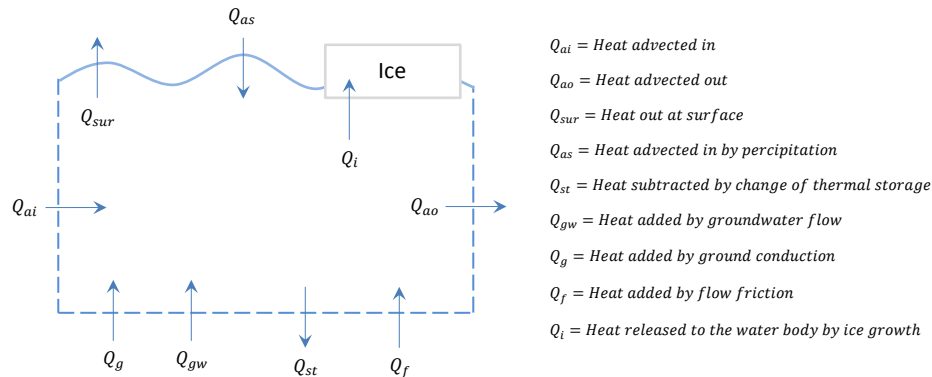
Figure 6: Ice formation parameters include the water velocity and its energy cascade down to small Kolmogorov scale, dissipating into heat [35].

Figure 7: Even during temperature as low as $-40°C$ the Winnipeg river contains surface ice openings which have the potential for surface mounted hydrokinetic turbines.

One alternative to dealing with icing difficulties is to remove the turbine from the flow at the onset of winter [37]. This is necessary for surface mounted turbines on the Yukon River since ice sheets 1 to 2.5 m thick develop and can encase the turbine in ice causing significant structural damage [37]. Johnson and Pride [1] discuss the parameters of the river environment that may affect the performance of a marine turbines. They mention that the interaction of icing does not only occur on the surface but also underneath as supercooled

water during the start of winter can turn into frazil ice and potentially inhibit the operation of a submerged turbine. Kassam [2] and Bibeau et al. [25] present one of the only documented cases regarding the impact of icing on the performance of surface mounted HKTs. They examine the damage that surface ice accretion can have on a research vessel fitted with a vertical axis 5 kW lift based hydrokinetic turbine. The turbine was tested near the Pointe du Bois generating station where the air temperature was recorded as low as $-40°C$. The constantly rotating motion of the turbine shaft prevented ice accretion allowing it to operate even at low temperatures. The only case of stalling occurred when ice built up from the inner walls of the pontoon finally reached the turbine's shaft encasing it in ice. Kassam [2] identifies that regular maintenance and ice removal is necessary for the operation of surface mounted turbines in conditions where the flow is fast enough to prevent surface ice sheets yet cold enough for it to accumulate on floating structures. Other issues encountered with turbine deployment and operation during cold weather include:

- gearbox issues due to the low temperatures reducing its viscosity;

- excess loading on anchor lines that pass through the water-air interface since they provide sites for ice accretion; and

- a reduced efficiency for maintenance procedures due to certain tasks requiring direct hand contact in cold weather.

Bibeau et al. [25] indicates that ideal placement of the HKT for riverine applications is below the water surface to avoid surface icing. Anchoring techniques include either a bottom mounted pile which has a large impact on the LCOE or ideally kitted mooring which is implemented in this thesis. Submerging the HKT under the water surface introduces an additional parameter dealing with its optimal positioning in the water column.

2.2.2   HKT positioning in the water column

The optimal positioning for a marine turbine in the water column is established through a site assessment similar to wind turbines [38]. An optimization process must be carried out to account for the factors influencing the power production such as:

- the power output's cubic relationship with the flow velocity;

- the distance between the location of power generation and consumption; and

- the capital cost required for reinforcing the infrastructure of the turbine.

White [39] indicates that open-channel flows have a maximum flow velocity located approximately 20% below the fluid surface. Wider channels lead to the flow profile approaching a more logarithmic shape which moves the maximum flow velocity closer to the surface of the channel. This is in agreement with field experiments conducted by Cheng and Gartner [40] in which they showed that the maximum flow velocity of the San Joaquin River is located 16% below the water surface and is 10% higher than the velocity at the surface. Cheng and Gartner [40] used an acoustic Doppler current profiler along with a modified profiler called a BoogieDopp to measure the flow in discrete cells along the water column. Similar results using an acoustic Doppler current profiler used at the CHTTC is presented in Figure 8.

As a consequence of the velocity profile of the flow, the operation of a bottom mounted turbine during winter at the CHTTC can result in stalling due to the lower flow velocities found near the bottom of the channel. Surface mounted turbines can be placed closer to the optimal flow region at the risk of sinking during winter months. One costly alternative for optimal positioning in the water column is a bottom mounted support pile which can allow a HKT to traverse the water column; this is implemented in the HKTs Seaflow, SeaGen, and the NREL reference turbine [4, 41, 42]. To avoid costs associated with a pile mount installation, a tethered HKT design can be made to have a variable buoyancy altering its location in the water column. This combines the accessibility of a surface mounted turbine and the ice/debris avoidance of a bottom mounted turbine. Hunt [43] employed this technique in
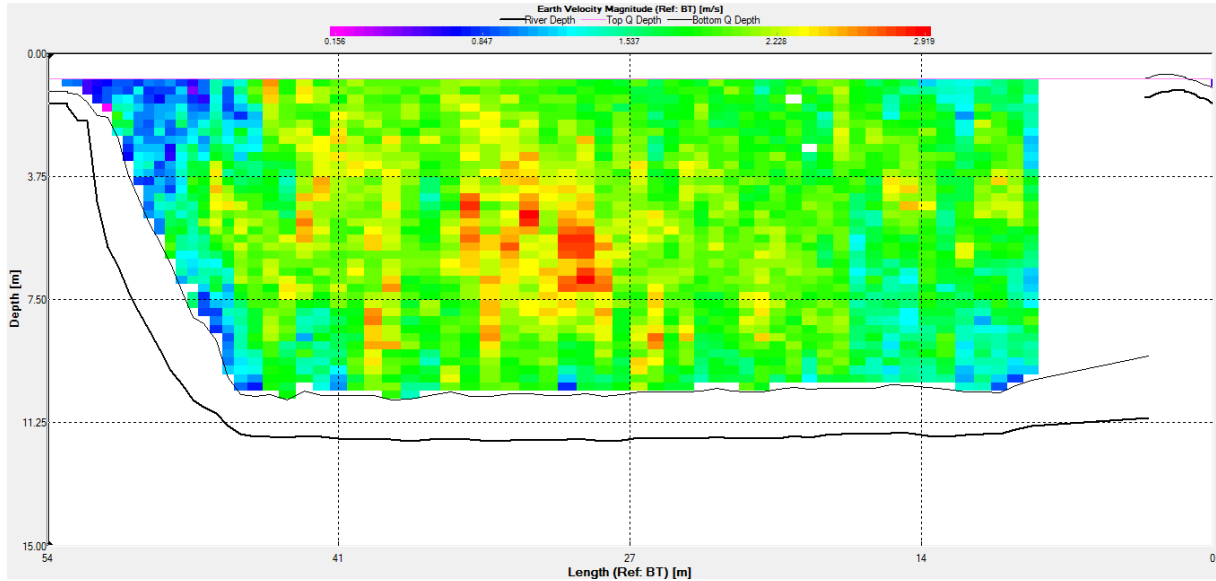
Figure 8: Velocity flow profile taken by Amir Birjandi at the CHTTC. Narrower channel walls results in the maximum flow velocity approaching the middle of the channel, similar to a pipe.

which a tethered hydrokinetic turbine's Tip Speed Ratio (TSR) is controlled by changing its position in the water column through the use of buoyant buoys. This design takes advantage of the flow's velocity profile and uses it as a design parameter for controlling the generator's output power. Coiro et al. [44] also use buoyant shells for controlling the position of their dual rotor tethered horizontal axis HKT in the water column. The variability of its position allows for the turbine to be placed lower in the channel during spring run-off and icing conditions for longer operational period throughout the year. The use of a dual rotor employed by Coiro et al. [44] requires balancing the torque on both rotor shafts to keep the system level during operation. The single rotor tethered system proposed by the RHT would eliminate this challenge with a passive counter-torque mechanism. In conjunction with the counter-torque mechanism, the proposed RHT utilizes a buoyant cavity to also control its positioning in the water column. Experience with a bottom mounted turbine at the CHTTC proved that proper positioning of the turbine in the velocity profile is important with respect to its power production. Appendix A.3 covers the details pertaining to the turbine deployment and positioning.

2.2.3   Levelized cost of energy

The LCOE provides a means of comparing different energy resource technologies by normalizing the total cost of the entire project life-cycle by the kilowatt hour output energy [9]. Due to the limited number of marine turbine demonstrations and confidentiality of their results, the analysis of the turbines' economics is limited. Nevertheless, in order to promote the technological development of hydrokinetic turbines, knowledge and quantitative values of the LCOE is necessary. This section examines the potential financial cost associated with the development and operation of two reference marine turbines found in the Methodology for Design and Economic Analysis of Marine Energy Conversion Technologies, produced by Sandia National Laboratories for the U.S. Department of Energy in 2014 [3]. Due to the wide range of unknown parameters that can influence the life cycle cost of a marine turbine, these reference models do not represent the final cost model; instead they are to be taken as drivers for guiding the design and direction of HKT technology development. The assumptions for the LCOE include [19]:

- a constant energy output,

- a constant annual operation and maintenance, and

- no financing.

Equation 2 presents the LCOE with the associated parameters presented by Short et al. [19]:

Total Life Cycle Cost (TLCC) Represents the initial costs associated with design, planning, fabrication, deployment and project management of the turbine.

Initial Investment (I) Initial investment for the project.

Operation and maintenance (O&M) All of the costs associated with operating the turbine.

Annual energy production (Q) Represents the delivered grid connection energy after

accounting for turbine availability.

Discount rate (d) The time value of money used to account for the inherent risk of the investment.

$$TLCC = I + \sum_{n=1}^{N} \frac{O\&M_n}{(1+d)^n} \tag{1}$$

$$LCOE = \frac{TLCC}{\sum_{n=1}^{N} \frac{Q_n}{(1+d)^n}} \tag{2}$$

The review of the analysis conducted by Neary et al. [3] will be broken down into the different life cycle costs associated with deployment and maintenance of the two turbine projects. It should be noted that the assumption made for constant maintenance costs and constant energy output is not a complete representation of the actual HKT performance since the flow velocities change annually and different climate conditions require different maintenance procedures.

2.2.3.1   Reference model one

The first reference model is a dual rotor variable-speed, variable-pitch, bottom mounted tidal turbine inspired by the first commercially grid connected marine turbine SeaGen [4]. This turbine model, illustrated in Figure 9, is selected to quantify the capital investment necessary for the installation cost of the support structure which consists of a pile mount embedded on the sea floor. A primary goal of this design model was to use standard protocols and off-the-shelf items to minimize additional engineering work and costs associated with custom designed components.

Figure 10 illustrates the cost breakdown of a 10 turbine array of the reference model one. The capital expenditure for the deployment of the turbine array is estimated to be $ 6, 190/kW$.
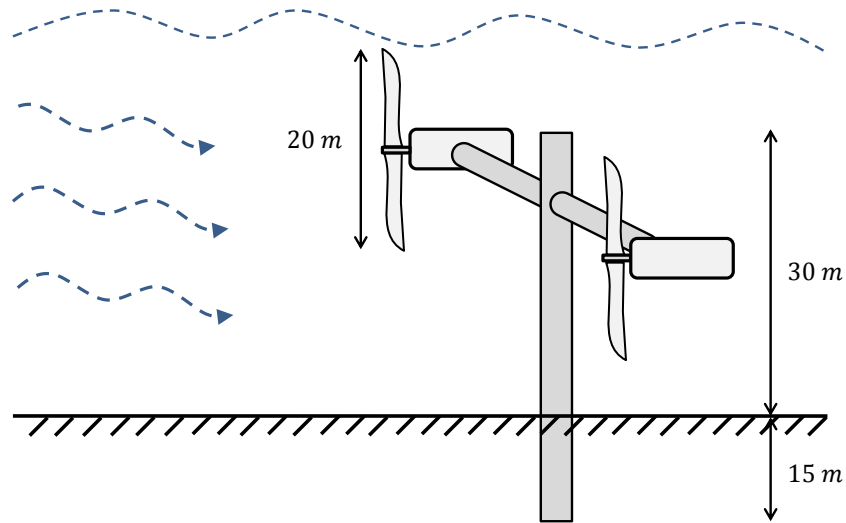
Figure 9: Reference model one is deployed and retrieved by a custom moon-pool vessel. A cross brace connecting the two turbine rotors together is hoisted up and down from the vessel onto the pile mount underwater [3].

The cost per single turbine is $ 31,900/kW$ (all costs in current year currency) [3]. The capital investment represents 70% of the total levelized cost while the operation and maintenance represents 30% of the total levelized cost.
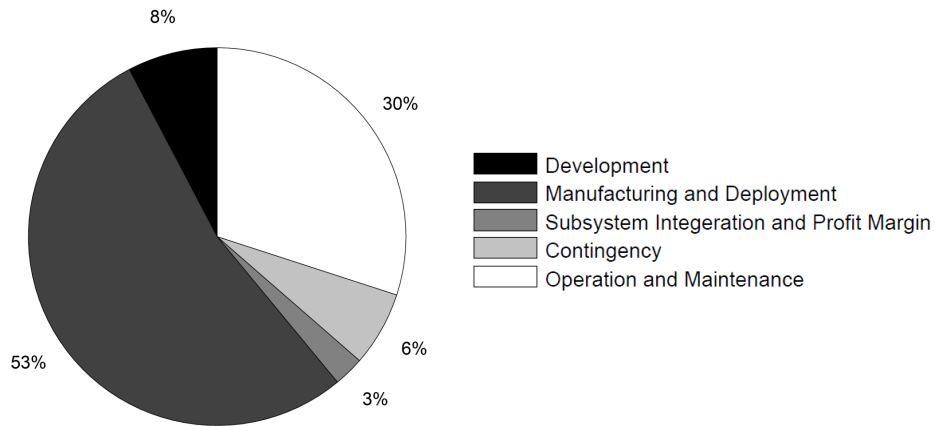
Figure 10: The components of the 40.7 $cents/kWh$ LCOE for ten turbine units of the reference model one, indicates that the manufacturing-deployment and operation-maintenance present the largest contributing component [3].

From the capital investment distribution shown in Figure 11 the drive train represents the greatest single cost, yet the sections representing the turbine support structure and the cost associated with it: infrastructure, device structural components, and installation together

represent 51.9% of the total capital. This is a result of the 45 m tall pile tower supporting the turbine, and the \$ 13 million to \$ 16 million custom moon-pool vessel with a crew of 20 for deployment and servicing [3]. In addition, to mitigate the shock waves generated in the water during hammering of the pile support structure a special sound attenuation system may be required [3]. Neary et al. [3] shows that the piles installation costs \$ 5,500/kW which is 65% of the total installation cost.
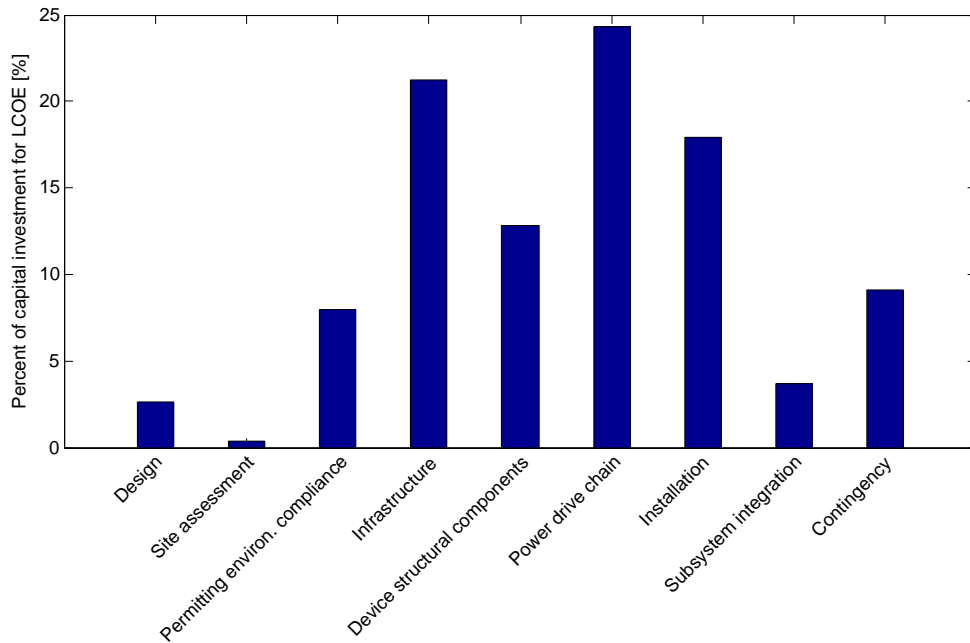
Figure 11: A breakdown of the capital investment of reference model one indicates the costs associated with civil engineering work (infrastructure, device structural components, and installation) is greater than the cost of the mechanical engineering work (power drive train and subsystem integration).

Research into techniques and methodologies to reduce the LCOE can be accomplished by focusing on the highest component cost. The support structure incurs 17% of the total capital for installation costs, while also contributing another 26% through decommissioning procedures of the pile mount and the turbine nacelle. Besides the dedicated moon-pool vessel, no other single component contributes as much as the pile mount for this turbine design. The annual energy production calculated from the flow frequency distribution and the turbine's power curve produces a capacity factor of 30% which when coupled with the

capital return and operational costs, gives a LCOE of approximately \$ $2,140/MWh$ (in 2014 dollars) for a single turbine unit [3]. Currently this is more than ten times the levelized cost for an off-shore wind turbine with a 38% capacity factor, and twenty-eight times larger than a land based wind turbine with a 36% capacity factor [9]. The cost of a ten unit array of the reference model reduces to \$ $400/MWh$ per turbine. Historically off-shore wind turbines were in a similar economic predicament 30 years ago as marine turbines are currently in now. The LCOE of off-shore wind turbines has dropped to $1/3^{rd}$ of that with a similar reduction in cost being expected for marine turbines over the next decade [45]. The methodology for reducing marine LCOE has been laid out by Taylor et al. [18], where they identify technological developments, government incentives, stakeholders investment, and collaboration between governments, universities, and industry to facilitate the development of hydrokinetic turbines.

It should be noted that economic analysis of any turbine model cannot be linearly scaled to different marine environments. Reference model one is utilized as an indicator of the impact of deployment costs to the overall LCOE. A riverine HKT may in fact incur higher costs due to the same demanding requirements as tidal turbines yet with lower overall power outputs as experienced at the CHTTC. Reference model two investigates the benefits of using a cable mount with a floating surface turbine and its reduction in deployment/infrastructure costs.

2.2.3.2   Reference model two

The second reference model turbine, illustrated in Figure 12, uses two counter-rotating turbines that are attached to a floating support structure. A 1:6 nominal scaled turbine has been constructed and tested by the Center for Oceans Renewable Energy at the University of New Hampshire [46]. The design consists of two pontoons 27.5 m in length held together with three cross-braces 19 m in width. The dual vertical axis turbines are secured to the middle cross-brace which fixes the 4.8 m blades underwater. One end of the mooring cable is

attached to the support structure while the other end is fastened to an eyelet on an anchor. The LCOE for the 100 kW turbine system is presented in Figure 13.
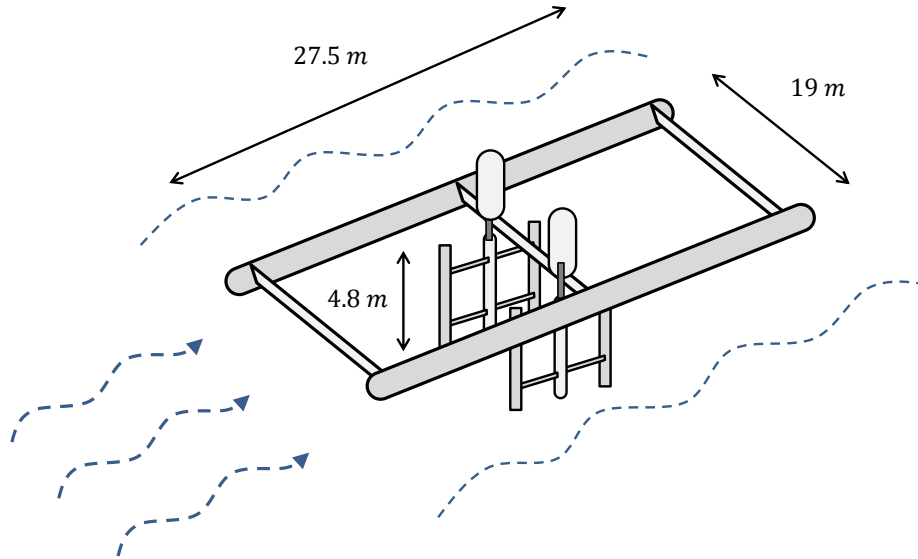
Figure 12: Reference model two has counter-rotating rotors in order to balance the torque generated. This can cause potential problems in the case that one turbine is not operating at the same capacity as the other.
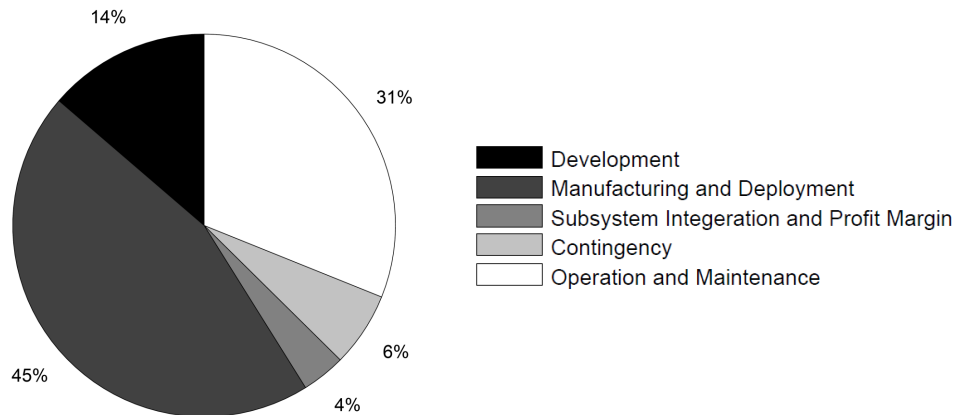
Figure 13: Levelized cost of energy distribution for an array of ten units of the reference two model. Manufacturing and deployment reduction is a target for reducing the cost of every turbine investigated by Neary et al. [3].

Reference model two has 69% of its levelized cost arising from capital expenditure while the remaining comes from operations and maintenance. From the total capital expenditure, the manufacturing and deployment contributes the most for reference model two similar to all

of the turbines investigated by Neary et al. [3]. The floating support structure provides easy access to the generator and power electronics which are on the water surface. In addition, the turbine can be placed closer to the optimal position in the flow since it is submerged at a depth of 9.5 m underwater [47]. However, Khan et al. [26] properly notes that one of the main issues with floating surface turbines is the fact that they present obstacles for ship traffic. This is much more prominent in riverine environments where anchors can be hidden from inexperienced boat drivers and can result in accidents. In addition, the experience from Bibeau et al. [25] in winter operations at Pointe du Bois in Manitoba indicates that ice build up on the turbine structure can cause the support structure to sink. Alternatively reference model one has the capability to avoid direct ice damage but at a financial cost of its pile mount infrastructure. Figure 14 shows the break down of the maintenance costs associated with reference model two.
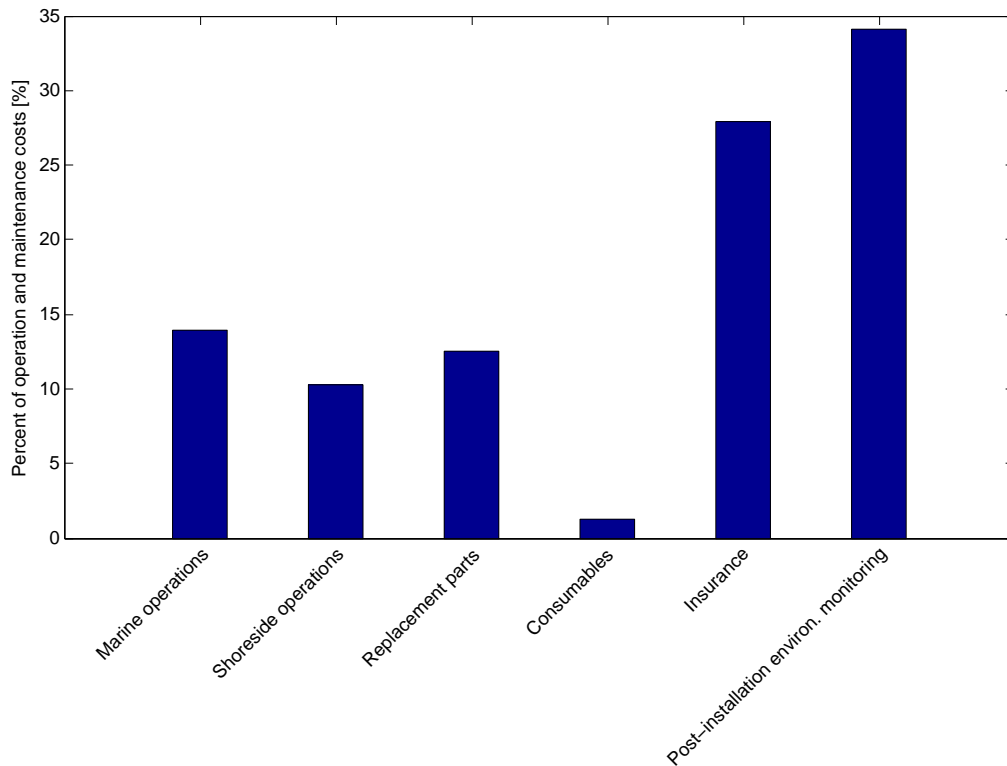
Figure 14: Operational and maintenance cost distribution for an array of 10 units of reference model two. Costs associated with the post-installation monitoring have a $+/-$ 20% error due to the large number of uncertainties [3].

It is expected that the marine and shore-side operational costs constitute only a small portion of the total maintenance costs. The post-installation environmental monitoring involves ship navigation, noise and electromagnetic interference characterization, influence on marine habitats, water quality monitoring, and the impact on fish and diving birds. Analysis of the environmental data provides the validation for the permits and licensing of the waterways being used [3]. The main driver behind its high cost is the uncertainty associated with the analysis due to the unknown impacts of the reference turbine.

The proposed RHT design adopts the benefits of having a surface access for maintenance procedures, similar to the reference model two; while being submerged during operation to avoid surface icing and debris like the reference model one design. A look into the resource assessment of marine environments provides further incentive for the RHT design.

2.3   Hydrokinetic resource assessment

The potential for hydrokinetic energy has been recognized through the implementation of resource assessments of the local marine environments in several countries [48, 49, 50, 51]. This has led to the development of incentives and programs for advancing the technological capabilities of HKTs and the experience base needed to properly operate them. A resource assessment is a primary step for investigating the density, reliability, and availability of a marine resource. A description of these assessments and their results is presented in Table 2.

Hammons [57] shows that in Europe, the United Kingdom has access to 47.7 % of Europe's tidal energy, followed by 42.1 % in France, 7.6 % in Ireland, 1.8 % in Holland, and the remaining in nations with some coastal regions. Based on the Special Report on Renewable Energy Sources and Climate Change Mitigation from the Intergovernmental Panel on Climate Change and Table 2, present day energy consumptions can be met impart by using marine energy [52]. It should be noted that turbine efficiency, site accessibility, technological

Table 2: Resource assessment for marine energy indicates the potential for offsetting a considerable portion of the current energy usage with hydrokinetic energy [52].

Assessment	Nation	Marine location	Method	Results
Assessment of Canada's Hydrokinetic Power Potential [13] [15]	Canada	River	GIS, Area-ratio, RETScreen, physiographic/-climatic data, and estimations	> 300 GW with 95 % CI [theoretical]
Assessment and Mapping of the Riverine Hydrokinetic Resource in the Continental United States [48]	United States	River	Hydraulic head and GIS information	157 GW [recoverable]
Value Proposition for Tidal Energy Development in Nova Scotia, Atlantic Canada, and Canada [49] [53] [54]	Canada	Bay of Fundy	Finite Volume Method numerical simulation	2.5 GW [theoretical]
Assessment of Energy Production Potential from Tidal Streams in the United States [50]	United States	Tidal [selective locations]	Regional Ocean Modeling System	$\sim 8\ kW/m^2$ [theoretical]
Ocean Energy Technology Study [51] [52] [55]	Global	Wave, Tidal, Thermal, Osmotic	Unknown	9 TW
Tidal Energy in France [56]	France	Raz Blanchard Tides	Modeling	1.82 GW

limitations, and socio-economic factors play important roles in the amount of energy that can be harnessed. A process of standardizing HKT systems, such as the one conducted by Babarit et al. [58] specifically for wave energy converters , would provide a more reliant and clear image for policy makers to integrate HKT technology in power generation. The potential of marine energy presents a viable resource that can be more predictable than current renewable energy applications. The RHT increases the extraction of this resource by simplifying deployment/retrieval procedures as well as allowing annual operation in cold

climate conditions.

2.4   Hydrokinetic turbine technology

The technological advancements in the hydrokinetic industry have progressed over the last decade thanks in part to the adaptation of technologies from similar industries and from the investment that government initiatives have had worldwide [26, 59]. Hydrokinetic turbines are classified based on parameters which describe its operating conditions:

1. Type of marine environment the turbine is located in.

2. Location of the turbine in the water column.

3. Axis of turbine rotation with respect to the mean flow direction.

4. Conversion method of harnessing the kinetic energy of the flow (i.e. lift-based, drag-based, flutter vane, etc.).

Ocean HKTs have had significant progress in their technological development which is also valuable to investigate. The advancements in ocean marine turbines can be attributed to the predictability of tides which have a 98 % accuracy for decades into the future [59]. Table 3 contains a list of relevant HKT designs which posses similar technology or operational requirements to the proposed RHT. Furthermore Thorpe [60] from the World Energy Council complied over 100 different designs and models for wave energy converters ranging from theoretical models to full scale commercial models.

Due to the demanding conditions of marine environments even small scale prototypes being field tested require considerable structural and mechanical strength to withstand the drag loads of the marine environment. This increases the challenge of developing marine turbines as considerable financial support is required for any contribution to be made [18]. As a consequence of this, the current industry consists mainly of floating surface structures with few turbines being placed on the river bed. Only 20% of all of the companies that have tested

at the CHTTC up to now have situated their HKT on the bottom of the river channel. The remainder have placed their support structure floating on the river surface. Kitted HKTs have a more demanding design requirement for successful operation, yet a smaller impact on the deployment and retrieval procedures. This is due to fairly well established method of anchoring [61, 62, 63], and the use of ballast tanks for buoyancy control which has been extensively employed in submarines. Table 3 describes a few relevant HKT designs with some having been field tested.

Table 3: A list of HKT designs with relevant features to the proposed RHT.

Name	Year	Location	Capacity	Description
Aquantis Ocean Current Generation Device [64]	2014	Gulf stream	2.5 MW	Dual rotor tethered current turbine operating at $1.2 - 1.8$ m/s with patented Passive Depth Stability controlling water depth location.
Bluewater's Tidal Energy Converter(BlueTEC) [62]	Unknown	Nova Scotia (test location)	2 MW	Floating platform gives the flexibility to install a variety of different turbines including horizontal or vertical axis.
CoRMat [61] [65]	2013	Sound of Islay, Scotland	0.5 MW	Counter rotating dual rotors operating at ocean depths of 8 to 500 m, moored to ocean floor with the use of buoyancy control to located operating depth.
Deep Green [66] [67]	2017	Wales	0.5 MW	Tethered kite which flies in a figure 8 pattern in tidal current increases flow velocity 10 fold, a 1/4 scale model tested successfully in Northern Scotland in 2013.

Name	Year	Location	Capacity	Description
RiverStar [68]	Unknown	United States	50 kW	Floating surface buoy with attached horizontal axis turbine, power line and tether line connects laterally to next subsequent turbine underwater and eventually to shore.
Oceade (previously known as Deep Gen) [69]	2013	Scotland (European Marine Energy Centre)	1 MW	Ocean bed mounted horizontal axis turbine with pitchable blades for tidal generation, entire turbine system floats for easy delivery to site.
DeltaStream [70]	2014	Ramsey Sound, UK	1.2 MW	A set of 3 turbines with fixed blades laid in a delta formation with connecting foundation, partnered with Cranfield University for numerical and experimental design work.
Eco-auger [71]	2012	USA	$\sim > 4\ kW$	A double helix horizontal axis turbine which pumps oil for generating electricity for remote communities, awarded the ConocoPhillips Energy Prize in 2009.
Kobold Vertical Axis Turbine [72]	2011	Strait of Messina, Italy	160 kW	A floating buoy with a vertical axis Kobold turbine attached with 4 moorings at a water depth of $18 - 25\ m$.
Evopod [63]	2014	Scotland	35 kW	Floating surface buoy which is moored to the ocean bed, a horizontal axis 4.5 m diameter turbine connected underneath operates with the tide; a 6 months winter operation proved successful even in harsh winter storms.

Name	Year	Location	Capacity	Description
THOR [43] [73]	2012	USA	Small Scale	Single rotor tethered turbine with a single counter-torquing ballast tank, wings, and central ballast tank to control the stability, water depth, and power output of the turbine.
Tocardo [74]	2008	Netherlands	2 MW	Simple yet effective single rotor horizontal axis turbine connected to nearby surface structure, such as a bridge or dam, cost effective and low maintenance makes turbine attractive in market.
GEM [75] [76]	2012	Forte SantAndrea, Italy	20 kW	Dual parallel rotors, each 3.08 m diameter rotor has a lift based shroud, deployed in 1.5 m/s ocean flow tethered with buoyant buoys for adjusting operational depth, numerical and experimental work done at the University of Naples.
Verdant Powers Kinetic Hydropower System (KHPS) [77]	2006-2009	New York, USA	1.3 kW	Six vertical axis bottom mounted turbines which were grid connected operated for 9000 hours generating 70 MWh, the tidal turbines rotated 170 deg every 6 hours and operated at flow speeds of approximately 1 m/s.
Hydra Tidal [78]	2010	Lofoten Islands, North of Norway	1.5 MW	Two sets of 2 horizontal axis turbines in-line with each other, a floating housing platform is moored to the ocean bed for tidal or river application, each rotor consists of 2 blades constructed out of wood.

The turbines that have been deployed and operated within the past decade have achieved an appreciable amount of success. Challenges for the turbines researched in Table 3 includes:

- the requirment of a custom transport vessel for turbine deployment;

- the installation of complex underwater support structures from a floating vessel;

- dealing with cold climate damage to surface structures in both rivers and oceans; and

- costly or insufficient consideration for maintenance procedures.

The use of kitted lines and ballast tanks presents one alternative to address these challenges, as shown by Hunt [43], Lane [61], Frith [66], Jansson [67], Bourne [68], and Fleming [64]. One limitation that is common with all of the current kitted designs is their reliance on either dual counter-rotating rotors or a highly secured mooring line to balance the turbine torque. The GEM prototype tested by Coiro et al. [76] showed that in a dual rotor tethered system, when one turbine is held fixed and the second rotor is rotating at 200 RPM, the system can reach a yaw angle of up to 20°. The Riverstar design [68] uses a channel wide mooring lines that can present an obstacle for fish and existing marine users, along with increasing the risk of damage from underwater debris. The RHT design addresses these issues by having a single mooring that is in-line with the flow, minimizing its projected frontal area; as well as having an extended ballast tank behind the nacelle to realign the turbine towards the flow during yawing motions. Hunt [43] performed experimental tests on a single rotor tethered HKT, similar to the RHT, which uses a ballast tank for buoyancy, an aerodynamic wing for increased lift, and a flap to produce the stabilizing counter-torque. The Thor design consists of a few challenges which include an asymmetrical support structure that needs to be stabilized through mass distribution and anchor positioning, the identification of the metacenter to prevent capsizing during deployment, and a mechanical system that would operate the flap for counter-torquing. The RHT design overcomes these challenges by having a symmetrical configuration in both geometry and mass distribution when initially placed

onto the river, and a non-mechanical system for counter-torquing. The bottom mounted HKT Oceade [69] has taken the benefits of ballast tank deployment and coupled it with the rigidity of a bottom mounted support structure. The controlled descent of the nacelle of this HKT must be aligned with the bottom mount support structure which is previously deployed. The deployment and retrieval procedures uses the ballast tanks on the nacelle to descend and ascend the main turbine nacelle from the anchored support structure which remains on the ocean floor. Using material selection from HKTs such as the Oceade, the RHT design can autonomously float on the river surface when its ballast tanks are filled with air, and only descend under controlled conditions when its ballast tanks are remotely filled with water.

2.5   Anchoring techniques

Some of the difficulties associated with hydrokinetic turbine include deployment and retrieval procedures [4] [21] [79]. Bibeau et al. [25] have experienced the challenges associated with riverine hydrokinetic turbine deployment at the CHTTC. Figure 15 illustrates one operation in cold weather.

(a) Survival suits   (b) Ice accretion encases pontoon

Figure 15: Winter opteration at the CHTTC presents additional challenges that inhibits regular procedures. (a) Testing an acoustic release buoy in cold weather at the CHTTC requires survival suits, this delays the onset of hypothermia in the case someone falls into the water.(b) Snow covered surface support structure for horizontal axis turbine.

Khan et al. [26] indicate that the location of where a hydrokinetic turbine is placed can have a significant impact on its life cycle, maintainability, construction challenges, safety regulations, energy density, ecological impact, and design specifications of the turbine. Figure 16 illustrate the primary locations for a HKT in a riverine, ocean, and tidal environment. This includes: floating on the marine surface, laying on the bottom of the marine bed, or kitted in the boundary layer position with a tethered line.

(a) Bottom mount

(b) Floating mount

(c) Water column mount
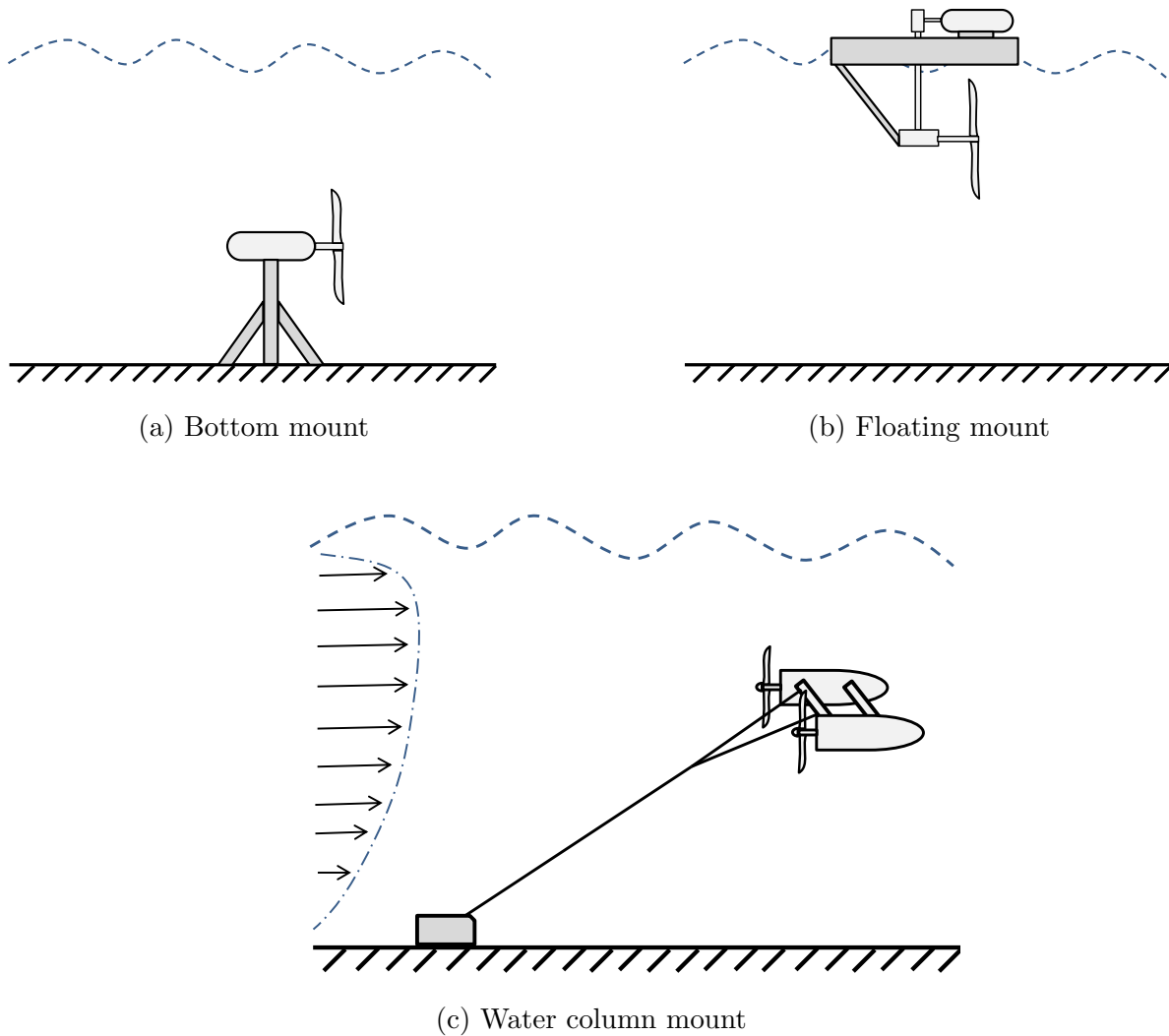
Figure 16: Three main techniques for turbine deployment. (a) Bottom mounted turbines can avoid surface interference yet they lie in low velocity regions. (b) Floating surface turbines are more accessible but cannot operate in cold climates due to icing accretion. (c) Water column HKTs avoid surface debris while have the benefits of floating surface mount of being easily retrieved. An additional control parameter for adjusting its operating point in the water column is required.

Murray and Michael [33] assessed some the specific challenges associated with current hydrokinetic operations and deployments. This includes the:

- high factor of safety due to unrecorded environmental impacts on the turbine;

- lack of understanding of long term turbine operation in marine environment;

- absence of internationally accepted standards for proper cost analysis;

- inability to justify high costs associated with grid connections in remote regions and off-shore locations; and the

- insufficient turbine farm demonstration for utility scale power generation.

2.5.1   Floating support structure

A floating support structure houses the turbine, generator, and sometimes its power electronics. It can be anchored to either an eyelet on a nearby shore or to a submerged anchor. The design of the floating structure frequently resembles a modified boat or custom pontoon. The advantages of accessibility, mobility, and familarity with existing transport vessels makes the floating structure an attractive option for initial turbine testing. However, this does not translate well into long term turbine operation due to icing issues mentioned in Section 2.2.1 in cold climate regions. Guney and Kaygusuz [80] also mentions how in heavily populated areas, the floating structure can block the passage of the ships and cause social/political issues with fishing boats. Bibeau et al. [25] discusses how in remote regions ice and debris accumulation, including hazardous frazil ice, can cripple the structural integrity of a floating support structure over time and eventually sink it.

The location of a floating mount can provide the maximum energy density from the flow since the location of the maximum flow velocity of a riverine channel is found at approximately 20% below the water surface [39]. Given this advantage, the development for maintaining a floating structure for an extended period of time is still in development. A few companies

Figure 17: New Energy Corporation 5 kW vertical axis turbine is mounted on a custom floating support structure which is dragged to the site location and moored either to a shore anchor or to a granite block on the river bed

including Bluewater's Tidal Energy Converter [62] and the Evopod [63] have had some successes with this designs in open ocean environments. The development of a rugged and structurally prominent design has allowed these turbines to survive harsh winter storms in open ocean waters with the use of bottom anchor cables fixed to the support structure on the water surface.

2.5.2   Bottom mounted support structure

Bottom mounted HKTs address the challenges of shipping traffic and icing issues affecting floating HKTs since they are located underneath the water surface. Technology from oil platforms have been transferred to bottom mounts with some success. This is evident with the first commercial grid connected tidal stream turbine SeaGen established by Marine Current Turbines [41]. One challenge for bottom mounted river turbines is the costs associated with the deployment and retrieval procedures. This can be seen from the mounting bracket installed in the river bedrock at the CHTTC by Bibeau et al. [22] in October of 2006 which required a barge, a drilling ridge, and two safety boats. Even with its success, the solution employed is unique to locations where access to a barge and drilling platform is available in addition to having a solid bedrock foundation. Another technique used at the CHTTC in 2013 involved placing a large cement block on the river bottom to which a bottom mounted

turbine was anchored. This is a more versatile method as it can be employed in a variety of river environments. A challenge of bottom mounted HKTs is the power electronics which must either:

1. Operate in a dry environment with a dynamic seal for the generator shaft.

2. Function with a flooded generator, in which case the fluid may be used as a lubricant.

Unlike bottom mounted turbines, surface mounted turbines do not need a fully water sealed generator and power electronics since they are located on the water surface. This can reduce the maintenance and installation costs. Even with some of these benefits the current technology available for the operation of a HKTs do not present a cost competitive alternative to existing renewable energy such as wind or solar [3]. Figure 18 illustrates the first commercial tidal turbine SeaGen: a pile mount inserted into the ocean floor acts as its support structure allowing the nacelle to slide along the pile with a mechanically driven rack and pinion system.

Figure 18: SeaGen was deployed in 2008 operating at a rated capacity of 1.2 MW in Northern Ireland, successfully generated over 8 GWh of electricity to date [42].

2.5.3   Water column positioning

Positioning of a hydrokinetic turbine in the water column with the use of tethered cables is seldom used, yet has several key advantages over the floating mount and the bottom mount HKTs. There are prototypes that currently employ this technique such as THOR [43], Deep Green [66], and Aquantis Ocean Current Generation Device [64], yet based on literature there have been limited large scale deployments. The only field experiment was conducted by Minesto with the Deep Green turbine in 2013. The test was initially conducted on a floating research platform which was then advanced to ocean bed anchoring [66]. Certain unique problems associated with this method of deployment include the buoyancy controller for positioning the turbine in the water column, the influence of vortex shedding from upstream anchor and mooring line on turbine performance, and the dynamic stability of pitching and yawing controls. Currently the designs associated with water column deployments rely on the use or combination of aerodynamic wings and ballast tanks to control the turbine's operating point along the water column such as the Thor prototype [43].

The operation of a single rotor tethered turbine is a multi-constraint problem which requires analysis in several key functional design components including its deployment/retrieval technique, operational dynamic stability, influence of the upstream mount on its performance, and emergency failure cases. Section 3 discusses the analytical modeling and design components required to operate the passive stability system for such as single rotor turbine.

3   Proposed novel counter-torque design

The design of the novel counter-torque mechanism described in Section 1.2.4 is required for a single rotor tethered HKT. This design addresses the challenges presented in Section 1 by:

- employing a single turbine with a counter-torque mechanism to avoid the complexities of balancing torques on two separate rotor shafts;

- utilizing the support structure of the RHT as a pontoon during delivery to reduce deployment costs; and

- having ballast tanks located in the nacelle that allow for ascending and descending the RHT from the water while also providing a mechanism for optimizing its positioning in the river's velocity profile.

The design of the counter-torque mechanism requires the development of:

Governing equations The derivation of the balancing torque required to counter the torque on the rotor shaft is based on the maximum flow velocity of the water tunnel and the maximum allowable load on the generator.

Functional components The mechanical and electrical components must be identified and integrated together into the turbine system. This includes the:

- counter-torque material,

- generator specifications and underwater operation,

- fabrication material for the support structure,

- sensor selection and waterproofing,

- suitable turbine,

- data acquisition and microcontroller programming, and

- preliminary methodology for testing.

CAD design Integrating all of the functional components together requires the iterative design of a support structure. The 3D CAD design accommodates the mechanical and electrical components while withstanding the drag load of the flow.

Fabrication/Assembly The final assembly and operation of the scaled prototype in the water tunnel is considered during the design phase since the design process is done in parallel to consider all aspects of the project.

This chapter details the scaled counter-torque mechanism, its operation, the design considerations made, the static and dynamic governing equations, the 3D SolidWorks CAD, the generator and turbine selection, and the fabrication of the scaled support structure. Certain design elements are not included or limited in detail as they are beyond the scope of the project, such as the filters for signal processing, microcontroller coding, and in-house post-processing program.

3.1   Scaled RHT system

The proposed passive counter-torquing mechanism is based on Newton's third law of motion in a rotating reference frame which governs the balance of the rotor torque and the counter-torque mechanism. The torque on the rotor shaft is a result of the rotor blades absorbing a fraction of the kinetic energy from the flow, while the passive counter-torque is a product of two point masses located at a fixed distance away from the rotor shaft on the end of two spokes. One of the point masses exhibits a constant positive buoyant force, while the other exhibits a constant negative buoyant force. Figure 19 shows a side view of the major components of the scaled prototype.

During the operation, the system is suspended in the flow with two tethered lines connected at each point mass. The tethered lines converge onto a single line which is then used to anchor the turbine. The tethered connections allow the point masses to rotate about the rotor axis
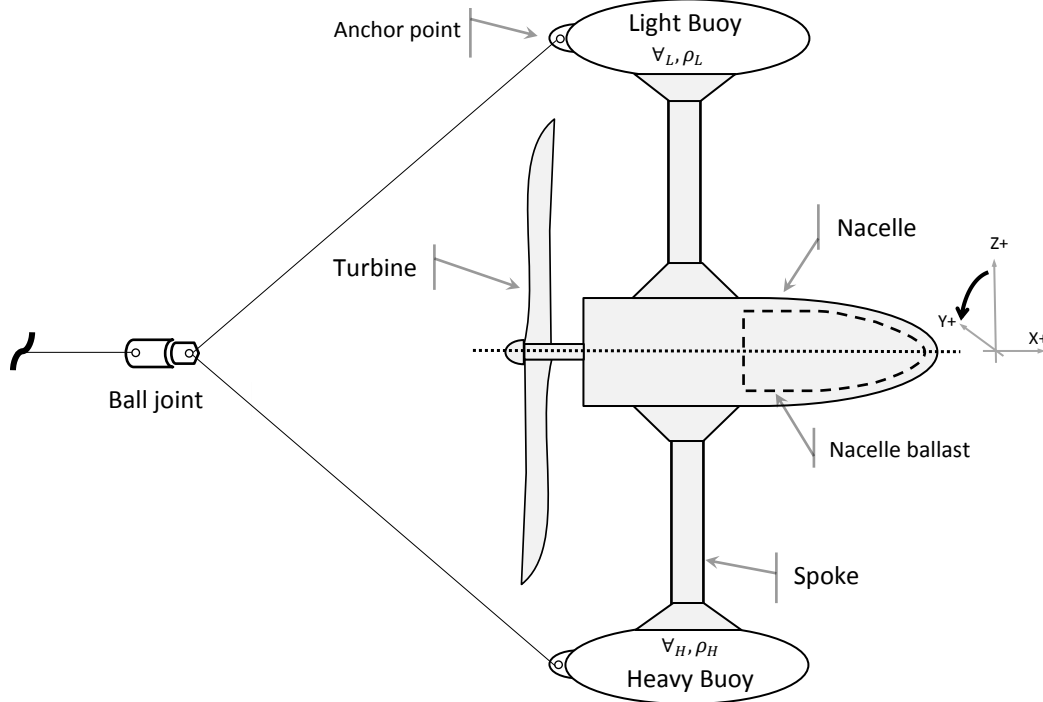
Figure 19: Side view of the scaled prototype, symmetric airfoil spokes connect to the nacelle which houses the geared 19.1 VDC generator. The torque on the turbine causes the system to passively incline between 0° and 90° to produce an equal balancing torque from the fixed buoys at either end of the spokes.

which varies the degree of counter-torque. When there is no torque on the rotor shaft, the point masses line up vertically which results in a zero moment arm and consequently zero counter-torque. As the rotor shaft torque increases, the angles of inclination of the spoke arm increases with respect to the y-axis which creates a larger moment arm and thus a larger counter-torque. The inclination angle of the system reacts to the changes in the torque of the rotor shaft, adjusting itself to the necessary counter-torque necessary to reach a new equilibrium. The central hub houses the generator, similar to wind turbine nacelles, with the spokes connected to the top and bottom. The point masses will be referred to as light and heavy "buoys" for the positively buoyant and negatively buoyant point masses respectively. Refer to Figure 19 for illustration. The scaled prototype includes all of the components presented in Section 2.1 except for the yawing mechanism which is not necessary due to the self-realignment of the nacelle with the mean flow direction. The entire scaled prototype is referred to as the "turbine system", and the combination of the nacelle, spoke, and buoys acts

as the turbine's support structure. The term "rotor" and "turbine" are used interchangeably as they refer to the mechanical device that extracts the kinetic energy of the flow and converts it to rotational motion.

3.1.1   Light and heavy buoy

For the scaled counter-torque operation, the light buoy consists of air to provide a positive buoyant force, while the bottom buoy consists of stainless steel ball bearings to provide a negative buoyant force. A Factor of Safety (FOS) is introduced during the design phase of the scaled prototype by:

1. Modeling the light and heavy buoys to be larger than their required volume.

2. Selecting the equilibrium point for the inclination angle of the turbine system to be 45°, allowing system to incline an additional 45° before it reaches its ultimate counter-torque.

As a result, a FOS of 2.2 is present for the heavy buoy, 4.7 for the light buoy, and 1.4 for the inclination angle, with a final FOS of 4.7 for the turbine system. The FOS can account for any unknown factors that may influence the operation of the turbine during testing, while also allowing the option to vary the point masses in the light and heavy buoys to determine the relationship between counter-torque and the rotor torque. The materials selected to provide the counter-torquing force has to meet the following criteria:

- accessibility in buoy cavity;

- no hazardous effect when introduced to the water system (filtration, contamination, etc.);

- greatest possible density difference with respect to water; and

- ease of measuring volume and/or mass

- relatively inexpensive

For the scaled prototype, stainless steel balls are employed for the heavy buoy and the air for the light buoy based on the above stated criteria.

3.1.2   Electromechanical conversion

The kinetic energy available in the flow is transformed to electrical energy through mechanical and electrical conversions. The turbine blade converts the kinetic energy of the flow into rotary motion which is then fed to the DC machine. Figure 20 illustrates this process which starts from:

Flow dynamic torque (T_f) The dynamic torque available in the flow is based on the flow velocity, turbine area, and fluid density. Refer to Appendix B for equations.

Turbine torque (T_r) The fraction of the torque absorbed by the turbine from the dynamic torque in the flow.

Gearbox torque (T_g) The torque on the output of the gearbox shaft after frictional losses have reduced the torque extracted by the turbine.

The generator transforms the mechanical energy into electrical energy with mechanical losses in the gearbox and bearings, along with copper losses present in the winding's and commutator brushes. These losses are represented by the armature resistance R_a. After all of the losses the final output power is applied to the rheostat load from the generator. This load draws current from the generator and dissipates it through heat. By changing the resistance on the load, the current drawn from the generator is alternated which consequently changes the torque drawn from the gearbox and rotor shaft.

The constraints of the scaled prototype include:

- Overall length of the turbine structure has to accommodate the counter-torquing mechanism while not interfering with the rotor blade which has a nominal diameter of 203 mm.
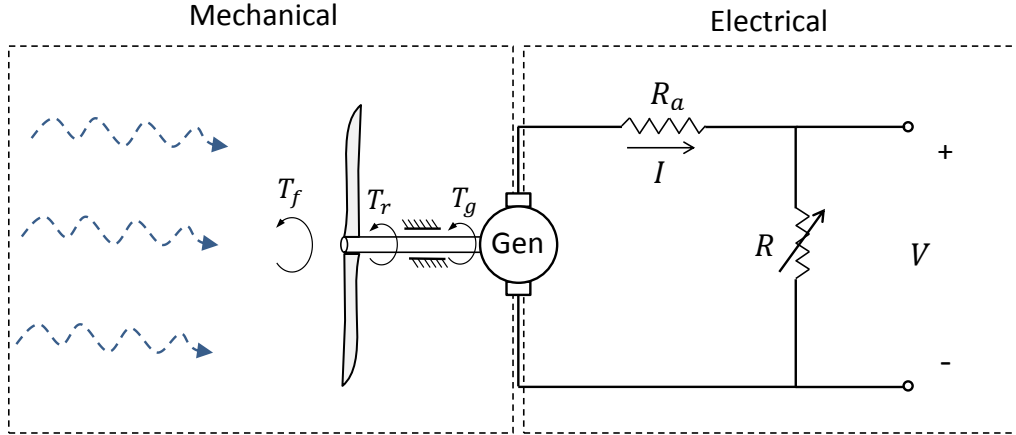
Figure 20: The electromechanical system which starts with the flow's dynamic torque on the left, converted to the shaft rotary motion by the turbine, perturbed by the losses in the gearbox and electrical resistance, outputted as electrical power on the load

- Generator's torque capacity should be as close as possible to the maximum flow torque of 0.153 Nm after an experimentally tested torque coefficient of 0.1 is factored in [81].

- The RPM of the generator at its maximum flow torque should fall as close as possible to 361 RPM which provides a TSR of 3.75 to capture as much of the power coefficient as possible [81].

- The counter-torque design needs to have the option to be varied since the performance at different capacities and operating conditions are measured.

The analytical calculations for the governing equations considers the constraints and design requirements laid out.

3.2   Analytical design

The analytical model consists of the static and dynamic equations that dictate the necessary counter-torque needed to balance the turbine torque and whether or not the system can establish the stable operating point with different starting conditions. A coordinate system is established based on the water tunnel layout shown in Figure 21.
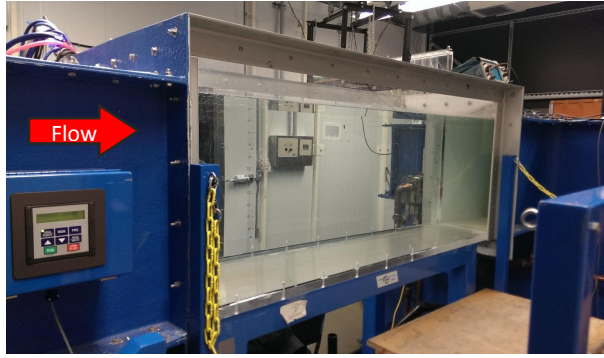
(a) Image of water tunnel
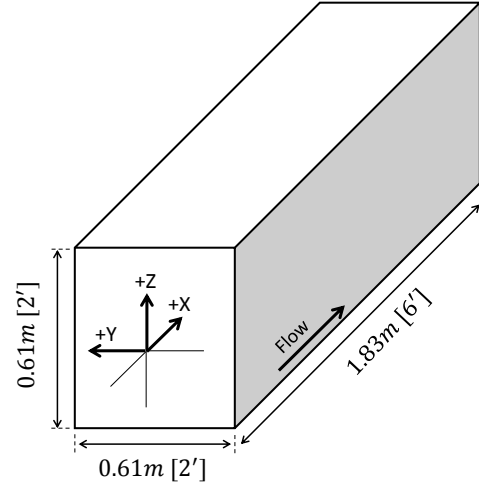
(b) Coordinate system and dimensions of the water tunnel

Figure 21: Water tunnel setup and the corresponding coordinate system established for the scaled RHT prototype

A set of assumptions are made for the analytical modeling of the turbine system. These assumptions include:

- water density in water tunnel at atmospheric pressure and $20°C$ is 1000 kg/m^3

- air density at 101.3 kPa atmospheric pressure and $20°C$ is 1.205 kg/m^3 [82]

- acceleration due to gravity is 9.81 m/s

The boundary conditions for the turbine operation are established through preliminary experimental tests and the design calculations. They are presented in Table 4 and they are necessary for the remainder of this section. Further details can be found in their corresponding sections.

Given the large number of possible operating points that exist from Table 4: operating angles $(0° - 90°)$, generator torque (3.5 to 35 Ω), and flow velocity (0 to 1.1 m/s); a Maximum Safe Operating Point (MSOP) is established to be largest turbine torque the counter-torque mechanism is required to balance. This is discussed in following section.

Table 4: Boundary conditions for each test parameter and operation condition; established through testing and calculations.

Parameter	Boundary condition	Section
Inclination angle	The inclination angle varies between the positive z-axis direction, representing 0°, and the positive y-direction, representing 90°. This is a consequence of the sinusoidal relationship between the counter-torque and the inclination angle of the system. In which 0° produces the minimum counter-torque and 90° produces the maximum.	3.2.1
Resistive load	The full range on the rheostat is used as the load for the generator, and is adjustable between 3.5 Ω and 35 Ω with 3.5 Ω resolution. The rheostat is able to dissipate up to 1.2 *Amps*	4.2.2
Flow velocity	The water tunnel is capable of flow velocities up to 1.1 m/s. The lower limit boundary condition is established by slowest flow velocity that is capable of elevating the RHT prototype off the water tunnel floor. The upper condition is established by the highest flow rate possible with minimal electromagnetic interference on the operation of the microcontroller and data acquisition unit.	4.2.2
Counter-Torque Capacity (CTC)	As a result of the buoy cavities being designed larger than necessary, the performance of the counter-torque mechanism can be varied by adding or removing the air and stainless steel balls in the light and heavy buoys respectively. A 50% CTC consists of both cavities having half of their volumetric space occupied with their respective counter-torquing material while the remaining volume is filled with water.	3.2.1, 4.2.2

3.2.1   Static model

This section presents the static model of the scaled RHT prototype when it reaches an equilibrium point. After the governing equations are established the MSOP parameters are substituted to solve for the unknown design parameters in the equation.

The governing equation for the counter-torquing mechanism is the cross product of the applied forces from the buoys and the moment arm created by the inclination of the turbine

system and spoke arm. The positive buoyant force from the light buoy is represented by F_L; the force applied by the heavy buoy, F_H; the arm length of the spoke, L; and the inclination angle of the scaled turbine system, θ. The total counter-torque generated, T_T, is a cumulation of the torques from the two buoys. The torque from the light buoy is represented by T_L, and the torque from the heavy buoy is represented by T_H. Figure 22 illustrates the free body diagram with the force vectors described.
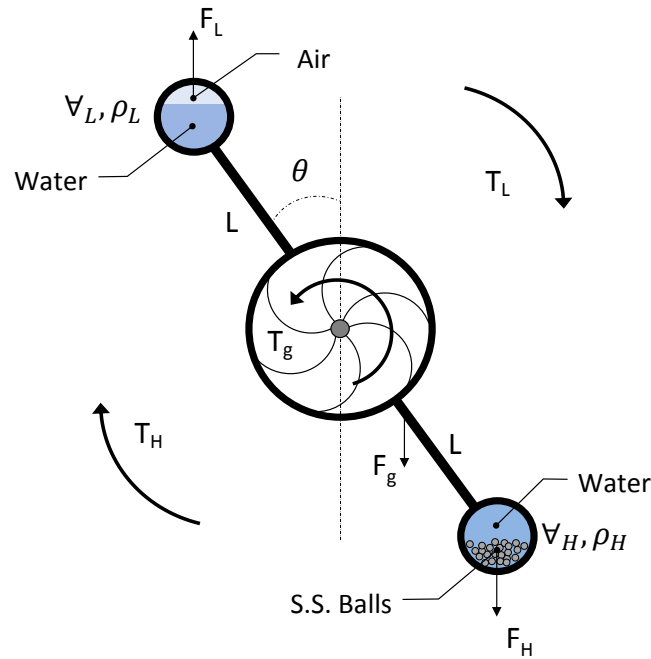
Figure 22: Free body diagram for forces and torques on scaled prototype RHT. The buoys have a combination of water and counter-torque material for controlling CTC.

The requirements of the counter-torque mechanism is calculated by equating two terms:

1. The **rotor torque** during operation, which is a function of the turbine blade profile.

2. The **counter-torque** cross product that is needed to balance the first term, and is a function of the total force exerted by the buoys, the inclination angle of the turbine system, and the spoke length.

The two terms above are calculated while ignoring mechanical and electrical losses since the information is not available during the design phase. The FOS introduced into the system

compensates for the frictional torque losses and the electrical inefficiencies. As a result, Equation 38 indicates an approximate equality of two terms. Previous experimental work conducted by Shahsavarifard et al. [81] on the same turbine blade established the torque coefficient, C_t, to have a maximum of 0.1 at a TSR of 3.75. With the torque coefficient, and the dynamic torque from the flow (detailed in Appendix B.1), the amount of torque that needs to be countered can be derived, as shown in Equation 5. Where the fluid density is represented by ρ, the flow velocity by v, and the turbine radius by r.

$$T_r = C_t T_f \tag{3}$$

$$T_T \approx T_r \tag{4}$$

$$T_T \approx \frac{1}{2} C_t \rho A v^2 r \tag{5}$$

With the first term represented by Equation 5 established, the second term can be derived. Equation 6 shows the cross-product of the total force exerted by both buoys, F_T, the spoke length, L, and inclination angle, θ.

$$T_T = F_T L \sin \theta \tag{6}$$

Equation 5 and Equation 6 can then be equated. Here the MSOP can be inserted into the equation and the remaining unknowns solved. The MSOP is the targeted operating condition for the turbine when the flow rate is at the maximum nominal 1 m/s, with the turbine's inclination angle at 45°, and the buoy at a CTC of 100 %; where both buoys are completely filled with their respective counter-torque material. The remaining unknowns include the spoke length, and the total force exerted by the buoys. With two unknowns and only one

equation the spoke length is set to be 165 mm from the rotor's axis. The basis of the spoke length comes from two factors: 1) to create enough of a clearance between the turbine rotor and the mooring lines, and 2) to ensure that the 3D printer model is able to accommodate the size of the turbine system. Table 5 summarizes the MSOP and its condition which theoretically ensures that the counter-torque prototype will successfully balance the rotor torque for any flow velocity below 1.1 m/s. Note that a slight, but fairly negligible change to the spoke length is made due to the to the offset of the generator's gearbox.

Table 5: Maximum Safe Operating Point for turbine testing

Parameter	Variable	Value	Established
Rotor torque	T_r	0.153 Nm	Calculated from maximum nominal flow velocity of 1 m/s, Equation 5
Counter-torque Capacity	CTC	100%	Set to completely fill the available volume of both buoys.
Inclination angle	θ	45°	Set as half of the maximum inclination angle.
Spoke length	L	165 mm	Based the clearance of the turbine and mooring line along with the fabrication limitations.

Equating Equation 5 to 6 and isolating F_T, gives Equation 7, which is the total force needed to provide the necessary counter-torque.

$$F_T = \frac{C_t \rho A v^2 r}{2L \sin \theta} \tag{7}$$

Since the specific gravity of each counter-torquing material is not the same, the amount of force exerted per unit volume of air compared to the ball bearings will not be equal. To allow for a symmetrical buoy design, a volume distribution variable, β, is created which distributes the amount of force between the two buoys such that their volumes will be equal. The total force is distributed between the light and heavy buoy in Equation 8 where a volume distribution variable, β, represents the percent of the force that is provided by the light buoy,

with the remaining force, $1 - \beta$, provided by the heavy buoy.

$$F_T = \left[\beta F_T\right]_{Light} + \left[(1 - \beta)F_T\right]_{Heavy} \tag{8}$$

Archimedes' principle dictates the force exerted by each buoy, shown in Equation 9 and 10 for the light buoy force, F_L, and heavy buoy, F_H, respectively. By isolating the volume term in Equation 9 and 10 and inserting the force required for the counter-torque in Equation 7, the final form of the required buoy volumes can be established, as shown in Equation 11 and 12. Note the light buoy density is ρ_L and the volume $\forall_L$, while heavy buoy density is ρ_H and volume $\forall_H$.

$$F_L = g\forall_L(\rho_w - \rho_L) \tag{9}$$

$$F_H = g\forall_H(\rho_H - \rho_w) \tag{10}$$

$$\forall_L = \frac{\beta C_t \rho A v^2 r}{2gL\sin(\theta)(\rho_w - \rho_L)} \tag{11} \qquad \forall_H = \frac{(1 - \beta)C_t \rho A v^2 r}{2gL\sin(\theta)(\rho_H - \rho_w)} \tag{12}$$

To determine the distribution of the total force amongst the two buoys, a plot of the volume of each cavity versus the buoy force distribution is presented in Figure 23. Since all of the parameters are known based on the assumptions and MSOP values, the only unknown is the buoy force distribution variable. The expected plot of the buoy volumes versus the distribution parameter, β, is linear. Figure 23 shows how increasing the light buoy volume results in a decrease in the heavy buoy volume. This is expected since as the contributions of one buoy force increases the alternative force decreases.

From the static equations and from Figure 23 it can be concluded that for a symmetrical
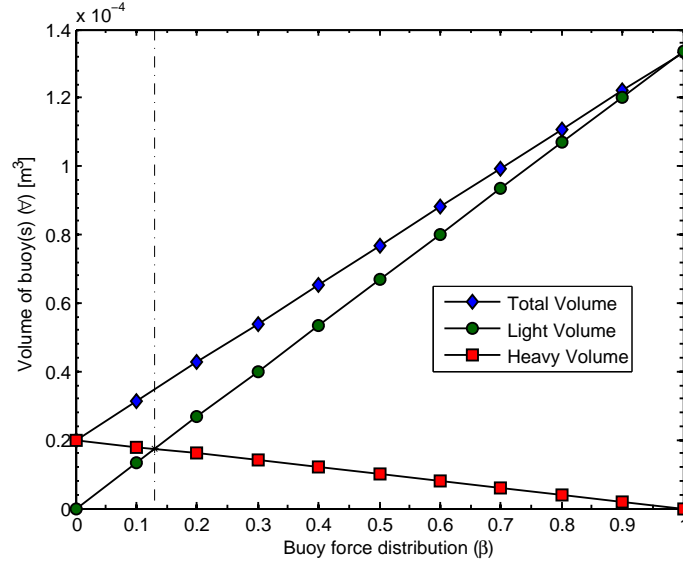
Figure 23: Distribution of volume amongst the buoys indicates a β value of 0.13 would allow both buoys to have equal volume and perform within the MSOP parameters

prototype, each of the buoys require a volume of 1.73×10^{-5} m^3 in order to balance the torque on the rotor shaft. This is established from a distribution variable of 0.13, which indicates that 13% of the counter-torque is provided by the light buoy while 87% is provided by the heavy buoy. During the 3D modeling phase, the actual buoy volumes are over sized in order to provide a FOS, as discussed in Section 3.1.1. In addition, due to the over sized buoys and the material being used for counter-torquing, the amount of counter-torquing force being exerted can be varied by volumetrically adjusting the air-to-water ratio in the light buoy and the ball bearing-to-water ratio in the heavy buoy. The volumetric percentage that each counter-torquing material occupies is referred to as the CTC. As an example, a 50% CTC indicates that half of the volume of the buoys are filled with water while the other remaining volume is filled with the buoy's respective counter-torquing material. If the CTC is not sufficient enough to balance the torque on the generator the entire system would rotate beyond an inclination angle of 90° into a continuous unsteady 360° rotation about the ball joint of the anchor. Figure 24 provides a graphical overview of the static equilibrium conditions for each possible combination of CTC and inclination angle of the system within the boundary conditions.
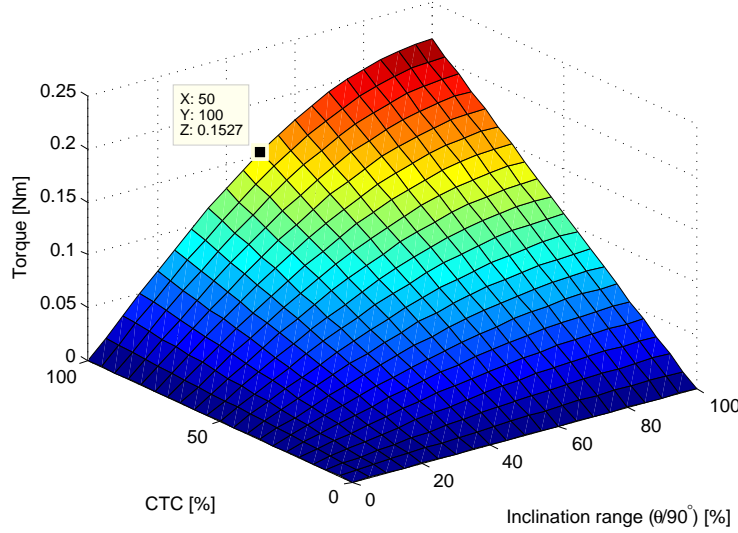
Figure 24: Counter-torque output for all variation of CTC and inclination angle of system within the upper and lower bounds of system's operating range

The MSOP condition can be identified in Figure 24 where the x-axis is at 50% indicating the system is inclined at 45° and the y-axis is at 100% which represents the buoys are filled completely with their respective counter-torquing material. At this operating point the counter-torque mechanism is required to balance 0.1527 Nm. A few observations can be noted:

- The projection of the plot onto the xz-plane (Torque versus Inclination) shows the first quarter of a sinusoidal curve which is a result of the counter-torque relationship with the angle of inclination. This is confirmed from Equation 6 where the total counter-torque, T_T, varies sinusoidal with the inclination angle, θ.

- Observing the yz-plane (Torque versus CTC) shows the linear relationship between the counter-torque and the CTC. This can be observed from Equation 6 where the total counter-torque is directly proportional to the force exerted by the buoys, which from Equation 9 and 10 is directly proportional to the occupied volume.

The turbine system reaches the equilibrium points established after stabilizing from its initial condition. The following section presents the behavior and stability of the turbine system as it approaches the equilibrium point.

3.2.2   Dynamic model

The dynamic model investigates the behavior of the turbine system to see if it converges onto a steady state point or diverges away from it. In conjunction with the dynamic equations, a phase portrait will reinforce the physical response of the system when its initial condition is set away from an equilibrium point. The turbine system is a non-linear dynamic system due to the sinusoidal relationship between the buoy force and the inclination angle. To simplify the analysis, a linear approximation is used by calculating the Jacobian and the subsequent eigenvalues. The system of equations governing the dynamic system is shown in Equation 13 where each of the terms describes a physical response of the turbine system. The terms in Equation 13 represent, in order:

1. Torque in the turbine system.

2. Rotor torque.

3. Counter-torque stabilizing the system.

4. Frictional drag from the support structure, contributed by the spoke and buoy geometry.

5. Remaining frictional torque in the turbine system.

The friction coefficient, represented by b, is a culmination of all of the sources of resistive torque that exists in the system. A linearized autonomous model is used based on the viscous friction losses of a rotating shaft [83]. The coefficient, b, is determined by comparing the physical response of the system to the observed response of the experiment. The additional variables present in the Equation 13 includes the angular acceleration of the support structure, $\ddot{\theta}$, its angular velocity, $\dot{\theta}$, and its moment of inertia, I_m.

$$I_m\ddot{\theta} = T_r - F_T L \sin\theta - \rho\left[A_{spoke}(L/2)\big(\dot{\theta}(L/2)\big)^2 + A_{buoy}L(\dot{\theta}L)^2\right] - b\dot{\theta} \tag{13}$$

From the dynamic model, the eigenvalue can be determined which indicates if the system has a stable converging point. To evaluate the dynamic system, the MSOP case must be applied in addition to the parameters presented in Table 6. Solving the Jacobian and calculating its determinate leads to the result that the eigenvalue are both negative for the 2 by 2 system. This indicates that the linearized model is asymptotically stable for the designated equilibrium point which is defined by the MSOP and Table 6.

Table 6: Dynamic stability parameters along in addition to the MSOP variables

Parameter	Variable	Value
Inclination angle	θ	Independent variable
Frictional torque coefficient	b	0.1 Nms/rad
Turbine system's moment of inertia	I_m	0.0088 kgm^2

With the eigenvalues established, the trajectory of the system can be investigated through solving the linearized model in Matlab. The phase portrait and the trajectories of several initial conditions can be seen in Figure 25. The initial conditions are set at 7 angular positions each with zero angular velocity which replicates the experimental setup. The angular positions, which encompass 0, 0.25, 0.5, 0.75, 1.0, 1.25, and 1.5 rad (0°, 14.3°, 28.7°, 42.9°, 57.3°, 71.7°, and 85.9°) are all equally spaced within the top two quadrants of the Cartesian coordinates . These are the approximate starting positions for the turbine during testing.

Figure 25 illustrates that when the system is placed at any of the initial condition, it converges towards the equilibrium point when the counter-torque system is set to the MSOP. The system initially begins with a high angular velocity and then gradually reduces to zero, at which point the angular position has converged to 45.06°. The difference between this converging equilibrium point and the static model equilibrium point is 0.132%. This indicates that the static model and the experimentally adjusted dynamic model both result in the same equilibrium point for the same functional parameters. Further analytical testing indicates
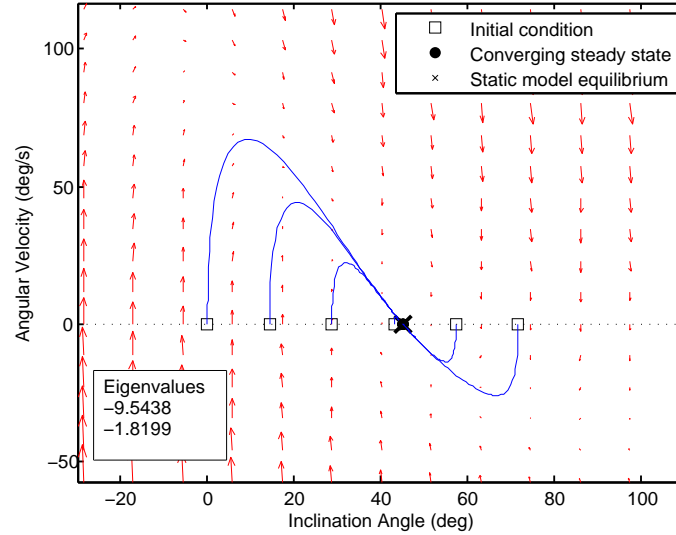
Figure 25: Phase portrait of dynamic stability of turbine system, note that the static model equilibrium is very close to the dynamic model's converging point

that if the equilibrium point is readjusted to 90°, such that the turbine system is aligned horizontally, the Jacobian results in a zero eigenvalue. According to Slotine and Li [84] and Lyapunov's stability criteria, no conclusive results for the behavior of the system can be established since the linearized system eigenvalue falls on the complex plane. This can be seen in Figure 26. It can be concluded that the 90° operating point is the edge of stability for the system in which any designed inclination angle less than that will produce a stable operating point while any angle greater than 90° will produce instability.

Based on the solution for the system's operation at the MSOP and maximum inclination angle it is clear that the turbine will converge to a stable equilibrium for any of the initial inclination angles between 0° and 90°. This represents the entire range for the scaled prototype operation. Following the analytical calculations for the inclination angle, a low drag zero lift design for the buoy geometry is employed to reduce the stress on the scaled prototype's mooring line.
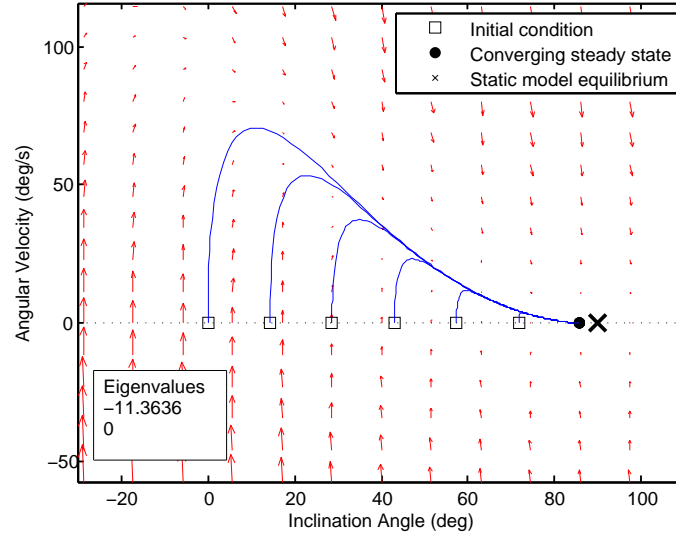
Figure 26: Linear model indicates inconclusive evidence for the system's behavior with the eigenvalue situated exactly at zero. From the sinusoidal behavior of the counter-torque mechanism though it is evident that the 90° inclination angle is the edge of stability in which any value beyond that will produce instability.

3.2.3   Drag reduction

A low drag zero lift geometry is employed for the buoy and nacelle geometry. From the design calculation performed on each component of the turbine system, it is evident that due to the mass of the generator and the density of the 3D printer material being used, the turbine's specific gravity is greater than one. This will cause the turbine to sink under its own weight due to the lack of buoyancy. As a result several alternative designs are investigated to increase the net upwards force on the system including:

- adjustable cambered wings mounted onto the nacelle

- removable foam inserts around the nacelle for positive buoyancy

- additional volume cavity located in the nacelle just behind the generator

The internal ballast tank in the nacelle is incorporated in the design due to technical challenges with the alternative options. The total volume provides a buoyancy force which is 25% of the total weight of the generator. Even though it is a small contribution, the cavity is included in the design since it has no negative side effects. Further more the anchor point

of the prototype is connected to the top of the water tunnel to provide the necessary upward force to keep the prototype turbine in the middle of the water tunnel. During preliminary testing a minimum flow velocity is established during to ensure that the the drag on the prototype is sufficient enough to raise it off the water tunnel floor. Section 4.2.2 discusses further the details of the preliminary tests. From the design process of the RHT prototype the overall specific gravity of the turbine system has become established as a critical component for the scaling parameters for a riverine site. Similar challenges with the turbine's overall mass were encountered during field testing of the Deep Green hydrokinetic turbine in Northern Ireland where they also employed the technique of anchoring their turbine to a floating research platform [66] [67]. Figure 27 illustrates the positioning of the mooring line and turbine system in relation to the anchoring point on the top of the water tunnel.
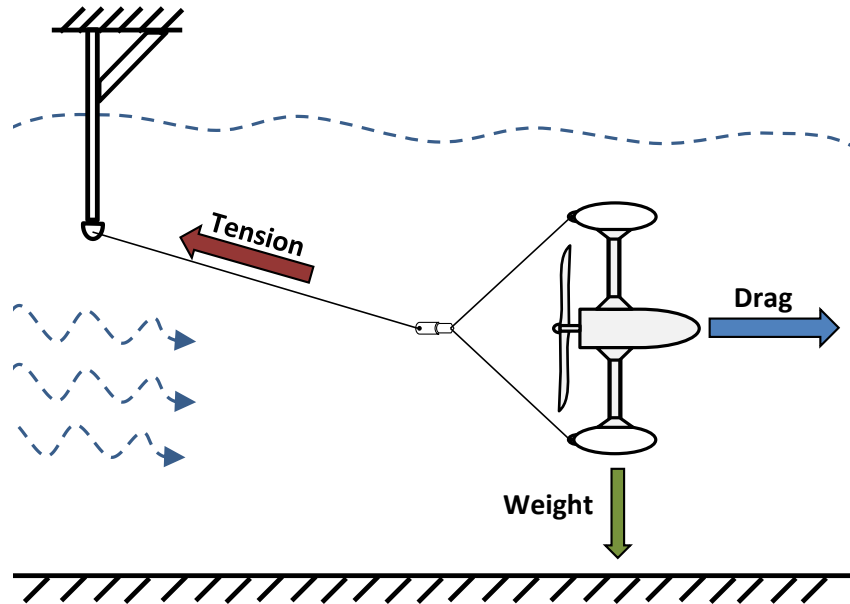
Figure 27: Water tunnel mooring setup with net forces. The mooring line is attached to top of the tunnel to provide additional upwards force to counteract the weight of the turbine.

The geometry used for the buoy and part of the nacelle came from the design of a low drag zero lift aerostat which is a zero incident body of revolution. The profile can be represented by a piecewise function to form a profile which is then revolved around a central axis. Kale et al. [85] generated this profile, known as the GNVR profile, from numerical modeling

and comparisons to existing aerostat designs. The profile consists of a circle, ellipse, and a parabola to form a fairly continuous low drag profile. It should be noted that the primary application of this profile places the aerostat in wind speeds of 0.1 $Mach$ and altitudes of 1 km. Given these conditions and assuming a length of 10 m for the aerostat, the Reynold's number defined as:

$$Re = \frac{vL_b}{\nu},\tag{14}$$

gives a value of 33×10^6. Where L_b is the total length of the revolved body and ν is the kinematic viscosity of the fluid. When compared to the conditions present in the water tunnel, the Reynold's number approaches 115×10^3 with a buoy length of 12 cm, maximum design flow velocity of 0.963 m/s, and the kinematic viscosity of 1.004×10^{-6} m^2/s at $20°C$. Although there is a significant difference in the initial conditions developed for the GNVR profile and the conditions present for water tunnel, Young [86] showed through the conservation of momentum that, a streamlined body of revolution with a length to width ratio of $3.25 : 1$ and a Reynold's number in the order of 10^6 has a total drag coefficient of 0.00619 [86]. The buoy design for the turbine is fairly similar to the conditions presented by Young [86] in which it's Reynold's number is two order of magnitude different with a length to width ratio of 3. Hess and James [87] also showed that the drag on an axisymmetric body with a low drag profile is fairly insensitive to small geometric changes and that significant drag reduction cannot be achieved from simply the shape alone [87]. This agrees with the results from Young [86] in which the total friction of the body is 93.3% due to skin friction drag. Given the analytical work present in literature and the scope of this thesis, the geometry selected is appropriate for a low drag zero lift profile for the buoys. Future work being conducted on the counter-torque mechanism will require a more rigorous numerical approach for determining the optimal profile for the specific conditions present. The profile for the buoy is shown in Figure 28 with L_b representing the length and D_b representing the largest diameter of the buoy.
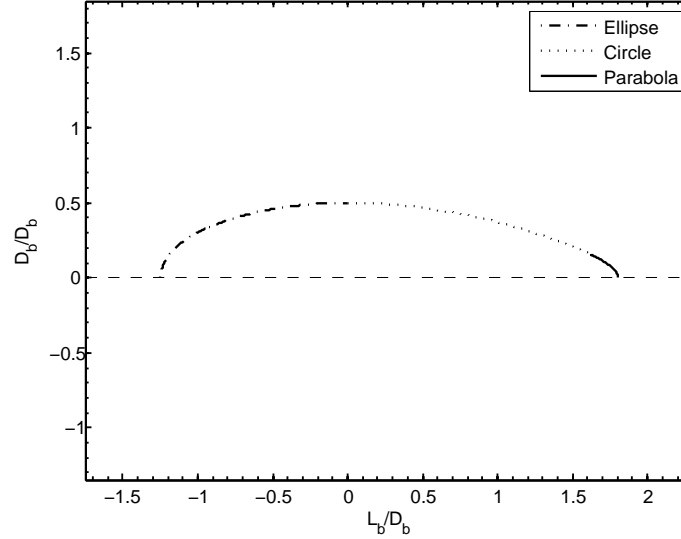
Figure 28: The combination of simply geometries allows for the delay of the transition and separation point of boundary layer which reduces the drag on the structure.

The equations which produce the GNVR profile have specific domains to allow for a near continuous function. During the application of this profile a discontinuity was discovered along with a few mathematical errors. These have been corrected for by modifying the equations from the originals [85]. A constant is added at the end of the parabola equation to mitigate this discontinuity. The constant is based on the operation of the 3D printer to ensure that the discontinuity is smaller than the accuracy of the printer head. The domains of the functions are also shifted to ensure that the profiles are situated in the correct order. The equations and their domains can be seen in Table 7 where x represents the positioning along the x-axis length.

Table 7: Equations for each section of the GNVR profile, small redesigns are required due to two mathematical errors in the original paper [87]

Section	Equation	Domain
Ellipse	$\dfrac{x^2}{1.25D^2} + \dfrac{y^2}{0.5D^2} = 1$	$-1.25D < x < 0$
Circle	$x^2 + (y + 3.5D)^2 = 16D^2$	$0 < x < 1.62D$
Parabola	$(y - 0.000152)^2 = 0.1373D(1.8D - x)$	$1.62D < x < 1.8D$

Two components of the turbine system utilize the GNVR profile, the buoys and the nacelle. From the profile outlined in Figure 28, a revolution about the x-axis produces the geometric shape for the buoys. The internal cavity is hollowed to allow the counter-torquing material to be stored inside. The nacelle consists of 2 subsections, 1) the cylinder fixture for the generator and 2) the back 50% of the GNVR profile, consisting of the circle and parabola sections. This is to allow a smoother transition from the cylinder fixture and to allow for a delayed separation of the flow. With the geometry of the buoy established the remaining components involved in the operation of the turbine are investigated.

3.3   Design components and parameters

Typically a large scale HKT have custom designed generators and turbine blades. These components are custom built to match as closely as possible to the flow conditions and load requirements. Given the extensive cost and time that would be necessary to employ such a method, an alternative approach is taken which is to find an off the shelf generator and turbine blade with similar operating conditions to the water tunnel.

3.3.1   Generator selection

The internal electromechanical design of generators are similar to motors, as a result a series of DC motor were put under preliminary tests in the water tunnel to measure their performance and determine their operating range underwater. The test setup involved the use of a fixture constructed out of 2" by 4" wood and a foam insert to secure the motor in place. The effect of water on the motors is of primary concern since they are not designed to operating fully submerged. A variable resistor is used as a load to change the current drawn from the generators. A total of five different motors were tested, Figure 29 shows the test setup in which each motor was fixed to during the preliminary tests.

From the results, all of the generators operated satisfactorily when fully submerged but

Figure 29: Preliminary generator tests to determine their functionality and operating range underwater. Note, flow traverses from bottom left corner of picture to the right edge, the red rotor blades are mounted on the motor being tested.

lacked the strength in their permanent magnets to absorb any considerable amount of the dynamic torque from the flow. Based on the preliminary tests, a higher torque generator is required which led to the search for a DC gear-motor. From the characteristic curves of the Pittman DC gear-motors, the dynamic torque from the flow, and the expected RPM range for the generator, the GM8212-21-SP 19.1 VDC gear-motor model is the most viable option for the prototype RHT. The data sheet [88] lists its continuous torque output of 0.122 Nm at 0.68 Amp with an angular velocity of 202 RPM and a gearbox efficiency of 73%. When compared to the expected torque derived from the rotor blades based on a torque coefficient of 0.1, a rotor area of 0.198 m^2, a fluid density of 1000 kg/m^3, and a flow velocity of 1 m/s, the rotor torque is 0.153 Nm at an angular velocity of 361 RPM. Section 4 presents the experimental results in which the range of the generator is evident as it captures roughly 50% of the complete power curve of the turbine. When compared to the alternative options this model approaches the torque and RPM range of the turbine the closest. A critical preliminary test that this model passed is having the capability to absorb enough torque

from the flow such that at 0% CTC (where only water is present in the buoys) the turbine system rotates continuously around its central axis due to the lack of a counter-torque. This is due to the generator's torque capacity being greater than the counter-torque. This is necessary to ensure that the generator being selected can produce enough torque in the system for the counter-torque mechanism to be necessary for stability.

Figure 30: GM8212-21-SP gear-motor is used as the generator, it operates on 19.1 VDC with a continuous torque output of 0.122 Nm which is 18% less than the input torque from the rotor.

Figure 31: White lithium grease with a consistency grade No.2 is substituted for the existed grease on the steel gears due to rust developing and locking the gears together.

3.3.2   Turbine selection

Ideally designing a custom turbine for the conditions present in the water tunnel would provide the most relevant performance from the turbine system. Due to the scope of the project, the rotor is selected as an off the self item due to the depth of design work that is involved in developing a custom turbine blade. The design of turbine blades uses the conservation of momentum and blade element theory to produce a control volume around a momentum disc. Work is done by the flow onto finite segments of the rotor blade in which the summation of the segments represent the total interaction of the rotor blades with the surrounding flow. A few assumptions regarding this method is taken:

- incompressible, inviscid, steady state flow

- no cavitation

- hydrodynamic forces determined by the characteristic lift and drag on the rotor geometry

- finite blade elements are two dimensional with no interaction between the elements

The combination of the conservation of momentum and the blade element theory is grouped under the Blade Element Momentum theory in which the analysis of both wind turbine blades and HKT blades are performed. The development of turbine blades is done through the use of commercial and research based numerical programs that perform the calculations on the blade geometry such as its twist, chord length, and airfoil profile [89]. Previous experimental work done by Shahsavarifard et al. [81] on a red 8 *inch* diameter blade from KidWind Project Inc. provided a reliable opportunity to adopt the same rotor blades for this project [90]. From contacting the engineering department at KidWind Project Inc., it is determined that the blade was experimentally designed in a wind tunnel with various airfoil cross-sections and blade twist until a high RPM low torque design was achieved.

Figure 32: Rotor has twisted and tapered blades. From observations on the surface finish and residual plastic stubs, the manufacturing process most likely involved injection molding.

With a reliable rotor and generator selected, the 3D CAD model of the turbine system can be developed. The model will need to accommodate the clearances and tolerances of the fixed components, such as the rotor and generator, and provide the mounting platforms for the corresponding sensors that will be used to collect data on the turbine's operation.

3.4   Prototyping

The structural components of the turbine system are designed in SolidWorks 2012 which are then 3D printed on a 3D Systems Projet HD 3500 with a custom evolved variation of SLA material known as VisiJet Crystal [91].

3.4.1   Computer aided design

The turbine components that requires 3D modeling include the:

Nacelle Which houses the generator and has mounting plates for the sensors.

Spokes Connecting the buoys to the nacelle and giving a moment arm for the counter-torque.

Buoys Designed by importing the GNVR profile, from Section 3.2.3, and creating the threads for the end caps.

Buoy end-caps For closing off the cavities in the buoys and the central nacelle ballast.

Each component is designed separately with interface surfaces which allows them to fit together. During the modeling process several factors where put into consideration including:

- Structural strength and durability of the system from exposure to flows up to approximately 1 m/s and minor impacts on the water tunnel inner walls.

- The density of material and the impact of central cavity on its buoyancy.

- Mounting fixtures for the sensors to be integrated into the nacelle with an ideal location for minimal impact and simplicity.

- Electrical conduit for generator and sensors.

- Printing platform and size limitations.

- Water-tight cavities for buoys and nacelle with use of o-rings on the end-caps.

Approximately four different iterations of this model were created as each one underwent revisions with recommendations from technical staff and as new knowledge regarding the system components became available. The design components are illustrated in Figure 33 and further details of each subcomponent is described in Table 8. The use of standard off the shelf parts and metrics were used to simplify the construction of the prototype. The only exception was the blade adapter which was custom designed to interface between the generator shaft and the rotor blade.
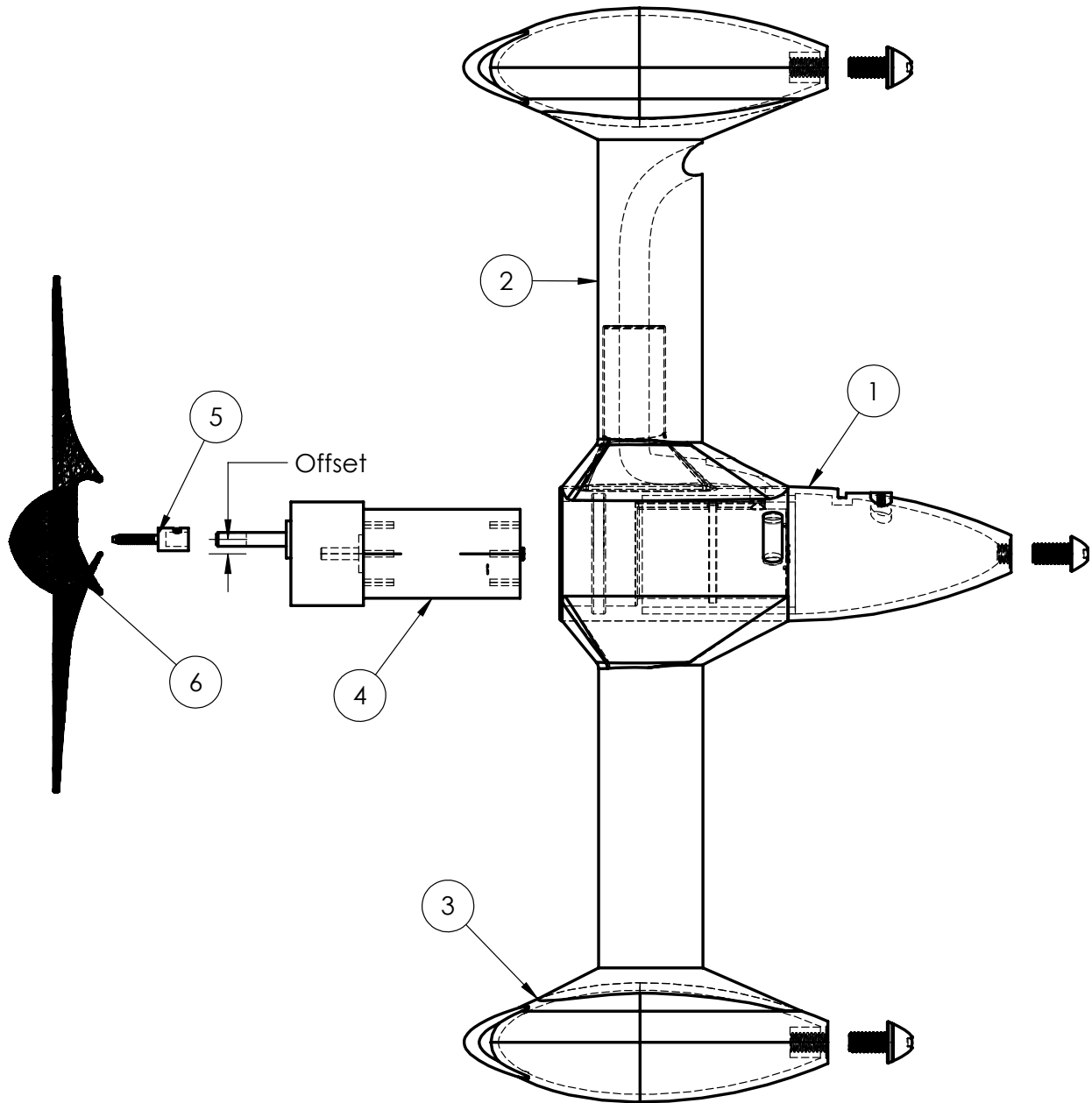
Figure 33: Assembly of turbine system with all of the mechanical components. Scale 1 : 2.22. Note the slight offset of the generator's gearbox in relation to the central axis of the turbine system.

Table 8: Outline of major turbine components and their specifications. Not to scale.

Prototype Part	Description
	1. Nacelle: Central fixture for the generator has two O-rings slips inside and a slotted path for electrical cables. A tolerance of 0.3 mm is given for generator fixture with the gearbox situated flush with the front end of the nacelle. The back end of nacelle is hollowed out for 25% added buoyancy by mass. A mount for a 6 degree of freedom inertial measurement unit is integrated on the back of the nacelle with two tapped holes for plastic bolts. With the give print area on the 3D printer the nacelle, bottom spoke, and bottom buoy are all printed as a single piece.
	2. Spokes: Supporting spokes connect each counter-torquing buoy to the nacelle hub. A central cavity runs through the top spoke for electrical cables to pass through in order to minimize external mounting structures. The spoke profile consists of a NACA 0030 airfoil with a 35 mm chord length. The end pieces of the spoke gradually transition to the nacelle body on one end and the buoys surface on the other. The bottom spoke is 3D printed as one piece with the nacelle while the top spoke has an indented cavity to allow a supporting mount from the top of the nacelle to connect to.
	3. Buoy: Located at the end of each spoke at equal distances away from the turbine axis or rotation. Each buoy is hollow with a 2.5 mm wall thickness, the access port has a 1/4-20 threaded cap with an o-ring insert to minimizes any water from leaving or entering the cavities. The geometry of the buoy is modeled after an aerostat, designed for zero lift and low drag applications. An anchor point is embedded into the front end of the buoy for connecting the mooring line.
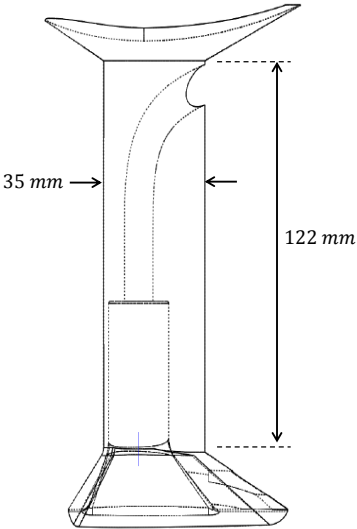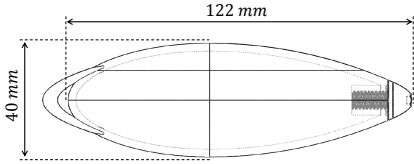
Prototype Part	Description
76.8 mm, 34.8 mm	**4. DC Generator**: A Pittman DC gear-motor is used as a generator, it operates on 19.1 VDC at 396 RPM providing continuous torque at 0.68 A. Its losses present themselves through friction, gearbox losses, and copper losses. The terminal resistance, R_a, is measured at 11.3 Ω along with a gear efficiency of 73%. Based on its characteristic curves from its data sheet, this generator is the best off the shelf item in to capture the operating points that represent the performance parameters of the turbine system.
15.2 mm, 10.2 mm, 7.6 mm	**5. Blade Adapter**: A custom design for the blade adapter fabricated out of stainless steel to avoid the oxidization with the strength of steel. A small set screw fastens the adapter onto the generator shaft while a left handed screw holds onto the blade.
10.1 mm [4 inches]	**6. Turbine rotor**: Experimentally designed 8 $inch$ nominal diameter rotor blades from KidWind Project Inc [90]. Initially designed for wind application, it can be successfully adopted for hydrokinetic applications as well with a power coefficient within the operating range of water tunnel [81]. Three blades with gradual twist towards center hub fabricated from durable waterproof plastic.
	Anchor Line: The ball joint connects the mooring lines together from the anchor points to the main mooring line attached to the top of the water tunnel. An off the shelf items are used for the ball joint and the mooring line which has a capacity of 350 N; a figure 8 knot ties each end of the mooring lines to the anchor points. The turbine system is able to rotate 360° as a result of the ball joint.
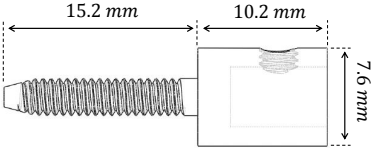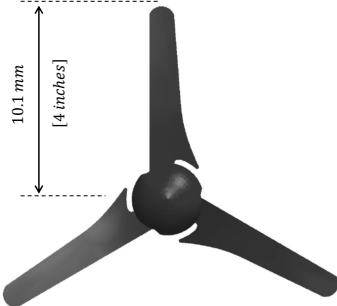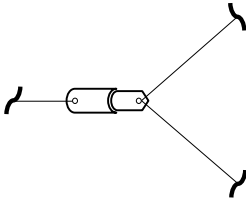
3.4.2   Rapid prototype

The process of 3D printing is different from the traditional milling, CNC, or lathing techniques which have been in use much longer. Most of the traditional techniques use a removal method of taking off material from a solid block until the desired shape has been achieved.

The 3D printing process involves taking the CAD model and breaking it down into separate slices which is laid down by the printer one layer at a time. Two solutions are used during the printing process, one for the model material and the second for a support material which provides underlying structural strength in areas where the prototype has over hanging parts or hollow cavities. Once the model has been built, the support material can be removed in the post-processing stage by various techniques based on what the support material consists of. For the 3D printer used in this project the final prototype is encased in a layer of support material, the post-processing step involves heating the entire encased model to the melting temperature of the support material. The model material has a melting temperature slightly higher than the support which allows the removal of the support without damaging the model. The two stages of this process can be seen in Figures 34 and 35.

Figure 34: Right after the structure was removed from the 3D printer, note that the model itself is encased inside of the support material for structural support during the additive process

Figure 35: After the post-processing the support material melts off, the model is spray painted white.

4   Experimental methodology

The experimental tests provide a method to determine the performance of the counter-torquing mechanism based on a set of metrics. The tests are carried out in a water tunnel at the University of Manitoba in which data on the RPM and voltage output of the turbine are collected by a DataTaker acquisition unit. The inclination angle is monitored and processed by an Inertial Measurement Unit (IMU) which is controlled by an Arduino microcontroller. Post-processing is carried out in MatLab in which data from the acquisition system and microcontroller are temporally aligned together to determine the counter-torque .

4.1   Setup

The setup of the experiment is illustrated in Figure 36 where the tethered RHT prototype is kitted in the water tunnel. The voltage output and communication lines of the IMU are extended from the prototype to the DataTaker and Arduino microcontroller.
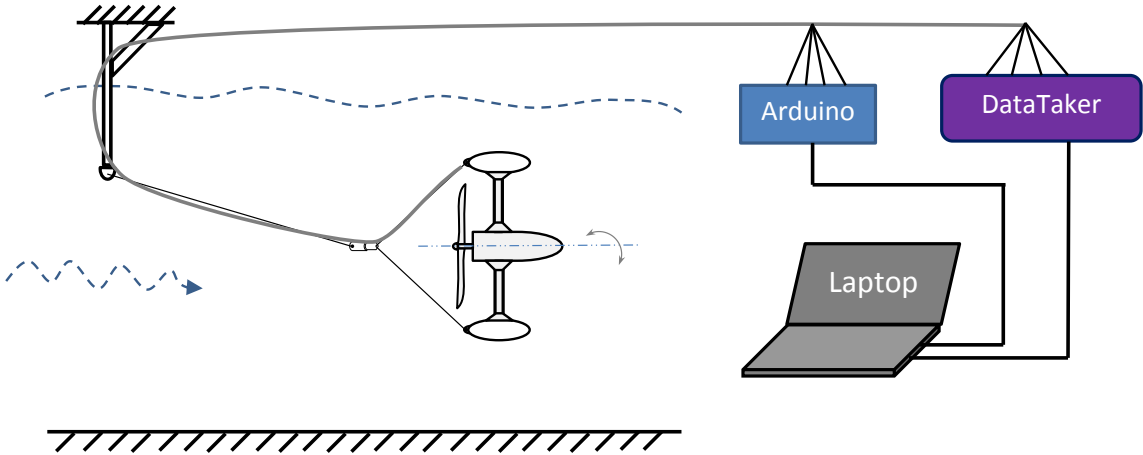
Figure 36: Overall experimental setup with the Arduino microcontroller operating and recording the IMU and the DataTaker recording the RPM and the voltage output of the generator.

4.1.1   Water tunnel

The closed circuit water tunnel was designed by Engineering Laboratory Design Inc [92]. A 30 HP, 1800 RPM AC motor is connected with a belt drive to a single stage impeller inside the water tunnel which is driven by a variable frequency drive with a $0 - 60\ Hz$ range and a 0.1 Hz resolution. The open top test section has clear Plexiglas walls with dimensions of 0.61 m in width, 0.61 m in height, and 1.83 m in length. A dimensional illustration of this can be seen in Figure 21. The design of the water tunnel allows for a variable water level height which changes the cross-sectional area of the flow region and consequently the flow velocity at a given input frequency. At the maximum water level height of 0.61 m the tunnel operates at a maximum flow velocity of 1.1 m/s. Calibration of the flow velocity and the tunnel's variable frequency drive is done through the use of an Acoustic Doppler Velocimetry unit. Figure 37 shows the linear calibration of the variable frequency driver and the water tunnel controller.
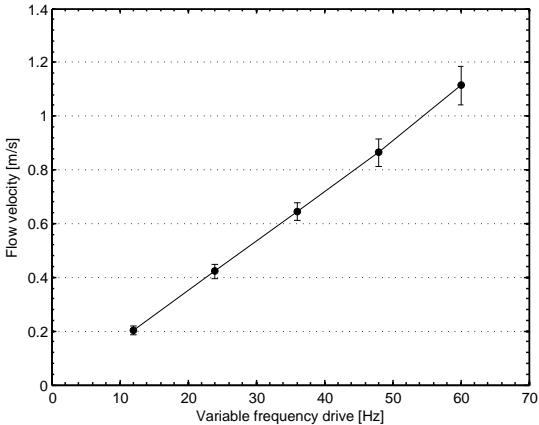
(a) Calibration plot   (b) Water tunnel controller

Figure 37: Preliminary testing of the water tunnel's frequency driver and overall operation is required to evaluate the final uncertainty of the experiments.(a) Calibration of the tunnel's frequency driver with the flow velocity indicates that at the maximum flow velocity the turbulence intensity is less than 4%. (b) The water tunnel's variable frequency drive has a range of $0 - 60\ Hz$ with a resolution of 0.1 Hz. The motor running the tunnel can reach its designated speed within 1.5 $mins$.

The mooring anchor point for the turbine system is constructed out of aluminum extrusions which are fastened to the top edge of the water tunnel test section with C-clamps. The

aluminum extrusions allow the anchoring point three degrees of freedom in the x, y, and z direction. A 350 N capacity fishing line acts as the mooring line which is feed into a fishing rod guide that is epoxied onto the end of the aluminum extrusion. The strength of the fishing line is selected based on a simple drag calculation which assumes the entire projected area to be a combination of a disk for the turbine rotor and two rectangular plates for the top and bottom buoy-spoke pair. The drag coefficient is taken to be 1.1 with a total projected area of 0.0424 m^2, a flow velocity of 1 m/s, and a fluid density of 1000 kg/m^3 [93]. The total force on the approximated structure is 23.32 N. This results in the fishing line having a FOS of 15. The extra security in the mooring line is crucial as loosing the RHT prototype can severely damage the water tunnel's impeller.

4.1.2   Data acquisition

The fastest sampling frequency of 10 Hz for the DataTaker is influenced by the measurement time, processing time, communication time, logging preparation time, and writing time [94]. The generator output is connected in series with a variable 35 Ω rheostat load; the DataTaker is connected in parallel with the rheostat in order to measure its voltage drop. The DataTaker also records the counter from the reed switch which is activated by three neodymium magnets positioned on the rotor shaft. Data collected from the DataTaker is exported into a comma separated values format which is processed by Matlab 2013a. The Arduino's sampling frequency is similar to the DataTaker in which it is not manually controlled but instead samples at the highest frequency possible given the complexity of the code and the amount of processing power it has [95]. For the conditions in place for the experiment the microcontroller has an average sampling frequency of 60 Hz. Figure 38 illustrates the programmable data acquisition unit and microcontroller. An output monitoring setup is used on both the DataTaker and Arduino in order to troubleshoot problems simultaneously as the turbine operates. This technique also allows to visually inspect the operational condition of the turbine while comparing it to the recorded data on the output

monitor.

(a) DataTaker
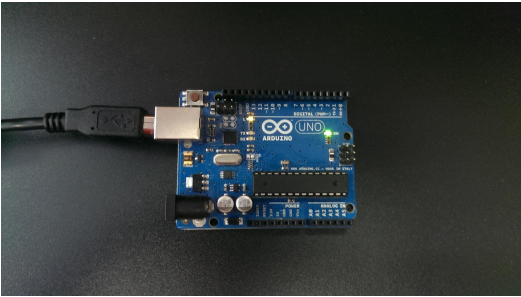
(b) Arduino microcontroller

Figure 38: The DataTaker acquisition unit and the Arduino microcontroller are used for this experiment due to the familiarity and their availability. (a) The DataTaker is designed for rugged use in field experiments. (b) The Arduino Uno microcontroller clocks at 16 MHz for its processing speed and has a 5 V operating voltage for its input/output ports.
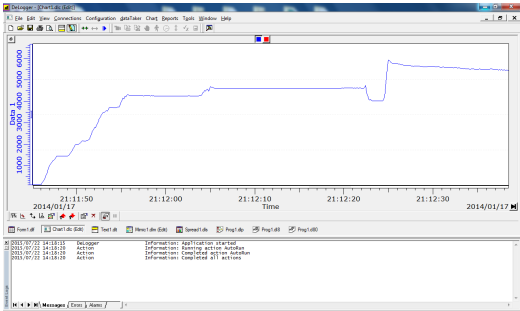
(a) DataTaker screen
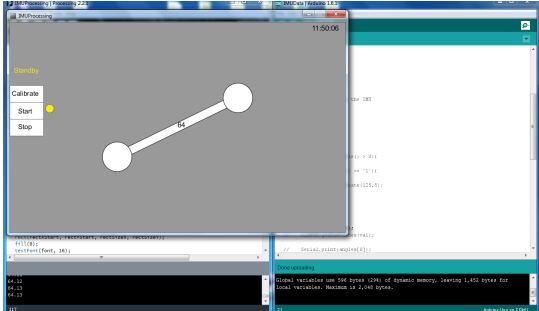
(b) Arduino screen

Figure 39: Observation of live turbine performance parameters gave the opportunity to assess and troubleshoot problems more efficiently. (a) The voltage output is monitored during each stage of the tests performed. (b) Arduino output fed into a custom in-house Processing code to store data onto a text file while simultaneously displaying a real time animation of the turbine's inclination angle.

An in-house Matlab program is written to extract, synchronize, process, and post-process the data collected by the DataTaker and the Arduino. The sensors used to perform the measurements on the turbine underwent a series of tests to determine their compatibility with the operational condition of the turbine while submerged underwater.

4.1.3   Sensors

The sensors used to collect the data include the:

IMU The six degree of freedom ITG3200/ADXL345 series IMU consists of an accelerometer and gyroscope to compensate for each others limitation, it has an operating range of $\pm 2000°/sec$ and $\pm 16\ g$ which measures the angular velocity of the turbine.

Reed switch The $MK24 - C - 1$ Meder Electroincs reed switch with a $5\ kHz$ operating frequency measuring the RPM [96]. The reed switch operates at several orders of magnitude faster than the RPM of the rotor shaft which has an average frequency of about $8\ Hz$.

Mounting brackets for the sensors are integrated onto the nacelle of the turbine during the design phase. Braided and shielded chassis wiring transfers the measurements from the sensors to the DataTaker and Arduino for monitoring and storage. Figure 40 illustrates the reed switch and IMU scale, both have 3D printed mounts.
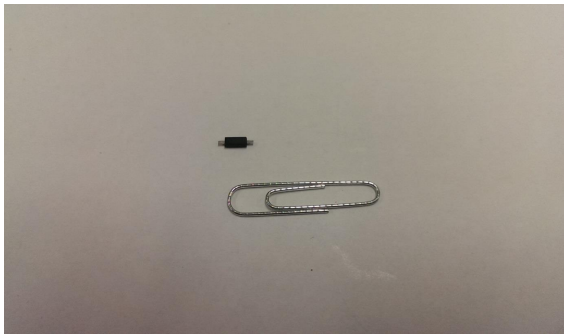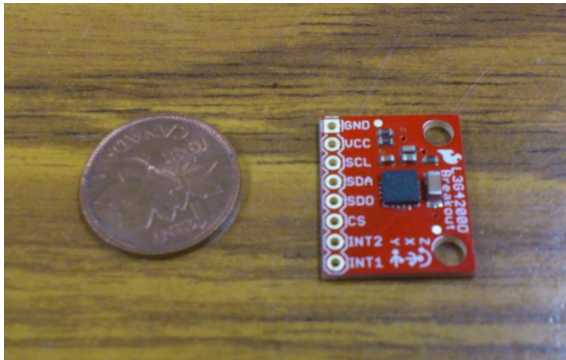
<table>
<tr><td>(a) Reed switch</td><td>(b) IMU</td></tr>
</table>

Figure 40: Sensors used for collected data on the RHT prototype operational condition. (a) A fully sealed reed switch toggled in the presence of a minimum magnetic field strength of 4.1 mT is used to collect data on the RPM of the rotor shaft. (b) The IMU collects the angular inclination of the system which processed and controlled by the Arduino microcontroller, waterproofing the sensor is necessary.

The reed switch is toggled by the presence of three neodymium magnet attached to the rotor shaft. The design of the reed switch requires a magnet with a minimum field strength of 4.1 mT [96]. This field strength is on the same order of magnitude as a household magnet

which allows a good versatility in magnet selection and positioning as a magnet with a stronger field can be placed further away [97]. The reed switch, illustrated in Figure 40, is fully sealed which allows it to be submerged underwater without complications regarding its operation. Preliminary tests established the appropriate distance and magnetic field strength for consistent switching of the reed switch.

The six degree of freedom Inertial Measurement Unit has two separate sensors that each have three degrees of freedom. An accelerometer and a gyroscope are combined together with a fusion filter to provide the benefits of each sensor while mitigating the drift and noise typically experienced by the sensors when used separately [98]. The accelerometer measures acceleration in the x, y, and z direction while the gyroscope measures the inclination angle of the mounting platform in the same three degrees of motion. The transmission lines of the IMU are fed through the electrical conduits designed into the top spoke of the turbine structure. The sampling rate and a low pass filter integrated into the IMU and can be adjusted from the registers coded by the microcontroller. A sampling frequency of 1 kHz with a low pass cut off frequency of 20 Hz is determined to be appropriate from experimental tests.

4.2   Metrics

To measure the performance of the scaled RHT prototype, several coefficients are analyzed which represent the capacity of the turbine's rotor and the counter-torquing mechanism. These coefficients include the power coefficient, Counter-Torque Flow Coefficient (CTFC), and the Counter-Torque Rotor Coefficient (CTRC). The power coefficient has been introduced in Appendix B.1 while the last two are derived in this section. The parameters that influence these coefficients are varied individually to determine their influence on the performance coefficients. These functional parameters include the flow velocity, the CTC, and the resistive load on the generator.

4.2.1   Performance coefficient

The efficiency a rotor and generator system, as described in Appendix B.1 and B.2, can be broken down into its subcomponents of fluid dynamic efficiency, gearbox efficiency, and electrical efficiency. Each subcomponent efficiency is determined with a focus on the counter-torque mechanism and the power coefficient. The analysis of the drive train or electrical efficiency is not an objective. The well established power coefficient is used to indicate the operating range of the RHT prototype and its overall efficiency [44, 75, 99, 100].

The coefficients for evaluating the counter-torque mechanism are non-dimensionalized to allow for comparisons to future tests. By comparing the counter-torque mechanism to the rotor torque and the dynamic flow torque, two non-dimensional parameters can be established. The CTFC is the ratio of the counter-torque to the flow torque, represented by C_f^c.

$$C_f^c = \frac{T_T}{T_f} \tag{15}$$

Similarly, the CTRC is the ratio of the counter-torque to the rotor torque, this is represented by C_r^c.

$$C_r^c = \frac{T_T}{T_r} \tag{16}$$

Given the performance metrics, the test parameters that are adjusted to vary the operational condition of the prototype follows.

4.2.2   Test parameters

The test parameters are the factors in the experimental tests that affect the operational condition of the turbine and which can be measured by one form of a metric. As mentioned in Section 4.2, the test parameters include the water tunnel velocity, the resistive load on

the generator, and the CTC which is the volumetric percentage of how much the buoy cavities are filled with their respective counter-torquing material. Each of the parameters have a control method which can be changed manually. The flow velocity is controlled by the frequency driver on the water tunnel, as described in Section 4.1.1; the CTC is changed by measuring the volumetric space of each counter-torque material, and the load on the generator is manually varied throughout its entire range by a variable rheostat. Details pertaining to each test parameter is further investigated.

The flow velocity's upper and lower limit are experimentally determined. The lower limit is directly related to the turbines weight and the drag required to lift the turbine off the test section floor. This is a direct result of the turbine's weight, which is illustrated in Figure 27 in Section 3.2.3. If the drag on the turbine structure is lower than certain threshold the turbine will remain stationary on the bottom of the test section. The minimum flow velocity required to lift the turbine off the test section floor is experimentally determined to be $0.7\ m/s$. The upper limit is set such that the frequency driver would have the least impact on the drift of the IMU. When the flow velocity was set to the maximum value of $1.1\ m/s$, the water tunnel's frequency drivers produced a certain electromagnetic interference which caused the IMU sensor to drift from positive to negative values. The maximum flow velocity was determined experimentally to be $1\ m/s$ which has the least impact on the performance of the IMU. This issue, as mitigated as it was, presented itself to be one of the major contributing factors in the errors for the final results. Further details pertaining to this will be covered in Section 5.1.1. With the upper and lower limits established, the flow velocity is set to range between $0.788\ m/s$, 0.875, and $0.963\ m/s$.

The second parameter is the CTC which is changed by measuring the volumetric space each counter-torque material occupies. Based on the CTC set for the particular test, a fraction of the light buoy is occupied by air with the remaining volume being filled with water. A syringe and scale, shown in Figure 41a, is used to measure the amount of water that is to occupy the light buoy and satisfy the required CTC. The scale is an AE Adam ACB+ model
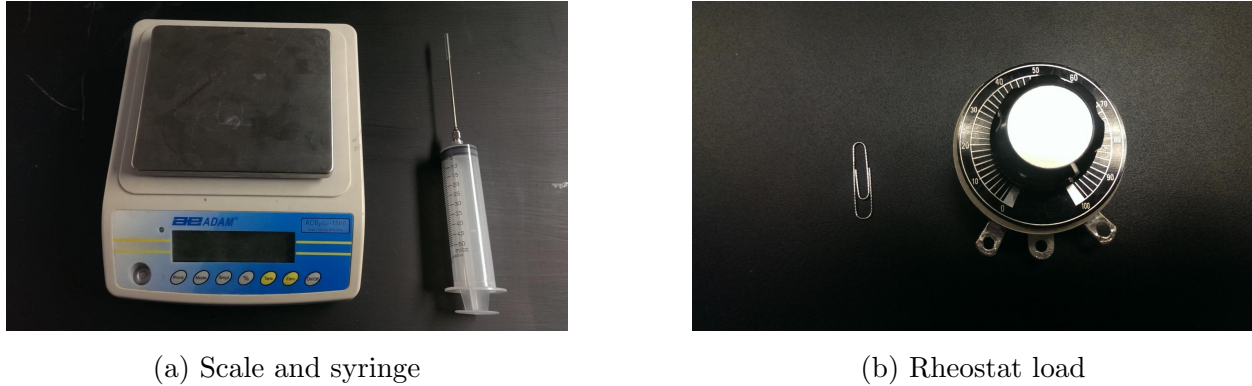
(a) Scale and syringe

(b) Rheostat load

Figure 41: Generator load is in the form of a 35 Ω rheostat. (a) Scale more measuring the masses of the stainless ball bearings and the water being inserted into the cavities. (b) Ceramic rheostat load.

with a maximum rating of 1500 g and a resolution of 0.05 g. It ran a self calibration at the start of each test, alongside the measurements being taken two times for each test. The syringe has 5 mL graduations, a total capacity of 140 mL, and an extended needle tip made out of plastic tubing. The air that is in the light buoy is at atmospheric conditions with a density of 1.205 kg/m^3 [82] and the water is at a density of 1000 kg/m^3 [101]. The heavy buoy's ball bearings are volumetrically measured based on their mass and density. The ball bearings have a diameter of 3.175 mm with a density of 7638 kg/m^3 [102]. The required mass is measured and inserted into the heavy buoy. The remaining volume is then filled with water similar to the light buoy.

The final test parameter is the load on the generator which is controlled by segmenting the 35 Ω ceramic rheostat load into ten increments. It is capable of dissipating a maximum current of 1.195 $Amps$. Each increment is tested for a 1 min interval which is then averaged during the post-processing stage, Figure 41b illustrates the load, item number RJS35RE from Ohimte, and its relative size.

By changing the test parameters the operational condition of the turbine system get affected systematically. These operational conditions include the inclination angle of the system, the power output, the RPM of the rotor, and the height of the turbine in the water column. All but one of the operational conditions were experimentally measured. The height of

the turbine in the water column was visually recorded but not numerically measured. The quantitative results of each of the test parameters is presented in Section 5.

4.3   Test procedure

The experimental procedure involves changing each of the test parameters to vary the operational conditions of the turbine while measuring them with the data acquisitions setup. Each of the parameters were varied in stages, with the flow velocity being at the first stage, the CTC the second stage, and the load on the generator the third stage. The water tunnel's frequency driver is set to the first flow velocity of 0.788 m/s in which the CTC on both buoys is varied between 10% and 40% with 10% increments. At each CTC, the load on the generator is varied from 35 Ω to 3.5 Ω with 3.5 Ω increments. Table 9 summarizes the test procedure and the order in which the parameters were varied. It should be noted that ideally the CTC should be varied between 0% and 100% with a sensitivity test being conducted on the variability of the increments. For this project the maximum CTC was incremented to 40% due to time limitations and available resources.

Table 9: The test procedure has each parameter varied by a designated metric system.

Stage 1: Flow Velocity	Stage 2: Counter-Torque Capacity	Stage 3: Generator Load
Primary test parameter is set to one of three velocities, 0.788 m/s, 0.875 m/s, or 0.963 m/s by adjusting the Variable Frequency Driver of the water tunnel. A maximum water height of 0.61 m during zero flow is checked each time to ensure the cross-sectional flow area remained constant in order for the flow calibration to be valid.	Both the light and heavy buoy were set to the same CTC based on their volumetric space inside the cavities. The capacity was varied between 10% and 40% with 10% increments. A 63.6% packing density is used for the volume occupied by the ball bearings to account for the random spacing in between each ball [103]	A variable 35 Ω rheostat acted as the load in order to change the torque absorbed by the generator. The load is varied between 3.5 Ω and 35 Ω with 3.5 Ω increments. At low resistance settings the current would be dissipated by the generator which would behave as a electrodynamic brake.

5   Results

The results include:

1. Test case that presents the performance of the counter-torque mechanism for a flow velocity of 0.788 m/s and counter-torque capacity of 20%. This requires investigating the:

   - variations in the counter-torque and rotor torque throughout the timespan of the experiment;

   - the friction present in the system at different TSRs;

   - the angular inclination of the system at different rotor torques; and

   - the power coefficient.

2. Uncertainty in the experiments, possible sources of error, and a sample derivation of the measurement uncertainty.

3. Non-dimensionalized performance metrics for assessing the operation of the of the RHT prototype, including:

   - CTFC, the counter-torque non-dimensionalized with respect to the flow torque, investigated at varying degrees of CTC and flow velocity; and

   - CTRC, the counter-torque non-dimensionalized with respect to the rotor torque, which is also investigated at varying degrees of CTC and flow velocity.

   - power coefficient, which is the output power non-dimensionalized with the available power in the flow; investigated at varying degrees of CTC.

4. Scaling parameters for the large scale development of the RHT.

Data collected for all of the experiments is reduced to the slowest recorded sampling rate for the DataTaker at 10 Hz. It is then averaged over one minute intervals. Each operating

point for all of the experiments is held constant for a one minute to allow for the transient

conditions to settle.

5.1   Test case

The test case with a flow velocity of 0.788 m/s and counter-torque capacity of 20% is

selected due to it covering 40% of the power curve when compared to experimental results

by Shahsavarifard et al. [81] on the same rotor blade. Figure 42 shows a rotor torque which

is on average greater than the counter-torque. During the tests the inclination angle never

exceeded 90° which indicates that the stability system successfully generates enough torque

to stabilize the rotor torque. As the rotor torque increases, it innately inclines the turbine

structure which consequently produces a larger counter-torque. From Figure 42 the different

resistive loads are clear where there is a sudden rise in the rotor torque. This is followed by

a transient period where the counter-torque rises followed by a steady state period.
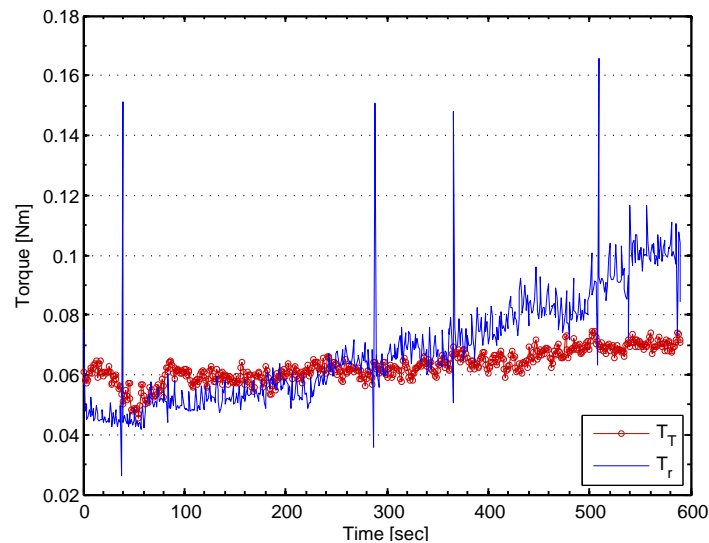
Figure 42: On average the rotor torque is greater that the counter-torque for the majority of the experiments conducted. Frictional torque present in the system provides an additional source of balancing torque for the rotor which reduces the demand on the counter-torque mechanism.

Note the increase in the viscous friction coefficient at the lower TSR in Figure 43. This

in conjunction with the increase in the angular velocity of the support structure indicating

that at lower TSRs the viscous friction increases. Figure 42 also reinforces this observation as the separation distance between the rotor torque and counter-torque increases at later times in the experiment; this corresponds to a lower TSR. Recall that the resistive load is decreased from 35 Ω to 3.5 Ω which indicates that later times periods are associated with lower TSRs. The horizontal dashed line in Figure 43 shows the averaged viscous friction coefficient from all of the experiments conducted, 0.03 Ns/rad indicated by the horizontal dashed line. This is one order of magnitude different from the analytical friction coefficient used in Section 3.2.2 due to the experimental errors encountered during the tests which are detailed in Section 5.1.1. The analytical friction coefficient of 0.1 Nms/rad properly depicts the observed operational behavior of the counter-torque mechanism.
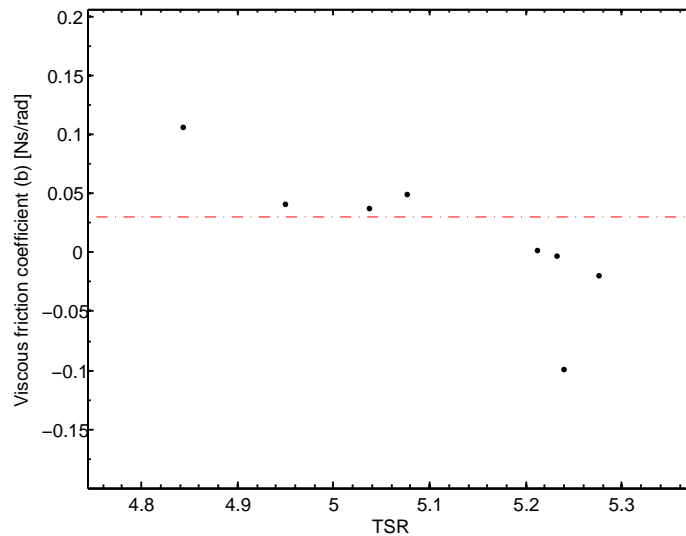
Figure 43: The viscous friction coefficient can be determined by taking the difference between the counter-torque and rotor torque and dividing it by the angular velocity of the support structure.

The numerical operating behavior of the counter-torque mechanism can be established from:

- the positive correlation between the inclination of the counter-torque system and the rotor torque in Figure 44, and

- the agreement with the counter-torque with increasing rotor torque from Figure 42.

The freewheeling operating point of the RHT is located on the right side of the power curve. As the rheostat load is decreased from the free wheeling point the amount of current drawn from the generator increases. With the increase in current, the torque drawn from the flow also increases which causes the turbine system to incline at a greater angle. Figure 44 shows this inclination increase. The maximum percent uncertainty associated with rotor torque is 61.1% with an average of 23.6%. Sources of error for the uncertainty calculations are discussed in Section 5.1.1.
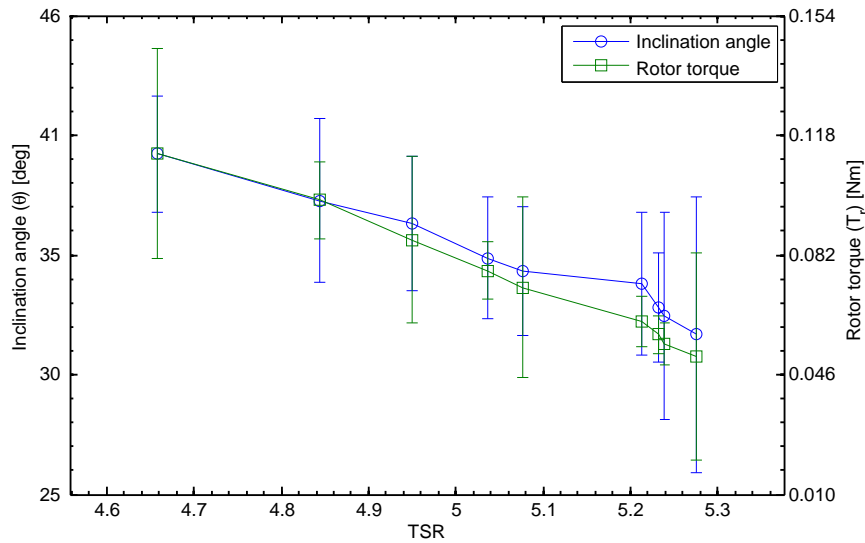
Figure 44: As the rotor torque increases with smaller TSR, the inclination angle rises to balance the torque on the rotor shaft. This depicts the behavior of the counter-torque mechanism under the full range of the generator load.

Based on the slope of the curve in Figure 45 it is evident that the turbine is operating on the right side of its power curve. In order to reach the peak and to surpass it to the left side, the generator's torque capacity and operating RPM range need to be aligned with the flow torque and the optimal TSR of the turbine rotor respectively. Based on the available motors from the manufacturer, the next higher gear ratio would have a torque capacity higher than the flow, resulting in no rotation in any flow condition. The lower gear ratio option would have a torque capacity much lower than the flow, resulting in an even smaller portion of the power curve being covered. The Guide to the Expression of Uncertainty in Measurements is used to quantify the uncertainty in the power coefficient which has a maximum value of

20.8% at a 95% confidence interval. The main reason for the high uncertainty is due to each generator load being tested in succession without stopping the data collection. This results in the transient portion of the test to be incorporated into the data analysis and contribute to the uncertainty. As a result of this, the standard deviation of one generator test will be effected by the previous test's transient period. This is one factor which may influence the uncertainty calculation along with a wide range of environmental factors that are further discussed in Section 5.1.1. It should also be noted that blockage effects, wall effects, and free surface effects were not considered in the power coefficient which would further reduce the power coefficient as blockage effects causes an increase in the local flow velocity which creates a higher than expected power output.
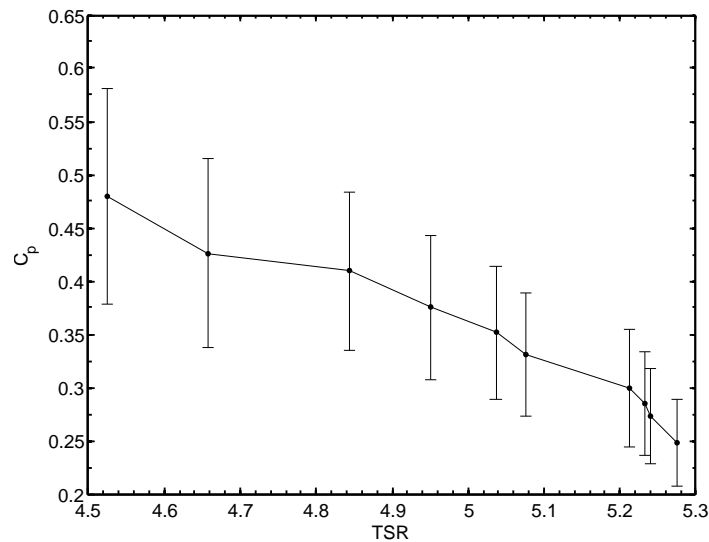
Figure 45: Power coefficient at 0.788 m/s and counter-torque capacity of 20% gives the right side of the power curve indicating that the generator torque is less than the dynamic torque in the flow.

The criteria used to determine if the selected generator is suitable for the experiments involves running a preliminary test with 0% CTC in which both cavities are filled entirely with water. If the generator can absorb enough torque from the flow, the lack of any counter-torquing force will result in the inclination of the support structure spinning in an unstable manner. This is the only criteria for selecting a generator as the primary purpose of the generator is to absorb enough torque such that a balancing counter-torque would be necessary to keep

the turbine in equilibrium.
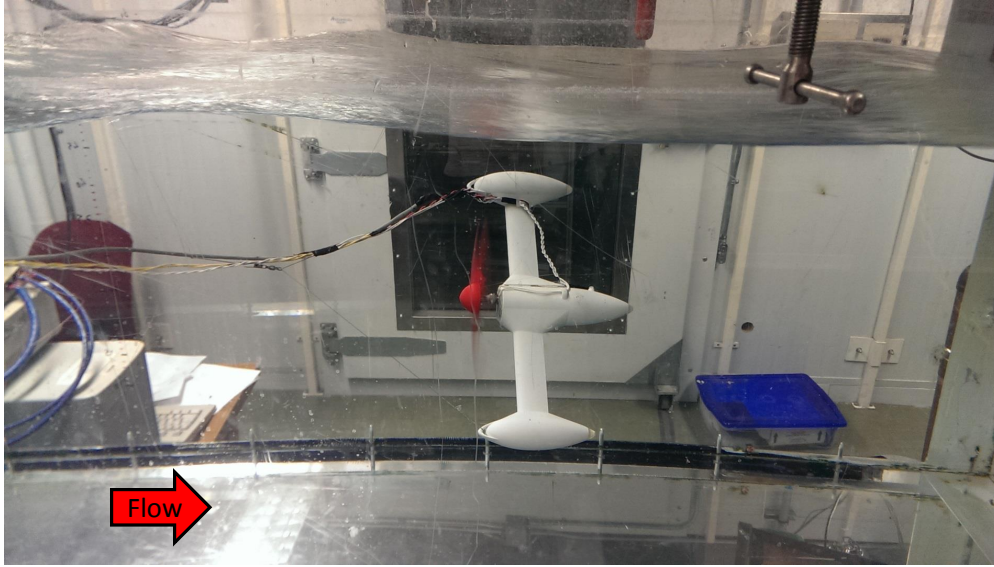
Figure 46: Experimental test with 0% counter-torque capacity, in which both buoy cavities are filled with water, resulting in the turbine system to spin continuously when the load on the generator is decreased below 20 Ω. This unstable condition indicates that a counter-torque mechanism is required for stability.

5.1.1   Uncertainty analysis

The method used to evaluate the uncertainty in the measurements is the Guide to the Expression of Uncertainty in Measurement [104]. The method of calculating the uncertainty of any calculated parameter, y, dependent on N number of measurements each with their own uncertainty is through the combined uncertainty represented by $u_c(y)$. Expressed in Equation 17, each measurement, x_i, has its own uncertainty, $u(x_i)$, that is the standard deviation of the measurement. The second order Taylor series is used to estimate the combined standard uncertainty.

$$u_c^2(y) = \sum_{i=1}^{N} \left(\frac{\partial f}{\partial x_i} \right)^2 u^2(x_i) \tag{17}$$

A sample calculation for the uncertainty for the total counter-torque produced by the system is presented. Recall, the counter-torque is the summation of the torque from the light and

heavy buoys together.

$$T_T = T_L + T_H \tag{18}$$

$$T_T = (F_L L_L \sin \theta) + (F_H L_H \sin \theta) \tag{19}$$

The combined uncertainty can be expanded upon based on the uncertainty in the parameters in Equation 19. Recall that the spoke lengths are slightly different due to the offset of the generator's gearbox mentioned in Section 3.2.1. The parameters include:

- the length of the spoke arms for the light buoy $u(L_L)$;

- the length of the spoke arms for the heavy buoy $u(L_H)$;

- the force exerted by the light $u(F_L)$;

- the force exerted by the heavy buoy $u(F_H)$; and

- the inclination angle of the system $u(\theta)$.

$$u_c^2(T_T) = \left(\frac{\partial T_T}{\partial F_L}\right)^2 u^2(F_L) + \left(\frac{\partial T_T}{\partial F_H}\right)^2 u^2(F_H) + \left(\frac{\partial T_T}{\partial L_L}\right)^2 u^2(L_L) + \left(\frac{\partial T_T}{\partial L_H}\right)^2 u^2(L_H) + \left(\frac{\partial T_T}{\partial \theta}\right)^2 u^2(\theta) \tag{20}$$

The uncertainty associated with the variables can be categorized into Type A and Type B. Table 10 categorizes the parameters in Equation 20 along with their respective values.

Type A Calculated by standard deviations of the measurement and any combined standard uncertainty

Type B Evaluated through engineering judgment and any relevant associated variance estimates available on the specification, properties, or knowledge of the measurement.

Type B uncertainties use a convergence factor of 2 which corresponds to a confidence interval of 95.45%.

Table 10: Uncertainties associated with the total counter-torque categorized based on their type. The resulting equations or process for their uncertainty is calculated.

Term	Type	Process
$u^2(L)$	B	**Spoke arm length**: Uncertainty in caliper used to measure the arm length is $\pm 2 \times 10^{-5}$ mm which translates into an uncertainty of 1×10^{-5} m.
$u^2(F_H)$	B	**Heavy buoy force**: Dependent on the buoyancy force of the stainless steel ball bearings which is dependent on the tolerance of the ball volume. The ball bearing's tolerance is 1.27×10^{-5} m which translates to 6.35×10^{-6} m with a coverage factor of two.
$u^2(F_L)$	B	**Light buoy force**: Dependent on the volume of the syringe used to measure the volume of water inserted into the buoy. Smallest division is 5×10^{-6} m^3 which translates to 2.5×10^{-6} m^3 in uncertainty with the coverage factor.
$u^2(\theta)$	A	**Inclination angle**: Measured from the IMU on-board the turbine, the standard deviation from the data collected can be used directly as the uncertainty associated with the inclination angle.

The uncertainty method employed requires each measurement be conducted in an independent test. Given the three flow velocities, four counter-torque capacities, and ten resistive loads settings, there is a total of 120 combinations for test cases. Due to time constraints, the test procedure used for this project involved varying the last test parameter in a step-wise function for one minute intervals while the remaining parameters are held constant. This results in a total of 12 different test cases, each with the resistive load varying from 35 Ω to 3.5 Ω. Figure 42 shows where the rotor torque has a step-wise variation when the resistive load is changed. The separation of each resistive load setting into its own test case is required for a more valid representation of the uncertainty analysis which should be done as a part of the future work for this project. Several other factors are involved in the contribution to the uncertainty analysis in which mitigation techniques are used to reduce their influence.

The environmental factors include:

- The variable frequency drive of the water tunnel causes electromagnetic interference that is picked up by the wires for the power lines, ground lines, and data acquisition [105, 106].

- The long cable for the data acquisition increases the capacitance in the IMU line and influences the rise and fall times of pulse width modulated signals sent over the serial data line and the serial clock line [107].

- Long cable connection causes cross-talk between serial data and serial clock line lines which can induce spikes in signal [108].

- Ground loops with the computer's power connections and the water tunnel causes the sensors to be inoperable [109]

- Internet connection interfering with the DataTaker communication lines

The electrical noise from the variable frequency drive is measured by an oscilloscope to range from 4 MHz to 10 kHz while the tunnel is operating at its maximum speed of 1.1 m/s. This electrical noise is compounded by the generator and communication lines used for the IMU, which are 1.75 m in length [105]. A shielded cable is used with the shortest possible length in order to minimize electrical noise. This technique helps reduce the problem, but not eliminate it as high frequencies are blocked by shielded cables while lower frequencies are blocked by braided cables. For the noise induced by the tunnel motor, both low frequency and high frequency noise is present. The cost for acquiring both a shielded and braided cable with enough wires for the IMU is not justifiable for the scope of this project. Figure 47 illustrates the electrical noise picked up with an oscilloscope. One probe was placed into the water and the other was left in the air.

The Arduino microcontroller and the IMU communicate over an Inter-Integrated Circuit (I^2C) connection which provides a 400 $kbit/s$ data transfer with one data signal line, one clock line, one power supply, and one ground line. The serial clock line synchronizes
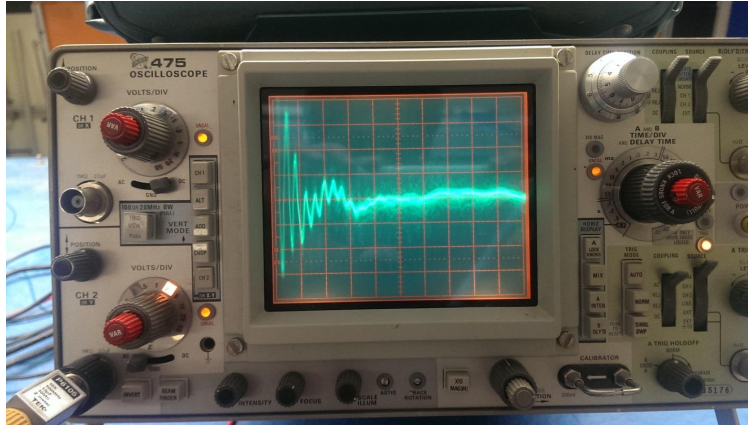
Figure 47: Electrical noise in the range of 4 MHz and lower is generated by the variable frequency drive contributing to noise on the 1.75 m length IMU data lines. The settings on the oscilloscope is set to 2 V/div and 0.5 $\mu s/div$.

the controller and the sensor together while the serial data line is for bi-directional data-transfer. The challenge with I^2C connection arises when extending the length of the lines beyond 10 cm. Special cable arrangements, circuit setup, and terminal resistance is necessary to deal with [108, 109]:

- capacitive cross-talk between the serial data and serial clock lines;

- the antenna-like behavior of the cables; and

- the ground potential difference at either end of the line.

Figure 48 shows an overview of the experimental setup with the generator, IMU, and reed switch lines extended from the prototype in the water to the data acquisition and microcontroller.

Stalling and faulty readings of the IMU are resolved by restarting the microcontroller, sometimes required after the communication lines come into contact with the water. An extensive amount of practical and research based work has been done to address grounding and noise problems, although from literature it is evident that each device setup has unique problems that cannot be fixed with a common solution [109, 110, 111]. The length of the communication line also dictates the capacitance in the line which directly affects the rise time of the
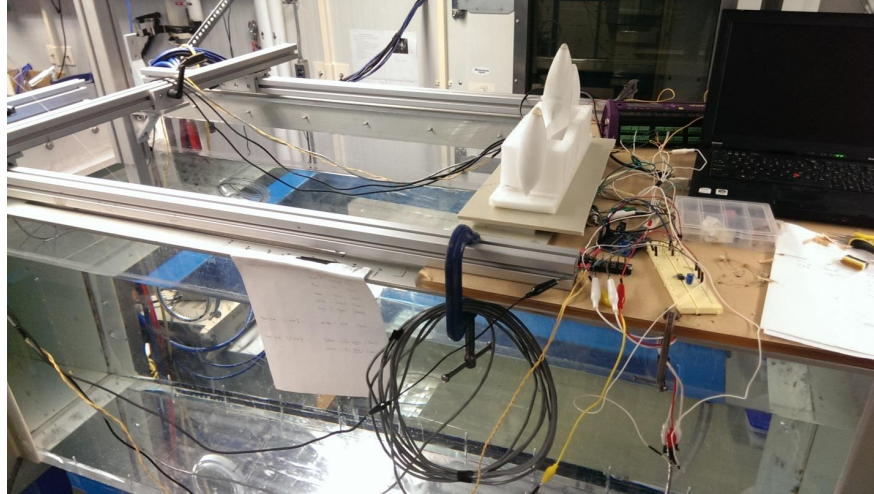
Figure 48: The experimental test setup with the aluminum extrusions clamped on the outer edge of the water tunnel for supporting the mooring line of the turbine.

signal, and this can influence the signal's integrity. The process used to mitigate these issues includes:

- placing resistors in series with the serial data and serial clock lines to reduce crosstalk and signal spikes;

- using pull-up resistors to ensure signal returns to the supply line when it not being grounded;

- filtering the signal by a low pass filter and ferrite beads;

- using a grounded foil shielding around the I^2C communication lines; and

- electrically isolating the computer and DataTaker from the power supply to avoid potential differences between the water and the computer.

These steps provided a more reliable signal integrity and presented a more agreeable qualitative observations of the turbine behavior.

Besides the microcontroller, the DataTaker is influenced by the internet connection on the laptop being used and the electromagnetic interference caused by the variable frequency drive of the water tunnel. Variable frequency noise is a common culprit for electromagnetic noise

with few solutions. One costly option is to use an inverse-sine wave frequency generators that produce the inverse PWM generated by the variable frequency driver to cancel out the noise [106]. Figure 49 illustrates the different sources of error and how they influence in signal integrity. The frequency driver causes an offset to occur in the voltage measurements while the internet results in a higher fluctuation of the voltage, seen by the standard deviation of the signal. This problem has also been experienced by technicians at the Applied Research Laboratory at Pennsylvania State University on another water tunnel [111]. Figure 49 shows the impact of the frequency driver and the interent. Mitigation techniques are used to reduce the electrical noise.

(a) Water tunnel VFD offset   (b) Internet noise
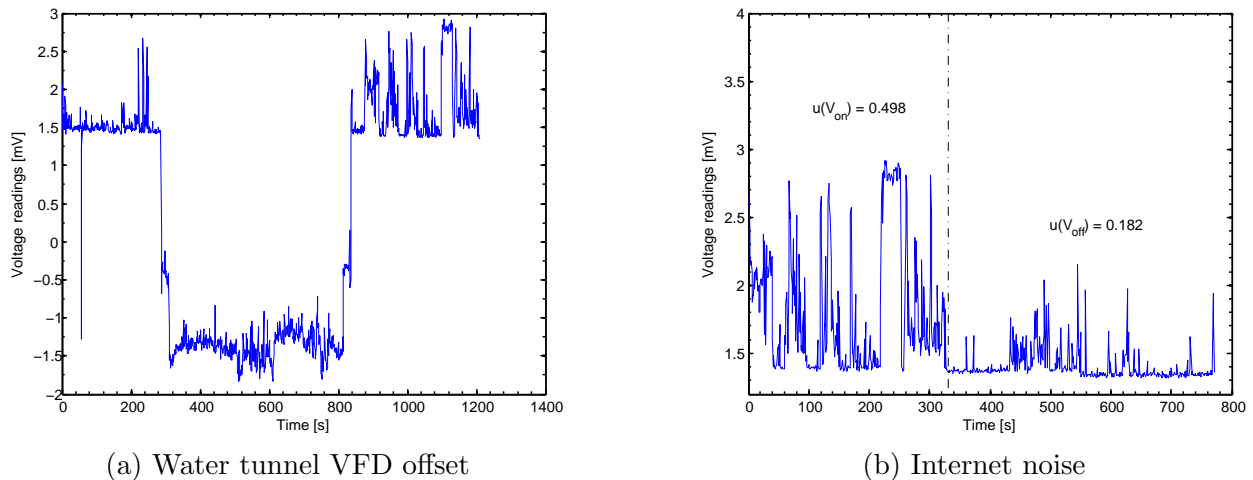
Figure 49: Noise from various environmental sources are discovered and mitigated. It is safe to assume that much of the noise present here also affected the microcontroller.(a) Water tunnel's variable frequency driver caused a voltage offset of approximately 3 mV at 1.1 m/s, this affects both the DataTaker and the microcontroller.(b) The interent, which was later turned off, causes the standard deviation of the voltage readings to nearly double.

5.2   Performance coefficient

Non-dimensional metrics are used to determine the performance of the small scale HKT developed and the counter-torquing mechanism. These are presented in Section 4.2 and AppendixB.1. The well established power coefficient is used to represent the efficiency of the rotor blade at different TSR giving the operating range of the HKT. A similar set of metrics

are developed to determine the efficiency of the counter-torque mechanism. The CTFC and CTRC are derived in a similar fashion to the power coefficient in which the torque exerted by the counter-torque system is non-dimensionalized with respect to the torque in the flow and rotor respectively. Each of the performance coefficients presented below are plotted with respect to the test parameter established in Section 4.2.2.

Flow velocity The three main flow velocities tested are 0.788, 0.875, and 0.963 m/s.

Counter-Torque Capacity Varying the CTC of the turbine to see its impact on the turbine performance.

Tip Speed Ratio Represents the operating RPM of the turbine non-dimensionalized with respect to the mean flow. Changes in the resistive loading varies the TSR.

The TSR is a standard independent parameter for measuring the performance of kinetic turbines and will represent the x-axis for all of the tests conducted. It is established from the flow velocity and the RPM of the rotor blades which is influenced by the generator load. The remaining two parameters will be shown separately.

The general performance of the prototype RHT is dependent on the non-linear relationship between the flow dynamics, the rotor blades, and the operating point of the generator [112]. When the load on the generator changes, the current drawn varies which is directly related to the torque on the generator shaft. This is seen from the rotor torque and inclination angle presented in Figure 44. A smaller generator load reduces the TSR which in turn increases the rotor torque and thus the counter-torque as well. This is considering that the operating point of the turbine is on the right side of the power curve, which is verified from Figure 45.

5.2.1   Counter-torque flow coefficient

The CTFC is the counter-torque non-dimensionalized with respect to the flow torque. It is expected that the amount of counter-torque exerted is dependent on the flow velocity and the load on the generator, while being independent of the CTC. This is the general

conclusion that can be drawn from Figures 50 to 52. As the load on the generator decreases, this lowers the TSR, and consequently the CTFC increases. The variation in the CTC does not have any impact on the CTFC since the same amount of counter-torque is required to balance the rotor torque regardless of the amount of counter-torquing material present in the buoys. Less counter-torque material, CTC, causes the system to incline at a greater angle, increasing the moment arm to produce the same amount of counter-torque. Certain cases such as in Figure 52 deviate from the expected performance which can be attributed to the errors mentioned in Section 5.1.1.

5.2.1.1   Counter-Torque Capacity parameter

The plots of the CTFC is presented with variable CTC in Figures 50 to 52. The general trend from the CTFC show the same negative slope which is indicative that as the TSR decreases the amount of counter-torque required increases. This can be explained from the operation of the generator and turbine response. The load on the generator is decreased from 35 Ω to 3.5 Ω, the decrease results in an increase in the current that flows through the load. The increase in current causes a larger torque on the rotor shaft. This is followed by a drop in RPM due to the internal resistance and the lower induced armature voltage. In response to the higher braking torque on the generator shaft the inclination angle increases until a new equilibrium point it reaches with the generator torque. The increase in the CTFC at lower TSR is synonymous with the increase in the torque coefficient in the rotor shaft.

5.2.1.2   Flow parameter

The flow velocity test parameter is varied between 0.788, 0.875, and 0.963 m/s. The CTFC is presented with different flow velocities in Figure 53. The general trend for the CTFC is a larger counter-torque is produced for lower flow velocities. This can be seen in Figure 53, where the maximum counter-torque produced by the 0.788 m/s is on average 0.0125 units higher than the 0.875 m/s flow velocity. This is a result of two features of the turbine
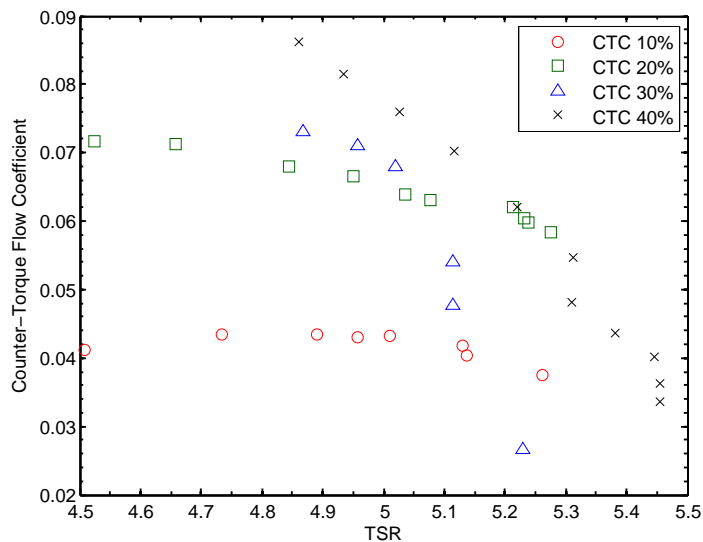
Figure 50: CTFC at 0.788 m/s, the amount of counter-torque is consistent with different CTC. This agrees with similar results seen in the torque coefficient as it decreases with higher TSR when the operating point is on the right side of the peak.
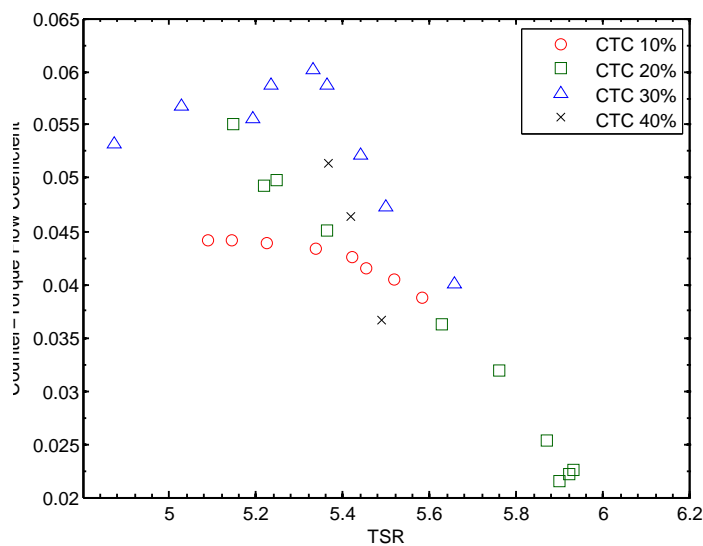
Figure 51: CTFC at 0.875 m/s, the counter-torque outputs the same torque regardless of the counter-torque capacity which follows the expected trend. The counter-torque mechanism operates correctly given the minimum capacity in the buoys are met.

operation:

1. As the flow velocity decreases the generator is able to operate at a higher torque since it can absorb a greater amount of torque from the flow.

2. At lower flow velocities the presence of friction has a larger impact by countering the
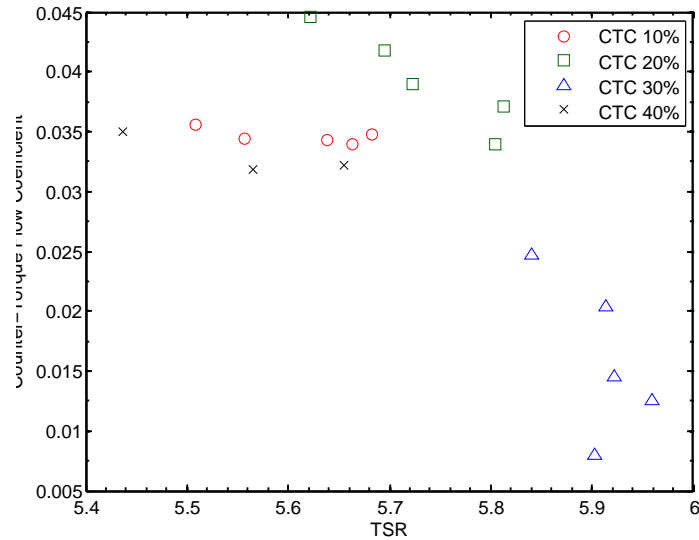
Figure 52: CTFC at $0.963\ m/s$, the counter-torque output the same general trend as expected since the counter-torque is independent of the counter-torque capacity.

rotor torque, allowing the rotor torque to operate at higher operational torque.

A higher current output indicates a larger rotor torque which results in a larger counter-torque needed for stability. This results in the trend in Figure 53 where lower flow velocities have a higher CTFC. Given this relationship, one possible method of capturing a wider range of the torque curve would be to lower the flow velocity to the point at which the generator's maximum operating torque matches or exceeds the flow torque. Based on the experimental setup and limitations though this is not possible due to the weight of the turbine which would cause it to drop to the bottom of the test section floor at any flow velocity lower than $0.7\ m/s$.

The trends seen in the CTFC is expected due to its similarity to the torque coefficient of the rotor blades. The rotor torque is balanced by:

1. The counter-torque.

2. The viscous frictional torque.

Equation 4 in Section 3.2.1 is written as a approximate equality, since at the time of designing the RHT prototype the impact of the frictional torque was unknown. The CTFC equation

(a) CTFC at 10% CTC

(b) CTFC at 20% CTC

(c) CTFC at 30% CTC

(d) CTFC at 40% CTC
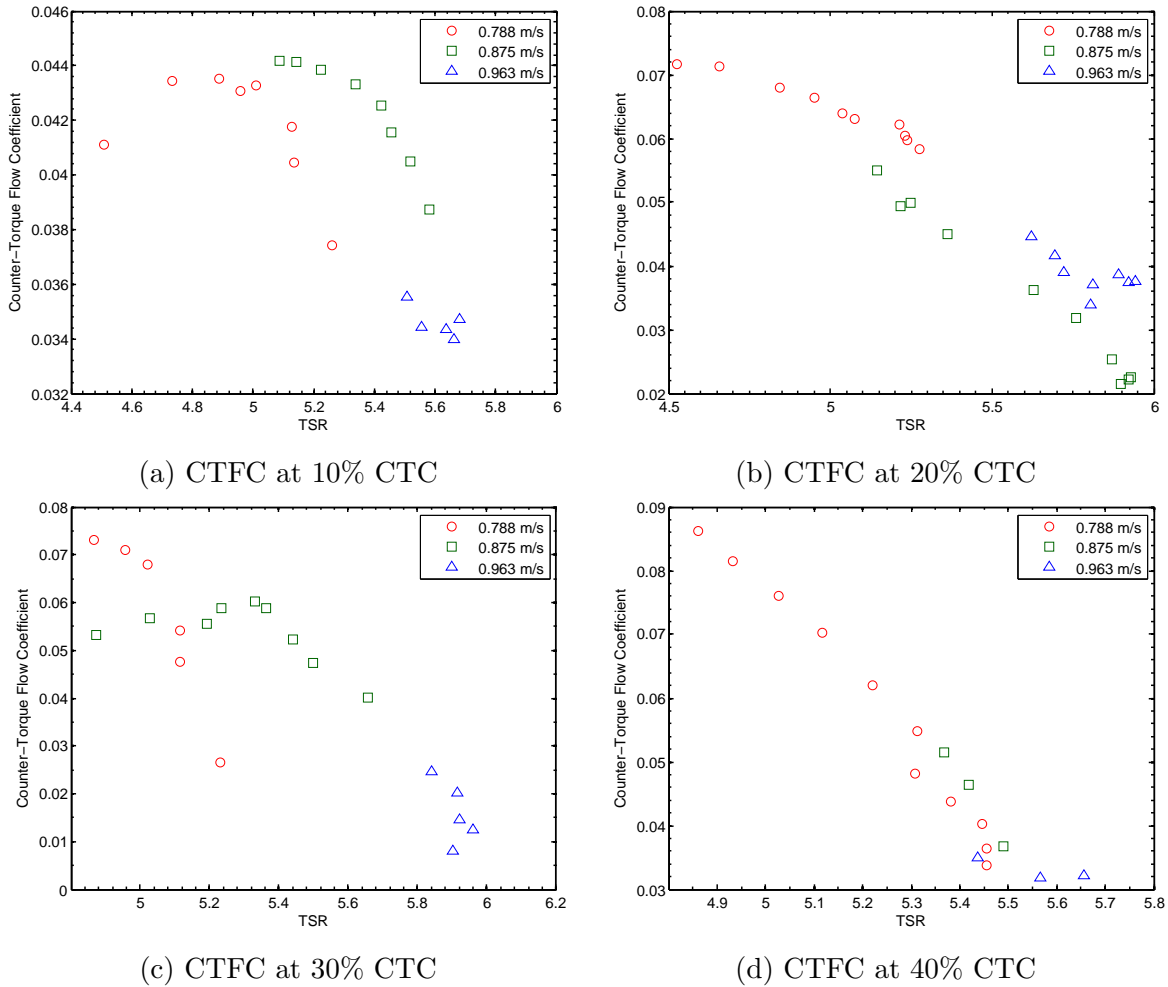
Figure 53: The general trend for the CTFCs follow a negative slope regardless of which flow velocity it is operating at. (a) The plateau at the lower TSR is a result of the generator outputting higher current values and influencing the operation of the IMU. (b) Lower flow velocities result in higher CTFC. (c) Higher flow velocities show a consistent decrease in CTFC due to the ratio of the counter-torque to flow torque decreasing. d) CTFC has less variations at higher CTC. This may be further verified in the future work when the CTC is increased to 100%.

can be re-written from Equation 15 as the torque coefficient of the rotor blades less the viscous friction term. Recall that the rotor torque measured from the generator is balanced by the counter-torque mechanism and the friction term:

$$T_T = T_r - b\dot{\theta} \tag{21}$$
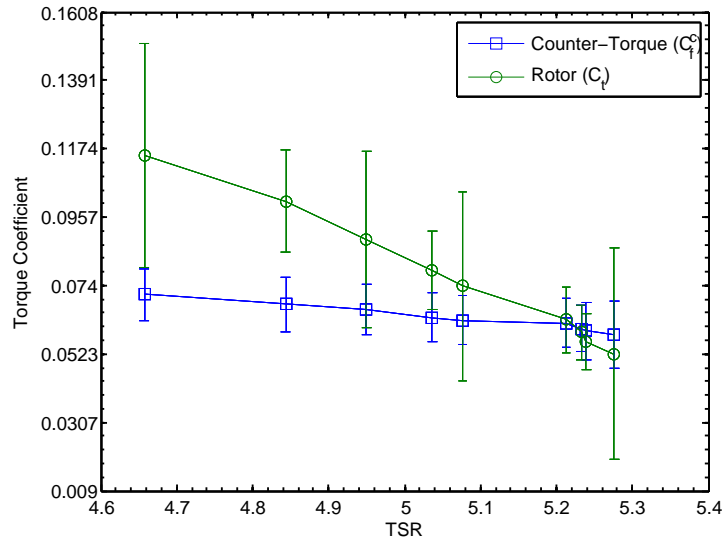
Figure 54: Comparison of the CTFC with the rotor torque coefficient at 0.788 m/s and 20% counter-torque capacity, the linear relationship with the torque rotor torque coefficient and counter-torque coefficient is the viscous friction.

Dividing both terms by the dynamic flow torque, T_f.

$$C_f^c = C_t - \frac{b\dot{\theta}}{T_f} \tag{22}$$

Experimental and analytical research show that the maximum torque coefficient for turbine rotors at a TSR above 5 is typically less than 10% [44, 113]. This is in agreement with the results presented here as the CTFC does not exceed 10% and follows a negative slope which is the right side of the bell curve. Figure 54 shows the difference between the rotor torque coefficient and the CTFC. Several valuable observations can be made:

Higher rotor torque The rotor torque is on average larger than the counter torque. This agrees with Equation 22.

Higher angular velocity at higher TSR Given that the separation between the rotor torque coefficient, C_t, and the CTFC is the linear term $b\dot{\theta}$, and that the viscous friction coefficient, b, is a constant; the increase in separation must be a result of an increase in the support structure's angular velocity at higher TSRs. This is apparent in Figure 55.
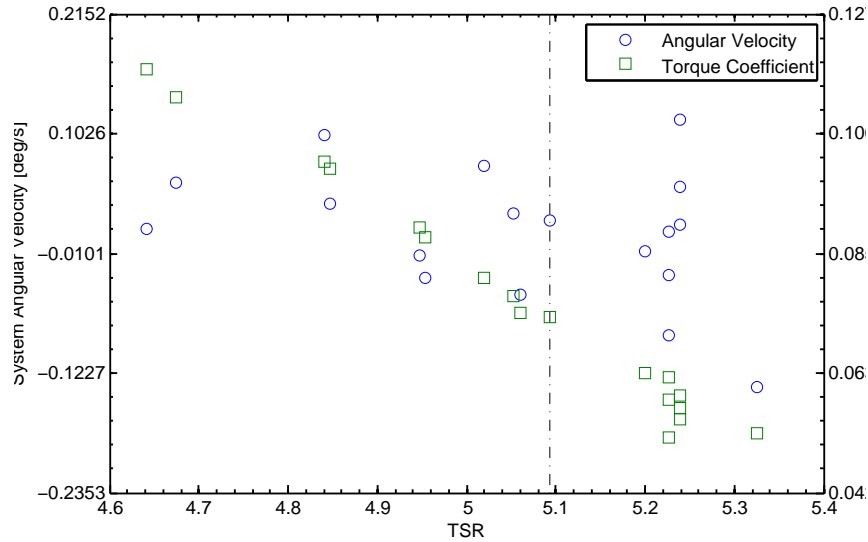
Figure 55: An increase in the RHT structural angular velocity at the lower TSRs causes an increase in the frictional torque which performs a portion of the counter-torquing necessary to keep the system stable.

Figure 55 shows the increase in the average angular velocity of the turbine structure at the lower TSRs which corresponds to the higher rotor torque. Due to the higher structural angular velocity, the viscous frictional torque compensates for a portion of the counter-torquing balance that is required. As a result there is a greater deviation between the balancing torque exerted from the counter-torque mechanism and the rotor torque as evident in Figure 54 and 42. Note the negative frictional torque indicates the average direction of rotation to be the same as the turbine rotation.

Based on the results in this section the performance of the counter-torque system follows a similar trend to that of a rotor torque coefficient yet at a linearly smaller value based on the viscous friction of the turbine system.

5.2.2   Counter-torque rotor coefficient

The CTRC defined in Equation 16 in Section 4.2, is the counter-torque non-dimensionalized with respect to the rotor torque. It is expected that the coefficient would remain at unity for the experiment since the counter-torque should always match the rotor torque. Although

due to the presence of the frictional torque in the system there is a decrease in the CTRC at lower TSRs for the majority of the experiments.

5.2.2.1   Counter-torque capacity parameter

Figures 56 to 58 presents the performance of the counter-torque system in relation to the rotor torque with varying CTC. The results of the counter-torque rotor coefficient generally have a positively sloped trend which indicates that for higher TSRs the amount of counter-torque produced is increases. This is caused by two factors which directly relate to the counter-torque produced:

1. The smaller rotor torque found at higher TSRs, evident in Figure 54.

2. The presence of the frictional torque.

Higher TSRs correspond to a lower rotor torque along with lower frictional torque, this results in the CTRC ratio to approach closer to unity as the counter-torque starts to match the rotor torque. Figures 56 to 58 have a CTRC that exceeds unity which is caused by the errors mentioned Section 5.1.1 and the influence on the performance of the generator being submerged in water. One significant factor influencing the results is the steel gears that are used in the gearbox which tend to rust after being submerged. White lithium grease was substituted for the existing lubricant in the gearbox which prevented the gears from seizing, however the influence of water on the final gearbox and electrical efficiency is unknown. Efficiency values for operating a dry motor are obtained from the data-sheet [88]. These values are used to evaluate the performance the of the generator as the as outlined in Section 3.3. Additionally, the operating range of the generator is located in non-linear regions for extended periods of time in order to capture a wider range of the power curve. Along with the influence of the environmental noise mentioned in Section 5.1.1 the rotor torque extended beyond the balancing torque provided by the counter-torque mechanism. It is recommended that a transistor current limiter be used to ensure the generator outputs current levels in the continuous torque region of its operating curve.
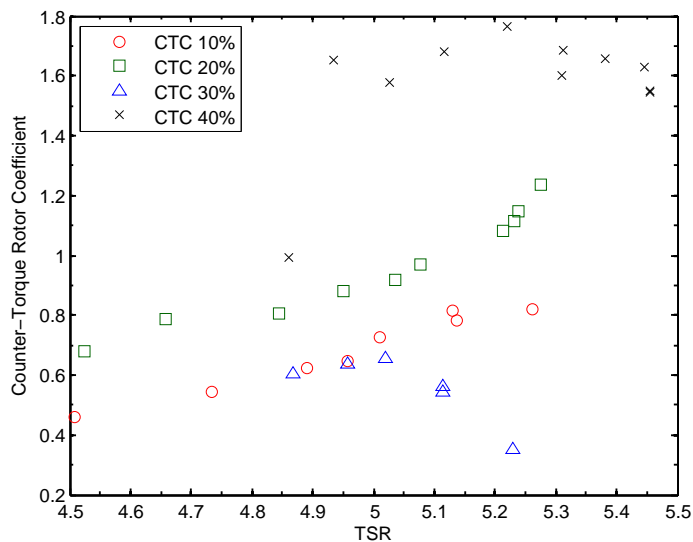
Figure 56: Counter-torque rotor coefficient at 0.788 m/s, increases with a higher TSR as a result of the smaller rotor torque and fluctuations in the angular velocity.
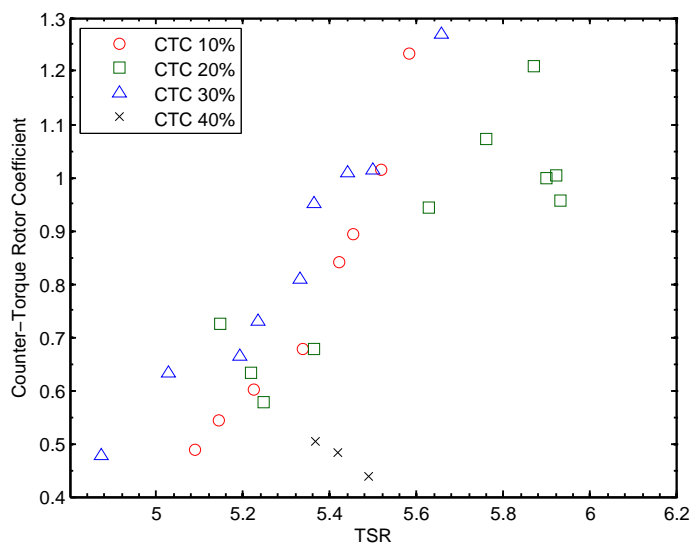
Figure 57: Counter-torque rotor coefficient at 0.875 m/s, follows the same increasing trend with no observable difference between the different CTC indicates that the increase in the counter-torque is independent of the CTC. This is expected since regardless of the contents of the buoys the same amount of counter-torque is required to balance a given rotor torque.

The original Equation 25 derives the CTRC. It is directly proportional to the counter-torque and inversely proportional to the rotor torque:

$$C_r^c = \frac{T_T}{T_r} \tag{23}$$
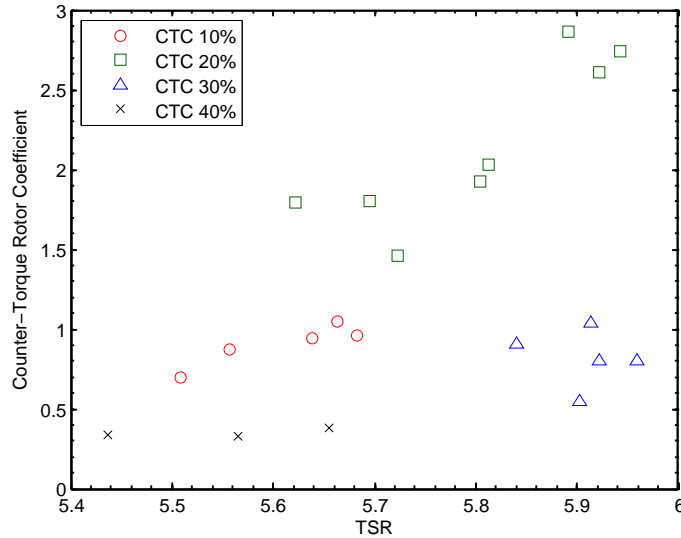
Figure 58: Counter-torque rotor coefficient at 0.963 m/s, results in a larger discrepancy between the different CTC. Higher flow velocities presented additional variability in the results due to the generator operating in non-linear regions for longer periods of time which also result in the majority of the data points to be above unity.

Recall, the total counter-torque is equal to the rotor torque less the frictional torque in the system expressed as:

$$T_T = T_r - b\dot{\theta} \tag{24}$$

By substituting Equation 24 into 23 the CTRC can be rewritten as Equation 25.

$$C_r^c = 1 - \frac{b\dot{\theta}}{T_r} \tag{25}$$

A critical observations can be made from the derived equation:

Maximum counter-torque Analytically the maximum CTRC will should never exceed one. Indicating that the counter-torque from the RHT will always match the rotor torque less any frictional torque present in the system. This is the cause of the lower CTRC at the lower TSRs shown in Figures 56 to 58.

The observation made above is further verified in Figure 59 in which adding the counter-torque to the frictional torque produces a new curve, the derived counter-torque, which lies on top of the rotor torque. The derived counter-torque has a maximum percent error of 89% and an average error of 27% when compared to the rotor torque. This validates Equation 24 in which the rotor torque is a summation of the counter-torque and the frictional torque.
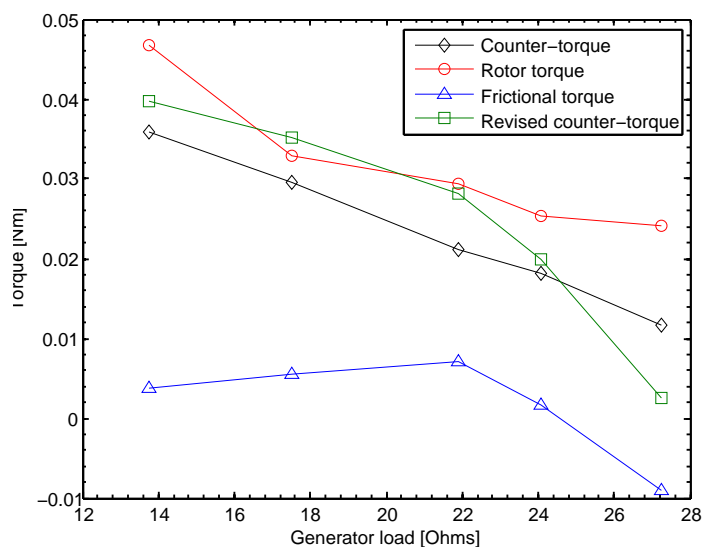
Figure 59: Plot of the various torque parameters for a flow speed of 0.963 m/s and a CTC of 30%. Note that both the derived counter-torque and rotor torque lie on top of each other.

The experimental results in Figures 56 to 58 show the counter-torque mechanism meeting the balancing torque required to keep the system stable.

5.2.2.2   Flow parameter

Figures 60 show the counter-torque non-dimensionalized with respect to the rotor torque for the three different flow velocities at each of the four CTCs. In addition to the positive slope of the CTRC, discussed in the previous section, the lower flow velocities operate at a lower TSR. The lower flow torque at the lower velocities may be the result of this as it allows the generator to operate at a lower RPM range since there is less dynamic torque induced onto it. This reinforces a similar observations made in Section 5.2.1.2. Figure 60d has a horizontal trend for the CTRC which may be a result of higher mass present in the buoys which causes

the turbine structure to stay vertical for a wider range of the TSR due to the increase mass in the heavy buoy. The inclination angle of the turbine structure is influenced not only by the rotor torque but also by the mass present in the buoys as a larger mass would result in a more vertical orientation.

(a) CTRC at 10% CTC

(b) CTRC at 20% CTC

(c) CTRC at 30% CTC

(d) CTRC at 40% CTC
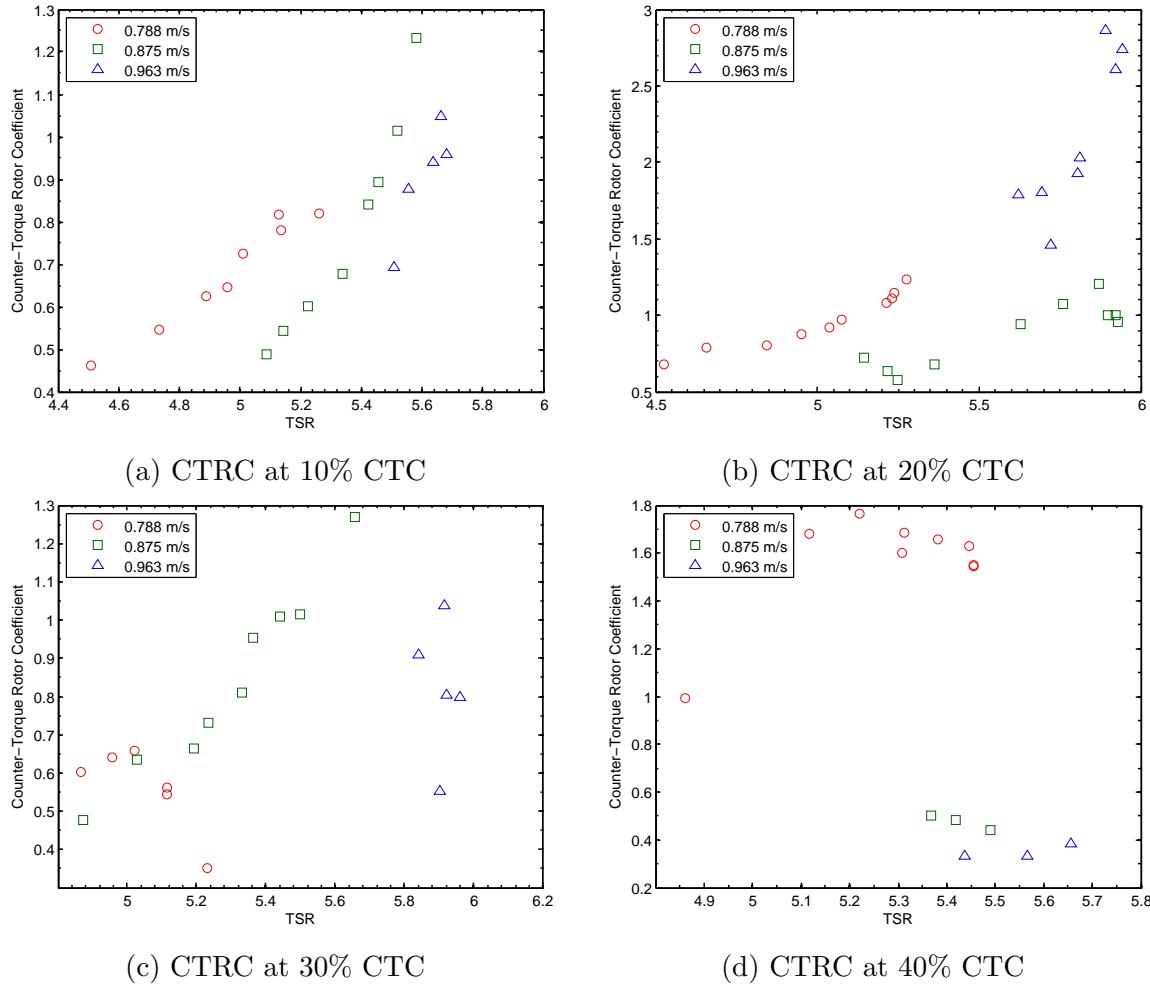
Figure 60: A positive sloping CTRC trend is consistent throughout all of the CTCs. It is described analytically in Equation 25. (a) Follows expected positive sloping trend with majority of data points below unity. (b) Note the lower CTRC for the lower flow velocities which also operate at lower TSRs. (c) Scattered data points occur due to the influence of the shift in the center of gravity of the turbine structure. (d) Significant variations in the CTRC caused by higher noise levels and turbine operating in non-linear regions of its operating conditions.

5.2.3   Power coefficient

The general shape of the power curve can be seen in Figure 61 which takes on a bell shape. At low TSRs the high angle of attack of the blade doesn't produce enough lift to extract any significant energy, resulting in a low power coefficient. Conversely, at high TSRs the drag forces dominate which reduces the torque on the rotor blade [114].
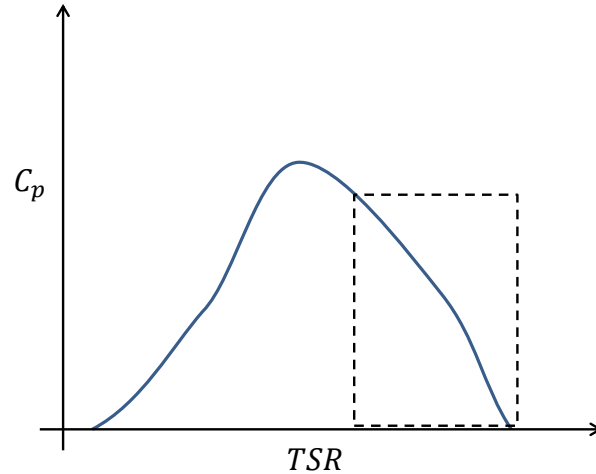
Figure 61: Operating range of the turbine is located on the right side of the power curve as illustrated in this sample curve.

Figures 62 to 64 present the power coefficients and the influence of the CTC on the power output. Comparison of the experimental power coefficients with Shahsavarifard et al. [81] provided the general range of where the plot lies. Changes in the flow velocity and its influence on the power coefficient is not presented as it has been established extensively in texts and literature [28, 114, 115]. Similar to Section 5.1 the negative slope of the power curve indicates that the operational region of the rotor blade is on the right of the power curve peak. The trends validate the independence of the power output with respect to the CTC of the buoys which is expected as the internal mass distribution and contents of the buoys have no influence on the rotor's interaction with the flow. An unintended consequence of the buoys contents may be the pitching and yawing of the turbine due to center of mass being located lower than the generator nacelle. This can be seen in the force balance diagram in Figure 22 which indicates the center of mass being located below the turbine

nacelle. As a result of this, the swept area of the rotor blades may be less than the projected area. Literature shows three possible correlations between the power output and the yaw misalignment which depends on the turbine blade design [116, 117]. The relationship has been calculated to be either $\cos(\alpha)$, $\cos(\alpha)^2$, or $\cos(\alpha)^3$, where α is the turbine yaw angle in relation to the mean flow. A yaw misalignment of $10°$ can contribute to a 1.5% loss in the best case correlation and a 4.5% loss in the worst case correlation. This factor coupled with the non-linear operating range of the generator can explain the variations in the power output for certain power coefficients. It should also be noted that blockage effects and surface effects are not considered in these results; these effects increase the power coefficient as there is an increase in the local flow velocity near the vicinity of the HKT.
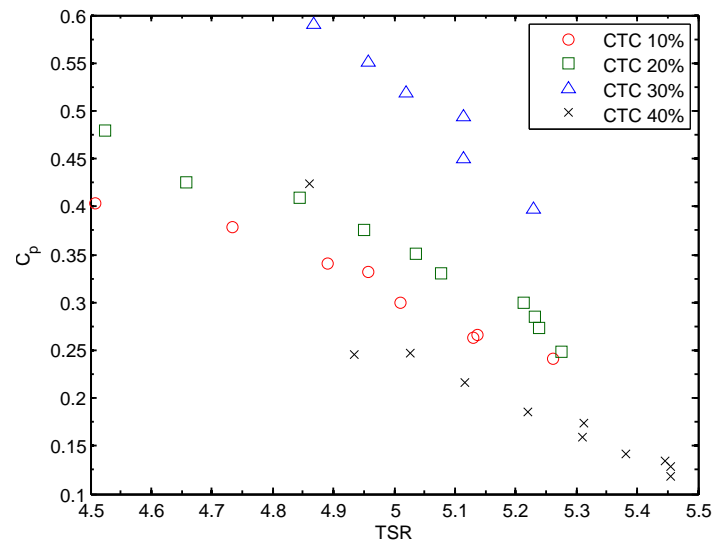
Figure 62: Power coefficient at $0.788\ m/s$ with varied CTCs. It should be expected that the power coefficient is independent of the counter-torque capacity since it does not influence the interaction of the rotor blade with the flow.
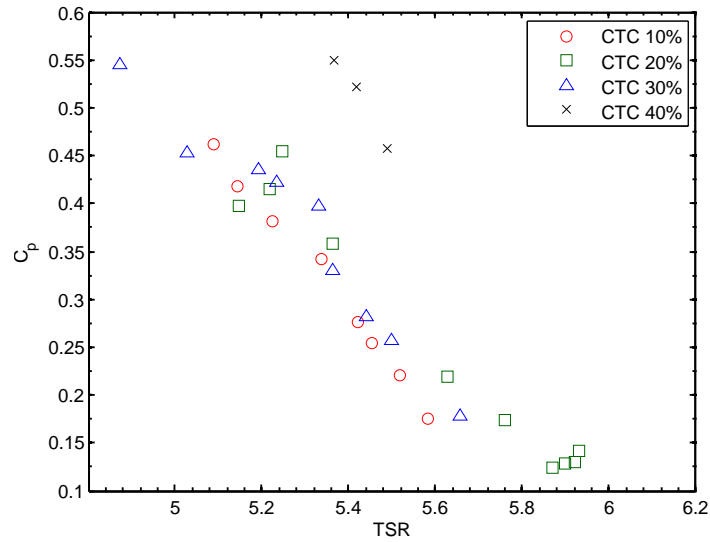
Figure 63: Power coefficient at 0.875 m/s with varied CTCs. The trends of each power coefficient lie within the same band which indicates the independence of the power output to the contents of the buoys.
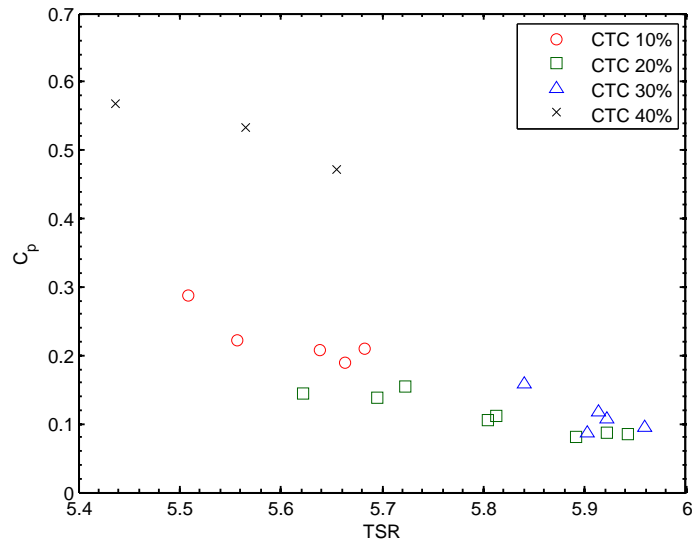
Figure 64: Power coefficient at 0.963 m/s with varied CTCs. A lower operating velocity is more ideal for the operational range of the generator being used.

5.3 Scaling parameters

The scaling parameters that influence the performance and geometry of the counter-torque mechanism and its operating condition for riverine applications include the:

Buoy volume Based on Equations 12 and 11 a linear relationship exists with the dynamic

flow torque and the volume of the buoys. The flow torque itself has a non-linear relationship with the flow velocity based on Equation 27 which indicates that the volume will increase exponentially with the flow velocity. This increase in the buoy volume can be managed by selecting a counter-torque material that has the greatest disparity from one in its specific gravity. The volume of the buoy also contributes to the drag on the buoy which is also non-linearly scaled with the flow velocity. The non-linear drag is a function of several parameters including the skin friction, the profile of the buoy, and the flow velocity.

Spoke length Increasing the spoke length will linearly increase the amount of counter-torque generated which can decrease the volume of the buoys or the density required for the counter-torque material. The minimum possible spoke length is equal to the radius of the blade with an additional clearance height to provide a factor of safety to ensure that the blade does not contact the mooring lines.

Counter-torque material The material selection for the positive and negative point masses must pass certain criteria similar to that which is applied for the small scale turbine. This includes the state of the material, its environmental impact, availability, cost, method of delivery into the cavity, and seasonal reliability. The social, economic, and non-linear relationship of the counter-torque material with the operation of the RHT makes it a critical component of the design. A material option for the light buoy is a closed cell insulator foam which would additionally provide structural support in case of impacts as well as having a low water absorption rate in case of punctures. The use sand for the heavy buoy would be viable and convenient for remote locations. Delivery and operational techniques are discussed in Section 1.2.4.

Overall turbine specific density The density of each component of the turbine must be calculated and reduced as it impacts the cavity volume needed for the nacelle ballast tank. Successful design and material selection for each component is necessary in order to ensure that the final turbine assembly will float with the given nacelle ballast. The

most critical turbine components that need to be assessed include the:

- material selection for the support structure,

- generator,

- gearbox, and

- cables.

The scaling parameters presented do not consider the turbine's performance which is influenced by factors such as the profile of the spoke, the geometry of the buoys, blockage ratio, solidity, number of blades, and clearance height of the water above the turbine. Most of these factors have been previously investigated for a wide variety of both horizontal and vertical axis HKTs [27, 118, 119, 120].

6 Conclusion and recommendations

Identified marine challenges presented in Section 1 include:

- avoid sinking surface mounted turbines due to icing;

- maximize the power coefficient of the system through optimal positioning of the turbine in the water column; and

- reduce the high LCOE of HKTs by targeting the costly deployment and retrieval procedures.

The proposed RHT addresses these challenges by incorporating a novel counter-torque mechanism with a nacelle ballast to:

Stabilize induced loads A stable operation point is passively acquired, allowing the RHT to operate at the desired power loads and in variable riverine flows. This is accomplished by

1. Two point masses located at a fixed distance from the turbine axis; under zero induced torque from the flow they are aligned vertically with the turbine axis.

2. The point masses incline with respect to the vertical axis under an applied power load.

3. The inclination of the point masses creates a moment arm which generates the passive balancing torque necessary to keep the system stable.

Operate annually Variable positions of the RHT in the water column allows it to operate annually by avoiding debris and ice formation on the water surface. This leads to a continuous annual power generation which is more predictable than established renewable alternatives such as solar or wind.

Engage in a pontoon configuration Both point masses can be configured to equally exert a positive buoyant force allowing the turbine to act as a floating pontoon during

deployment procedures.

Allow remote deployment Controlled positioning of the RHT in the water column can be accomplished remotely from shore by filling the nacelle ballast tank with water and air. This leads to reduced work labor and simplified deployment vessels which decreases the LCOE.

The counter-torque mechanism is conclusively validated through the analytical calculations, dynamic system analysis, scaled prototype design and fabrication, and experimental testing in a controlled laboratory. Table 11 outlines the research contributions.

Table 11: Design process of HKT model from analytical to experimental tests.

Stage	Description	Image
Analytical calculations	Development of the governing equations and dynamic behavior of the counter-torquing system. The loads and electromechanical requirements of the system are established in order for the RHT to operate at the maximum operating point.	
3D Modeling	Design of a 3D model must also account for the generator housing, IMU mount, cabling conduits, buoy end cap, integrated anchor points, NACA airfoil spokes, assembly procedure, and tolerances. Material properties of 3D printer are also considered for water absorption rates.	
Fabrication	Fabrication and assembly of the turbine prototype along with preliminary tests of the processing code for the IMU and data acquisition unit. Low pass filters are tested and sensor water-proofing is done. Non-dimensional metrics for quantifying the performance of the system are established.	
Experimental testing	Controlled laboratory testing in a water tunnel given the operating parameters of the water velocity, Counter-Torque Capacity, and generator load. Data collection and post processing on Matlab synchronizes data from the IMU measuring the system's inclination angle and the power output from the turbine.	
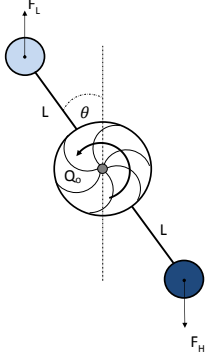
6.1   Technology readiness level

Background information into the TRL is provided in Appendix E. The project initially started at a TRL one in which the basic principles and environmental functionality of the technology are considered during the turbine deployments at Point du Bois [25] [79]. The analytical calculations of the static and dynamic operating conditions of the turbine in a laboratory environment brought the TRL to level two. Preliminary tests on wind turbine controllers, gyroscope sensors, and initial phases of the counter-torque mechanism in Appendix D brought the maturity to level three. Water tunnel testing and successful experimental operation of the small scale turbine brought the technology level to TRL four. This level integrates all of the subsystems components together in a complete laboratory scale model. The thesis provides the foundation to further advance this technology to a maximum TRL of seven by providing the required analytical model and the setup to initiate the large scale procedures.

6.2   Recommendations

Recommendations for further development of the RHT include:

1. Experimentally investigate the full range of counter-torque mechanism by varying the CTC of the buoys systematically. This requires changing the CTC of the buoys synchronously as well as individually to determine the contribution of the counter-torque from each point mass. This will verify the analytical design which indicates that only 13% of the counter-torque is derived from the light buoy while 87% is obtained from the heavy buoy when the buoy volumes are equal.

2. Development of a numerical model to assess the pressure and skin drag on various profiles of HKTs. Literature from aerostat can provide a basis as they also attempt to minimize drag while eliminating lift forces.

3. Numerically evaluate the influence of the spoke's profile on the rotor's power coefficient. Optimal profile design would provide the necessary structural support while avoiding any influence on the power generated. The parameters include the profile shape, the separation distance to the turbine, the transition profile between the spoke and the nacelle, and the position of the spoke relative to different angular positions of the turbine.

4. Experimentally investigate the influence of yawing and pitching of the turbine relative to the flow and its relationship with the $cos\alpha^3$ law for the turbine's power coefficient.

5. Investigate the operational performance of the nacelle ballast tank numerically and experimentally.

6. Design a setup to experimentally test failure procedures for the turbine's operation, including debris getting caught in the blades and emergency retrieval procedures.

Further recommended work includes a modified counter-torque mechanism in which two variable angle of attack wings attached to the nacelle provide the necessary balancing torque. Figure 65 illustrates this concept with a force balance diagram in which the average counter-torquing force is exerted from the center point of the airfoil wings.
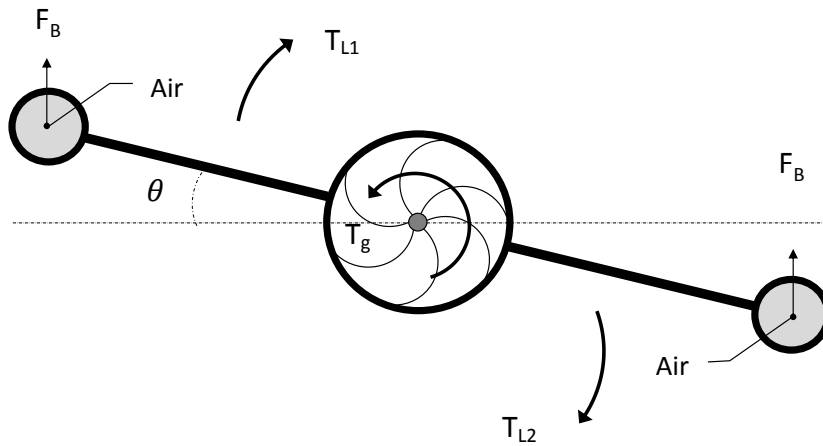
Figure 65: An alternative technique for counter-torquing involves the use of airfoils and an active feedback system. An on-board IMU detect the inclination of the system and provides the necessary angle of attack on the airfoils to stabilize the turbine at the desired inclination angle. Key difference between this system and counter-torquing buoys is that the active feedback system which requires power for operation.

References

[1] J. B. Johnson and D. J. Pride, "River, tidal, and ocean current hydrokinetic energy technologies: Status and future opportunities in alaska," Tech. Rep., November 2010.

[2] S. Kassam, "In-situ testing of a darrieus hydro kinetic turbine in cold climates," Master's thesis, University of Manitoba, 2009, Mechanical Engineering.

[3] V. Neary, M. Previsic, R. A. Jespsen, M. J. Lawson, Y. Yu, A. E. Copping, A. A. Fontaine, K. C. Hallett, and D. K. Murray, "Methodology for design and economic analysis of marine energy conversion (MEC) technologies," Sandia National Laboratories, Tech. Rep., March 2014.

[4] M. Beam, B. Kline, B. Elbing, W. Straka, and A. Fontaine, "Marine hydrokinetic turbine power-take-off design for optimal performance and low impact on cost-of-energy," in 31st International Conference on Ocean Offshore and Arctic Engineering (OMAE), April 2012.

[5] J. Conti, P. Holtber, J. A. Beamon, S. Napolitano, A. M. Schaal, J. T. Turnure, and L. Westfall, "International energy outlook 2013 with projecections to 2040," Office of Energy Analysis U.S. Department of Energy, Tech. Rep., July 2013.

[6] "Annual energy outlook 2015 with projections to 2040," Office of Energy Analysis U.S. Department of Energy, Tech. Rep., April 2015.

[7] A. Sieminski, "International energy outlook 2013 for center for strategic and international studies," July 2013.

[8] J. Balke, "Intergration of renewable energy in europe," Tech. Rep.

[9] "Levelized cost and levelized avoided cost of new generation resources in the annual energy outlook 2015," Tech. Rep., June 2015.

[10] P. Gadonneix and K. Meyers, "World energy perspective: cost of energy technologies," Tech. Rep., 2013, project partner: Bloomberg New Energy Finance.

[11] "A brief history of hydropower," International hydropower association. [Online]. Available: http://www.hydropower.org/a-brief-history-of-hydropower

[12] "Energy: Canada's energy consumption increasing," December 2012, CANSIM table 128-0016. [Online]. Available: http://www.statcan.gc.ca/pub/11-402-x/2012000/chap/ener/ener-eng.htm

[13] C. H. Centre, "Assessment of Canada's hydrokinetic power potential," National Research Council of Canada, Tech. Rep., March 2010.

[14] "Marine and hydrokinetic resource assessment and characterization." [Online]. Available: http://energy.gov/eere/water/marine-and-hydrokinetic-resource-assessment-and-characterization

[15] W. Jenkinson and A. Cornett, "Assessment of Canada's river hydrokinetic energy resources," in *International Conference on Ocean Energy (ICOE)*, November 2014.

[16] J. Khan and G. S. Bhuyan, "Ocean energy: global technology development status," Powertech Labs Inc., Tech. Rep., March 2009.

[17] "Marine and hydrokinetic technology database," United States Department of Energy. [Online]. Available: http://en.openei.org/w/index.php?title=Marine_and_Hydrokinetic_Technology_Database&oldid=878632

[18] J. Taylor, T. Kutney, and M. Knowles, "Charting the course Canada's marine renewable energy technology roadmap," Tech. Rep., 2011.

[19] W. Short, J. D. Packey, and T. Holt, *A Manual for the Economic Evaluation of Energy Efficiency and Renewable Energy Technologies*, National Renewable Energy Laboratories, March 1995.

[20] J. Thake, "Development, installation and testing of a large-scale tidal current turbine," IT Power, Tech. Rep., October 2005, contract number T/06/0021/00/REP.

[21] L. Lago, F. Ponta, and L. Chen, "Advances and trends in hydrokinetic turbine systems," *Elsievier: Energy for Sustainable Development*, vol. 14, pp. 287–296, 2010.

[22] E. Bibeau, S. Kassam, J. Woods, A. Gole, F. Mosallat, P. Vauthier, and T. Molinski, "Design of in-situ river kinetic turbines test facility in cold weather," 2006, tech. paper turbine deployment.

[23] K. Fraunkron, "Spray polyurethane foam for residential construction and code compliance," 2011.

[24] "Abrasive blasting operations: engineering control and work practices manual," Tech. Rep., March 1976, contract No. 210-75-0029.

[25] E. Bibeau, S. Kassam, J. Woods, T. Molinski, and C. Bear, "Operating a 5-kw grid-connected hydrokinetic turbine in a river in cold climates," *Journal of Ocean Technology: Renewable Ocean Energy*, vol. 4, pp. 71–82, 2009.

[26] M. J. Khan, G. Bhuyan, and J. E. Quaicoe, "Hydrokinetic energy conversion systems and assessment of horizontal and vertical axis turbines for river and tidal applications: A technology status review," *Elsevier Applied Energy*, vol. 86, pp. 1823–1835, 2009.

[27] N. Kolekar, Z. Hu, A. Banerjee, and X. Du, "Hydrodynamic design and optimization of hydro-kinetic turbines using a robust design method," in *1st Marine Energy Technology Symposium*, April 2013, washington, D.C.

[28] A. R. J.F. Manwell, J.G. McGowan, *Wind energy explained: theory, design, and application*, 2nd ed. John Wiley and Sons Ltd, 2009, ch. 3: Aerodynamics of Wind Turbines.

[29] J. K. Kladellis and D. Zafirakis, "The wind energy (r)evolution: A short review of a long history," *Elsevier: Renewable Energy*, vol. 36, pp. 1887–1901, 2011.

[30] R. Gasch and J. Twele, *Wind Power Plants: Fundamentals, Design, Construction and Operation.* Springer-Verlag Berling, 2012.

[31] "Levelized cost and levelized avoided cost of new generation resources in the annual energy outlook 2014," Tech. Rep., April 2014, U.S. Energy Information Administration.

[32] A. Stinner, "Wind energy," 2007, teaching series LCP 4A.

[33] R. Murray and P. Michael, "Review and analysis of ocean energy systems development and supporting policies," Sustainable Energy Ireland, Tech. Rep., June 2006.

[34] "Lake of the woods control board 2014 annual report," Tech. Rep., June 2015. [Online]. Available: http://www.lwcb.ca/waterflowdata.html

[35] R. F. Carlson, "Ice formation on rivers and lakes," vol. 13, 1981.

[36] A. Birjandi, S. d'Auteuil, C. Ridd, and E. Bibeau, "An innovative low cost hydrokinetic site selection technique for cold climate regions," in *OCEANS 2015 - Genova*, May 2015.

[37] "Eagle hydrokinetic turbine project," in *Alaska Tidal Energy Conference.* Alaska Power and Telephone, January 2007.

[38] "Statement of best practices for in-stream tidal energy development and operation," Nova Scotia Department of Energy and Marine Renewables, Tech. Rep., 2012, province's Marine Renewable Energy Strategy.

[39] F. M. White, *Fluid Mechanics*, 7th ed. McGraw Hill, 2001.

[40] R. T. Cheng and J. W. Gartner, "Complete velocity distribution in river cross-sections measured by acoustic instruments," California, Menlo Park.

[41] P. L. Fraenkel, "Marine current turbines: pioneering the development of marine kinetic energy converters," *Proceedings of the Institue of Mechanical Engineers*, vol. 221, 2007, part A: Journal of Power and Energy.

[42] "Seageneration project background," Marine Current Turbines LTD. [Online]. Available: http://www.seageneration.co.uk/background.php

[43] T. Hunt, "Thors power method for hydrokinetic devices," Virginia Polytechnic University, Tech. Rep., July 2012.

[44] D. Coiro, G. Troise, and F. Scherillo, "Design, towing tank test and deployment of full scale gem, a novel tethered system for harnessing tidal energy," in *Asian Wave and Tidal Energy Conference Series (AWTEC)*, November 2012.

[45] P. L. Fraenkel, "Power from marine currents," *Proceedings of the Institue of Mechanical Engineers*, vol. 216, 2002, part A: Journal of Power and Energy.

[46] P. Bachant, M. Wosnik, B. Gunawan, and V. Neary, "Experimental test plan - 1:6 scale reference model 2 cross-flow turbine," Tech. Rep.

[47] *River Hydraulics and Channel Form*, ch. 5: The nature of turbulence and velocity distributions in rivers.

[48] P. Jacobson, "Assessment and mapping of the riverine hydrokinetic resource in the continental united states," Electric Power Research Institute, Tech. Rep., December 2012.

[49] M. Gardner, S. MacDougall, J. Taylor, S. Kerr, and J. Fitzharris, "Value proposition for tidal energy development in Nova Scotia, atlantic Canada and Canada," Gardner Pinfold Consultants Inc., and Acadia Tidal Energy Institute, Technical Report, October 2014.

[50] K. Haas, H. Fritz, S. French, B. Smith, and V. Neary, "Assessment of energy production potential from tidal streams in the united states," Georgia Tech Research Corporation, Technical Report, June 2011.

[51] K. Nielsen, "Ocean energy technology systems," The Alliance for Offshore Renewables, Technical Report, May 2012.

[52] O. Edenhofer, R. P. Madruga, and Y. Sokona, "Renewable energy sources and climate change mitigation," Tech. Rep.

[53] R. Karsten, J. McMillan, M. Lickley, and R. Haynes, "Assessment of tidal current energy in the Minas Passage, Bay of Fundy," *Proceedings of the Institution of Mechanical Engineers Part A: Journal of Power and Energy*, vol. 222, pp. 493–507, March 2008.

[54] J. M. McMillan and M. J. Lickley, "The potential of tidal power from the Bay of Fundy," Department of Mathematics and Statistics, Arcadia University.

[55] H. Rogner, "World energy assessment: energy and the challenge of sustainability," United Nations Development Programme (UNDP), United Nations Report, 2012.

[56] "GDF/Alstom and EDF/OpenHydro reach the Raz Blanchard," Open Ocean, Marine Data Intelligence. [Online]. Available: http://www.openocean.fr/node/70

[57] T. J. Hammons, "Tidal power," *Proceedings of the IEEE*, pp. 419–433, March 1993.

[58] A. Babarit, J. Hals, M. Muliawan, A. Kurniawan, T. Moan, and J. Krokstad, "Numerical benchmarking study of a selection of wave energy converters," *Elsevier: Renewable Energy*, vol. 41, pp. 44–63, October 2011.

[59] S. Benelghali, M. Benbouzid, and J. F. Charpentier, "Marine tidal current electric power generation technology: State of the art and current status," *IEEE IEMDC'07*, pp. 1407–1412, 2010.

[60] T. Thorpe, "Survey of energy resources," World Energy Council (WEC), Survey, 2010.

[61] E. Lane, "Nautricity's cormat spins this way and that," 2011. [Online]. Available: http://www.greenpatentblog.com/2011/06/26/nautricitys-cormat-spins-this-way-and-that

[62] Bluewater, "Bluetec 2MW," 2009. [Online]. Available: http://www.bluewater.com/new-energy/bluetec

[63] "Evopod completes 6 months winter survival trials." [Online]. Available: http://www.oceanflowenergy.com/news25.html

[64] A. Fleming, "Aquantis ocean current turbine development project report," Dehlsen Associates and Aquantis Inc., Tech. Rep., June 2014.

[65] "Cormat," company number SC366792, Scotland. [Online]. Available: http://www.nautricity.com/cormat/

[66] J. Frith, "Deep green: the low current tidal generator," January 2015, Maritime Journal Magazine.

[67] A. Jansson, "Reflections from breakthrough marine energy trials," January 2015.

[68] Bourne, "Riverstar," Vermont, USA. [Online]. Available: http://www.bourneenergy.com/future.html

[69] Alstom, "Alstom improves the performance of its tidal energy solutions with oceade 1.4MW." [Online]. Available: http://www.alstom.com/press-centre/2014/10/alstom-improves-the-performance-of-its-tidal-energy-solutions-with-oceade-18-14mw/

[70] "Deltastream." [Online]. Available: https://www.cranfield.ac.uk/research/research-activity/current-projects/research-projects/deltastream.html

[71] W. S. Anderson, "Eco-auger product." [Online]. Available: http://eco-auger.com/our-solution/eco-auger

[72] E. Project, "Kobold vertical axis turbiner," 2011. [Online]. Available: http://tethys.pnnl.gov/annex-iv-sites/enermar-project

[73] T. Hunt, "Power control protocol for a hydrokinetic device including an array thereof," July 2012, US Patent 8,219,257. [Online]. Available: https://www.google.com/patents/US8219257

[74] "Tocardo tidal turbines," 2013. [Online]. Available: http://www.tocardo.com/

[75] F. Scherillo, U. Maisto, G. Troise, D. P. Coiro, and S. Miranda, "Numerical and experimental analysis of a shrouded hydroturbine," *2011 International Conference on Clean Electrical Power (ICCEP)*, pp. 216 – 222, June 2011.

[76] D. P. Coiro, G. Troise, and F. Scherillo, "Design, towing tank test and deployment of full scale gem, a novel tethered system for harnessing tidal energy," *Asian Wave and Tidal Conference Series*, Nov 2012.

[77] "The rite project," 2006. [Online]. Available: http://www.verdantpower.com/rite-project.html

[78] "Hydra tidal," Straum. [Online]. Available: http://www.straumgroup.com/hydratidal

[79] C. Wessner and C. Bear, "Vertical axis hydrokinetic turbines: Practical and operating experience at Pointe du Bois, Manitoba," New Energy Corperation Inc., Research Note.

[80] M. S. Guney and K. Kaygusuz, "Hydrokinetic energy conversion systems: A technology status review," *Renewable and Sustainable Energy Reviews*, vol. 14, June 2010.

[81] M. Shahsavarifard, E. L. Bibeau, and V. Chatoorgoon, "Effect of shroud on the performance of horizontal axis hydrokinetic turbines," *Elsevier Ocean Engineering*, vol. 96, pp. 215–225, 2015.

[82] "Gases-densities," Engineering Toolbox. [Online]. Available: http://www.engineeringtoolbox.com/gas-density-d_158.html

[83] *DCMS DC motor system*, Zeltom LLC, March 2011, ver. 1.3.

[84] J.-J. E. Slotine and W. Li, *Applied Nonlinear Control*. Prentice Hall, 1991, ch. 3.3: Linearization and Local Stability, p. 55.

[85] S. Kale, P. Joshi, and R. S. Pant, "A generic methodology for determination of drag coefficient of an aerostat envelope using CFD," *American Institute of Aeronautics and Astronautics*.

[86] A. D. Young, "The calculation of the total and skin friction drags of bodies of revolution at zero incidence," *Aerospace Research Council (Great Britain)*, April 1939, Reports and Memoranda No.1874.

[87] J. L. Hess and R. H. James, "On the problem of shaping as axisymmetric body to obtain low drag at large reynolds' numbers," Tech. Rep., 1975, Office of Navel Research.

[88] McMaster-Carr, "Miniature dc gearmotor," Pittman-motors, datasheet item GM8212-21-SP.

[89] S. H. Pierson, "Composite rotor design for a hydrokinetic turbine," Tech. Rep., May 2006, University of Tennessee.

[90] "Kidwind red blade set." [Online]. Available: http://www.vernier.com/products/kidwind/wind-energy/parts/kw-red/

[91] V. Crystal, "Multijet modeling materials." [Online]. Available: http://www.agile-manufacturing.com/materials/multi-jet-modeling-materials.html

[92] "Model 505 24-inch," 2011. [Online]. Available: http://www.eldinc.com/pages/Model50524

[93] M. Sadraey, *Aircraft Performance Analysis*. VDM Verlag, 2009.

[94] *DT80 Range User's Manual*, DataTaker, 2011.

[95] Arduino, "Arduino Uno," 2015. [Online]. Available: https://www.arduino.cc/en/Main/ArduinoBoardUno

[96] Thauke, *Meder electronics*, July 2012, item MK24-C-1 reed switch.

[97] "Information on MRI technique," Nevus Network, January 2005. [Online]. Available: http://www.nevusnetwork.org/mritech.htm

[98] "Stable orientation - digital IMU 6DOF + Arduino," March 2012.

[99] A. N. Gorban, A. M. Gorlov, and V. M. Silantyev, "Limits of the turbine efficiency for free fluid flow," *Journal of Energy Resource Technology*, vol. 123, pp. 311–317, December 2001.

[100] M. S. Guney, "Evaluation and measures to increase performance coefficient of hydrokinetic turbines," *Elsevier:Renewable and Sustainable Energy Reviews*, vol. 15, pp. 3669–3675, August 2011.

[101] R. Walker, "Table of density of pure and tap water and specific gravity," Tech. Rep., February 2011. [Online]. Available: http://www.simetric.co.uk/si_water.htm

[102] "Precision ball," Grainger, ANSI/ABMA Standards, Item 4RJK4. [Online]. Available: http://www.grainger.com/product/THOMSON-Precision-Ball-4RJK4

[103] G. D. Scott and D. M. Kilgour, "The denisty of random close packing spheres," *Britain Journal of Applied Physics*, vol. 2, 1969.

[104] "Evaluation of measurement data guide to the expression of uncertainty in measurement," Joint Committee for Guides in Metrology, Tech. Rep., 1995, corrected version 2010.

[105] R. Venugopal, "Bus buffers simplify design of large, noisey I2C systems," *LT Journal of Analog Innovation*, January 2013.

[106] E. Potentials, "Environmental potentials: Power quality for the digital age," EP Research and Development, Tech. Rep., March 2009.

[107] AN11084, "Very large I2C-bus systems and long buses," Tech. Rep., October 2011, rev.1.

[108] *I2C-bus specification and user manual*, April 2014, rev. 6.

[109] T. Engdahl, "Ground loop problems and how to get rid of them," 2013. [Online]. Available: http://www.epanorama.net/documents/groundloop/

[110] D. Gerke, "Mysteries of grounding," September 2002, Rocky Mountain Chapter EMC Society.

[111] R. C. Marboe, A. A. Fontaine, and T. Cawley, "Final report on instrumentation and equipment updgraes to improve acoustical and fluid dynamic measurements in the garfield thomas water tunnel," Pennsylvania State University, Tech. Rep., October 2003, technical Report 03-009.

[112] M. Khan, M. Iqbal, and J. Quaicoe, "Effects of efficiency nonlinearity on the overall power extraction: A case study of hydrokinetic-energy-conversion systems," *IEEE Transaction of Energy Conversion*, vol. 26, pp. 911–922, September 2001.

[113] H. Jiang, Z. Cheng, and Y. Zhao, "Torque limit of horizontal axis wind turbine," in *International Conference on Mechanical Engineering and Material Science (MEMS)*, November 2012, pp. 148–151.

[114] T. Burton, D. Sharpe, N. Jenkins, and E. Bossanyi, *Wind Energy Handbook*. John Wiley and Sons Ltd, 2001, ch. 3.5: Rotor Blade Theory.

[115] "Fundamentals of wind energy conversion for electrical engineers," Tech. Rep., August 2014.

[116] P. A. Fleming, A. K. Scholbrock, A. Jehu, S. Davoust, E. Osler, A. D. Wrigth, and A. Clifton, "Field-test results using a nacelle mounted lidar for improving wind turbine power capture by reducing yaw misalignment," *Journal of Physics*, 2014, conference series 524.

[117] "Yaw misalignment," March 2015, ROMOWind - Field testing.

[118] C. A. Consul, R. H. J. Willden, E. Ferrer, and M. D. McCulloch, "Influence of solidity on the performance of a cross-flow turbine," in *8th European Wave and Tidal Energy Conference*, 2009.

[119] A. H. Birjandi, D. Gaden, M. Shahsavarifard, and E. Bibeau, "Scaling-up, hydrodynamic similarity laws, and guidelines to design hydrokinetic turbines for vertical hydrokinetic turbines," NRCan, Tech. Rep., 2012.

[120] A. K. Verma, N. Garg, and T. S. Rajput, "Efficiency improvement techniques of hydrokinetic turbines: A review," *International Journal of Emerging Technology and Advanced Engineering*, vol. 5, pp. 144–151, June 2015.

[121] A. H. Birjandi, M. Goharrokhi, S. d'Auteuil, and E. Bibeau, "Resource assessment at the CHTTC site using horizontal adcp," Canadian Hydrokinetic Turbine Test Center, Tech. Rep., Septmeber 2015, CHTTC/TR-005-0915.

[122] "Winnipeg river outflow at seven sisters," Lake of the woods control board, September 2015, provisional data. [Online]. Available: http://www.lwcb.ca/waterflowdata.html

[123] "Seven sisters fall, manitoba," Manitoba Hydro, Winnipeg, Manitoba, public affairs.

[124] "Seven sister generating station," Google Earth, September 2015, 50.123762, -96.024713.

[125] W. D. Lubitz, "Impact of ambient turbulence on performance of a small wind turbine," *Elsevier Renewable Energy*, vol. 61, pp. 69–73, 2014.

[126] S. J. Chapman, *Electric Machinery Fundamentals*. McGraw Hill, 2005.

[127] E. Koutroulis and K. Kostas, "Design of a maximum power tracking system for wind-energy-conversion applications," *IEEE transactions on industrical electronics*, vol. 53, pp. 486–494, April 2006.

[128] "Everything about stmicroelectronics' 3-axis digital MEMS gyroscopes," Technical article TA0343, July 2011, rev.1.

[129] "Defense acquisition guidebook," July 2011, Defense Acquisition University.

[130] "Technology readiness assessment guide," Tech. Rep., September 2011, Initiated by: U.S. Department of Energy.

Appendix A   CHTTC

The Canadian Hydrokinetic Turbine Test Center, CHTTC, provides the opportunity for national and international hydrokinetic companies to perform deployment procedures, operational tests, and address design issues. The author has been involved in three of the fifteen turbine deployments at the site, along with several other projects which have provided first hand experience into some of the challenges currently facing hydrokinetic turbine design. Typically the nondisclosure agreements signed with the companies and the proprietary nature of their work, restricts specific data or details regarding the issues and procedures performed. Fortunately the hydrokinetic company Clean Current provided some details of their bottom mounted turbine which is used as a case study for their deployment, operation, and procedures. This will be preceded by details regarding the hydrodynamic environment of the test facility and the its available resources.

A.1   Hydrodynamic resources

The test facility compound is located approximately 1 km downstream of the Seven Sister's Generating Station. The hydrodynamic potential of the site is determined through a series of field tests conducted by Birjandi et al. [121] with a horizontal acoustic doppler velocimetry profiler and a Hummingbird's fish finder depth tracker. The site resources equates to the expected power output and can also be related to the environmental challenges experienced in the flow. The main challenges that will be investigated are icing, positioning of the turbine in the boundary layer, and safety procedures in high flow.

Birjandi et al. [121] placed a horizontal acoustic doppler velocimetry profiler at 137 cm below the water surface at three points along the channel width. Averaged velocity data every 5.6 s is collected over a minimum of 2 $mins$ for 9 transects along the water channel. The averaged data of the surface water velocities are interpolated using an unstructured mesh shown in Figure 66a, providing the flow velocity along the channel shown in Figure 66b.

(a) Unstructured interpolating mesh

(b) Flow velocity
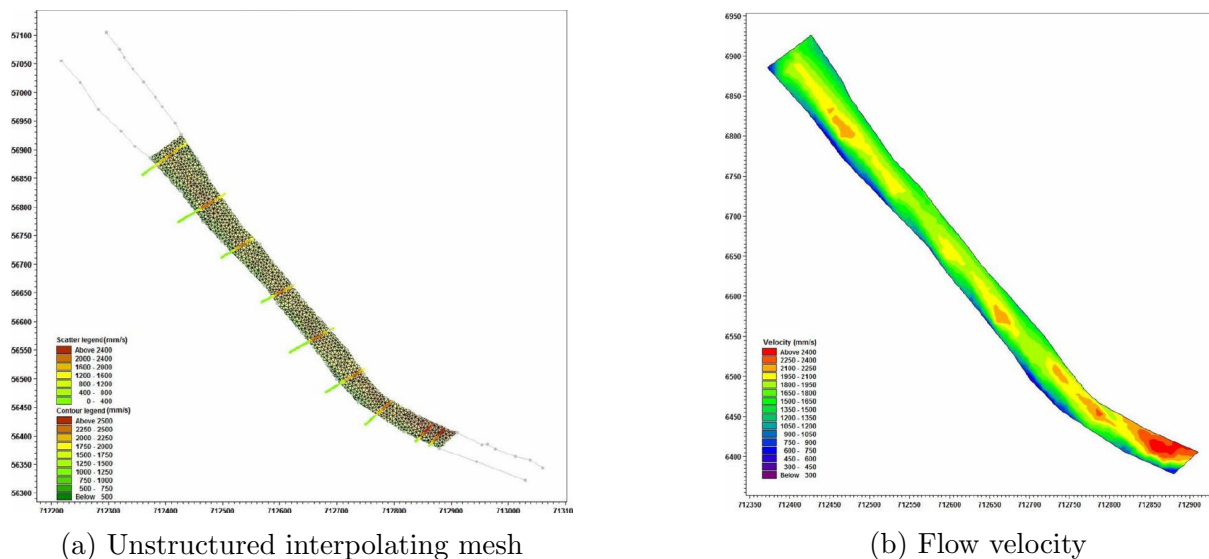
Figure 66: Resource analysis conducted by Birjandi et al. [121] for the river at Canadian hydrokinetic turbine test center.(a) An interpolating mesh created for generating a smooth flow surface profile for the 9 transects taken along the channel.(b) A maximum flow velocity of 2.62 m/s is located at the exit of the Seven sister's generating station with an overall average flow of 1.85 m/s for the day of July 14 to July 16.

The flow rate of the channel varies based on the gate controller at the generating station upstream of the testing facility and seasonal variations in the water level. Online flow rate data from the station is averaged to 1200 m^3/s for the three day site assessment conducted from July 14, 2015 to July 16, 2015 [122]. This can be used to approximate the cross-sectional area of the channel for the corresponding water level at the station. During the construction of the generating station in the 1920's the tail-race was carved into a rectangular channel which provides convenient geometry to determine its area, as well as a unique opportunity to place bottom mounted turbines and anchors onto a fairly leveled river bed [123]. The depth of the channel is measured using a Hummingbird fish finder which provided a fairly consistent 12 m along approximately 60 % of the channel length. Given the discharge rate, flow rate, and channel depth, the width of the channel can be calculated to be 54 m which falls within the range of widths acquired from satellite images at site coordinates of $50°07'25.5"N$ $96°01'29.0"W$ [124]. The agreement in the channel width confirms the validity of the measurements and site assessment performed. Based on the flow rate, the expected power density within 1 m of the channel surface can be calculated from Equation 26 to be

$3.1 \ kW/m^2$. This is not consistent throughout the entire water column due to the boundary layer decreasing in velocity closer to the river bed [39]. The hydrodynamic potential of the site is an attractive resource to establish the current testing facility in the tail-race of the generating station.

A.2   Facility resources

The testing facility compound contains two 20 ft shipping containers that house a wide range of power tools, ropes, shackles, internet accessible computers, work benches, full support equipment for two zodiac boats and two pontoons, and also grid connectivity to the local utility. Figure 67 illustrate the site facility along with the pontoon which serves as a deployment and work platform for the turbines. The site also allows accessibility for a crane which supports the deployment procedures for the turbines. The facility also allows cold climate operations with the proper survival suits, which is dangerous yet critical if hydrokinetic turbines are to be made available for year long operations. Testing of turbine maintenance, operation, and even possible deployment techniques in cold climate conditions need to be exercised and investigated in order to validate the applicability of hydrokinetic technology for northern remote communities in Canada.

One particular challenge that most surface mounted and some bottom mounted turbines encounter is the anchoring technique used to fix the structure in one point along the channel. Several different techniques are employed at the test facility including the use of shore anchors, anchor blocks for cable connection, and daisy chaining turbines together. A few of these procedures are presented in Table 12

Grid connection promotes the application of hydrokinetic turbines as well as taking the design of a turbine to the next technology readiness level. An extension line to the local generating station has made this possible for turbines being tested at the facility in which

(a) River channel

(b) Facility compound

(c) Shipping containers

(d) Inside equipment container

Figure 67: Testing facility consists of the site compound along with the entire length of the tail-race of the generating station.(a) Buoys connected to the concrete blocks on the river bed float on the surface indicating the connection points for turbines.(b) At full capacity the site can have approximately to three turbines anchored to the concrete blocks along with approximately four turbine anchored to shore with three turbines bottom mounted.(c) Two shipping containers that houses most of the equipment and facilitates as a base of operations for planning tests and turbine operations.(d) Dry storage space is critical for keeping equipment in good operating condition with proper safety regulations being met.

several of them have been designed for this operation. The only turbine that has had two successful bottom surface mounts at the site is Clean Current.

A.3   Clean current deployment

The company Clean Current designed a single rotor 12 kW horizontal axis bottom mounted hydrokinetic turbine that is enveloped with a shroud to allow for small discrepancies in the

Table 12: Shore anchors provide the advantage of using load cells for measuring drag on the turbine structure where as underwater concrete anchors provide the advantage of having all of the mooring cables concealed underwater instead of lying outside of the water posing potential danger to nearby boats and people.

Anchor Type	Description	Image
Shore	A hole is drilled into a hard rock, such as granite, to bolt down an eyelet. Epoxy glue is used to fill the bolt threads to further secure the anchor point. Problems encountered typically involved overloading the eyelet and bending the bolt due to ice build-up on the mooring lines.	
Cement blocks	Three anchor blocks each weighing six tons are placed at the bottom of the channel in order to attach cable lines for fixing the turbine's position on the water surface. Buoy are attached permanently to the cables connected to the eyelets to secure an access point to the anchor lines.	

angle of the inflow. The turbine's generator is located at the central hub which is connected directly to the rotor blades on a set of bearing; all of the power electronics are located in a trailer on shore. A variable frequency driver is used to control the tip speed ratio of the turbine which runs six 500 W light bulbs as dump loads. Two separate deployments took place with the second deployment have major overhaul work done on the base support of the turbine. An overview of the first deployment will be presented along with the challenges that were encountered with the setup.

The deployment of the 12 kW turbine took roughly one week of preparation and one full day for deployment into the channel. A description of the deployment steps is outlined in Table 13.

Figure 68: Clean current's 12 kW horizontal axis hydrokinetic turbine with shroud allows small deviations in the inflow angle.

The turbine was placed on the bottom of the Winnipeg River channel in the tail-race of the Seven Sister's generating station. One of the main challenges encountered during its operation is the decrease in its power output during winter due to the lower flow velocities that are found closer to the river bed. This is a result of the approximate logarithmic velocity profile of the flow [47] and the lower flow velocities during winter. This led to the development of the subsequent design which is based on the first turbine yet with a modified base support to allow the turbine to be placed higher in the water column. The base support is composed of two segments; one vertical column which raises the turbine approximately 5 m off the river bed, and the second which counters the bending moment experienced by the drag force on the turbine and its support structure. Maintenance procedures required the retrieval and re-deployment of the entire turbine even for small issues which required a pontoon vessel, safety boats, 4-6 personnel, and a full days worth of work. Given the infancy of the hydrokinetic industry, mechanical and electrical problems can be expected frequently; a design which provides ease of deployment and retrieval is important to be able to reduce costs and complications with the operation and maintenance of the turbine. Even though bottom mounted turbines avoid the onset of ice and debris during spring run-off, the cost, time, and safety hazards associated with removing the turbine from the flow impacts the

Table 13: Deployment procedures for the Clean Current bottom mounted turbine deployed in 2013.

Step	Description	Image
Loading	The turbine is picked up from a trailer bed with a crane and placed into a low flow region of the channel. The aluminum pontoon is aligned above the turbine which allows it to be picked up by winches.	
Delivery	The pontoon delivers the turbine to the deployment location in middle of channel waiting for cable connection from shore. Two more maneuverable boats assists in guiding of the pontoon in the fast flow as well as addressing any additional safety concerns that arose.	
Cable setup	Cable connection from a spool is dragged to the turbine position using two boats; a set of flotation buoys support the cable weight for it to lie on the water surface. Due to large drag forces on the cable, this step proved to be very difficult. Alternate methods such as deploying the cables from the turbine location may be more feasible.	
Deployment	Turbine is gradually lowered into the flow with a set of winches once the cable connections are secured. Additional buoy markers are attached to find the location of turbine for retrieval procedures. The exact positioning and orientation of the turbine are recorded afterwards using a sonar sensor.	

applications of this type of turbine.

Appendix B   Governing parameters

The operational procedure of a HKT involves the extraction of mechanical energy from a fluid flow which is then cascaded down into electrical energy through as series of conversions in which each have their associated losses. There exists a variety of different conversion systems. The specific focus of this thesis involves one such system in which the aerodynamic interaction between the rotor and the flow induces rotary motion on a shaft which is then transfered to electric energy through a DC machine. The governing equations which describes the physics behind this operation will be broken down into their subcomponents of mechanical and electrical processes.

B.1   Dynamics and kinematics of hydrokinetic turbines

The dynamics behind hydrokinetic turbines stems from the interactions between the rotor and the flow. These are governed by the aerodynamics principles which determine the operational condition of the turbine. Given that both wind turbines and hydrokinetic turbines operate in fluid flow, the governing equations that oversee them rely on the same principles [80]. In any flow condition, the mean value and the fluctuating component of the flow can be disassociated from each other and analyzed. The mean flow is predominately responsible for the mean load and mean power output, where as the fluctuating component has a higher impact on the fatigue and peak load operation [28]. Lubitz [125] showed through a series of experiments on a Bergey XL.1 1 kW wind turbine that turbulence intensities of less than 14% had a 2% reduction in the power output during its normal operating range. Conversely higher turbulence intensities resulted in an increase of 2% in the power output. Given the minimal effects of turbulence on the normal operating range of a turbine and the low turbulence intensities for the experimental setup, which will be further investigated in Section 4, the higher order statistics of the flow will not be analyzed and instead focus will be given on the mean flow and its effect on the mean power output.

Betz and Glauert performed the classical analysis of a wind turbine's aerodynamics and performance parameters in the 1930's. The power output and the thrust on an ideal rotor was obtained through a simple one-dimensional momentum theory [28]. Given the model that they used, a series of assumptions were made:

- homogenous, incompressible, steady state fluid flow

- an infinite number of blades

- uniform thrust over the disc and rotor area

- non-rotating wake

The addition of two other assumptions are made which have a more direct influence over the calculations of the power output rather than the counter-torque performance which is the main focus of this thesis. The additional assumptions made are:

- no surface effects

- negligible blockage effects

The governing equations are based on how much force is transfered from the flow onto the rotor blades which is direct relation to how much torque and power is produced. The power available in the flow, P_f, shown in Equation 26, is related to the fluid density, ρ, the swept area of the rotor blade, A, and the free stream velocity, v. Since the mean loads are of interest for this study, the average component of the free stream velocity will be used. Similarly the available torque in the flow, T_f, shown in Equation 27, is also based on the same parameters as well as the radius of the rotor blade, r.

$$P_f = \frac{1}{2}\rho A v^3 \tag{26}$$

$$T_f = \frac{1}{2}\rho A v^2 r \tag{27}$$

Based on the design and aerodynamics of the rotor blade, a fractional amount of the available power is extracted by the rotor, P_r. The ratio of the power absorbed in relation to the available power is known as the power coefficient, C_p. An empirical relationship of the non-dimensional power coefficient, known as the Betz Limit, indicates that the maximum possible power extracted by a rotor is 59.3% [28]. This occurs at the optimal operating conditions in which the fractional decrease in the flow velocity at the rotor, known as the induction factor, is exactly $\frac{1}{3}$ of the free stream velocity. By looking at the advanced stages of the wind turbine industry and the developing HKT industry, the Betz Limit greatly overestimates the power extracted by the rotor alone. A great number of experimental HKTs and operating wind turbines have power coefficient capacities ranging from nearly 25% to 40% [99] [100] [26] [44].

$$C_p = \frac{P_r}{P_f} \tag{28}$$

$$C_p = \frac{P_r}{\frac{1}{2}\rho A v^3} \tag{29}$$

Similar to the power coefficient the fractional amount of torque absorbed by the rotor, T_r, can be determined based off the torque coefficient, C_t.

$$C_t = \frac{T_r}{T_f} \tag{30}$$

$$C_t = \frac{T_r}{\frac{1}{2}\rho A v^2 r} \tag{31}$$

From the torque extracted by the rotor, the gearbox transforms the kinetic energy to a higher RPM ratio while decreasing the torque. Due to frictional losses and gearbox design, a percentage of the power inputted into the gearbox is lost. The efficiency of the gearbox,

η_g, is derived from the inputted power from the rotor, P_r, and the outputted gearbox power represented by P_g.

$$\eta_g = \frac{P_g}{P_r} \tag{32}$$

The non-dimensionalized power and torque coefficients are typically paired with the Tip Speed Ratio (TSR) which is the tangential velocity of the rotor blades non-dimensionalized with respect to the flow velocity. The angular velocity of the rotor is represented by ω .

$$TSR = \frac{\omega r}{v} \tag{33}$$

With the governing equations for the interactions between the rotor and flow established, the subsystem efficiencies for the generator can be introduced based on the electromechanical operation of the generator.

B.2   Electromechanics and motor control

After the kinetic energy of the flow has been translated into rotational energy by the turbine, an electric machine can be employed for converting the mechanical energy into electrical energy. The governing equations for the operation of the DC machine can be established based off the circuit diagram in Figure 69.
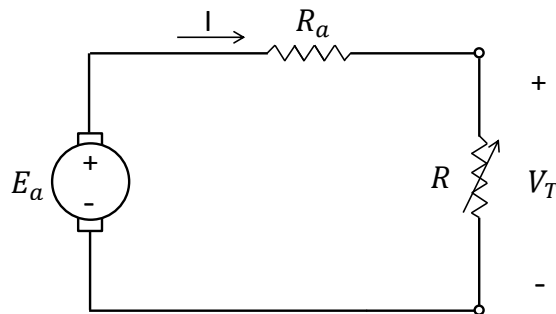

Figure 69: DC machine circuit layout

The excitation voltage of the armature, E_a, is a function of the RPM of the generator shaft, the flux of the magnets, the number of current paths, total number of conductors, and the total number of poles [126]. The current drawn from the generator, I, is a function of the armature voltage and the load applied on it, R. The resistance in the armature windings and the voltage drop across the commutator brushes are combined together to represent the total armature resistance R_a. Given the circuit in figure 69, Kirchhoff's Voltage Law can be applied to derive a simplified equation representing the motor circuit. This is shown in Equation 34 [126].

$$V_T = E_a - IR_a \tag{34}$$

With the given voltage, current, and resistance values, the electrical power output and excitation voltage can be determined along with the generator efficiency. The electrical power output, P_o, is based on the current and voltage readings from the generator shown in equation 35. The generator efficiency is the ratio of the power output from the gearbox to the power delivered to the load, this is represented by η_e. The losses associated with the generator is a function of the internal resistance mentioned before as R_a. The total power delivered to the load at can be used to determine the generator efficiency, η_e, in relation to the gear box output. This is shown in Equation 36.

$$P_o = IE_a \tag{35}$$

$$\eta_e = \frac{P_o}{P_g} \tag{36}$$

The generator efficiency can be combined with the mechanical power coefficient to produce the total water-to-wire efficiency equation shown in Equation 37.

$$P_o = C_p \eta_g \eta_e \frac{1}{2} \rho A v^3 \qquad (37)$$

A diagram representing each stage of the energy cascade, from the flow to the electrical output, is presented in Figure 20 located in Section 3.1. This section deals with the operation and control of the turbine system. Using information from the electrical output along with the mechanical performance of the generator, the electrical output torque, T_o can be determined from the output power and angular velocity of the shaft using equation 38.

$$T_o = \frac{P_o}{\omega} \qquad (38)$$

During large scale operation, HKT generators are typically custom built or ordered to match the appropriate gear ratio or flow velocity in a given marine environment. Given the scale of this project, the generator selection is done by matching the flow properties as close as possible to the available permanent magnet DC (PMDC) gear-motors available in the market. This limited the selection of motors to brushed DC motors since AC motors and brushless DC motors typically do not operate within the range of 300 to 450 RPM with torque values ranging from 0.1 to 0.2 Nm. These constraints are explained in Section 3. In order to operate a large scale HKT at an optimal point a Maximum Power Point Tracking system can be employed which uses a combination of software and hardware to incrementally vary the load on the generator until it reaches its maximum operating point [127]. The non-linear behavior of each subsystem has a minimal contributions to the efficiency of the turbine system when compared to the primary variable, the RPM [112]. It is viable to describe the entire efficiency of the system with the power coefficient which will constitute all of the electromechanical efficiencies of the system. This power coefficient will again be represented by C_p and is a function of the non-dimensionalized RPM, the TSR which is represented by the λ .

$$C_p = f(\lambda) \tag{39}$$

Due to the dimensional constraints of the RHT prototype and power requirements, a PMDC machine is used as the generator. Losses associated with a DC machine include [126]:

- electric or copper losses

- brush losses

- core losses

- mechanical losses

- stray load losses

Several advantages and disadvantages exists with the PMDC machine when compared to alternative DC and AC machines. Some of the advantages include the absence of losses associated with the field windings, and smaller sizes due to lack of rectifying circuitry. Disadvantages include the demagnetization of the poles due to armature reaction effect, and low induced torque from the permanent magnets when compared to an externally applied shunt field [126]. Each of the losses associated with PMDC machine have their own characteristic properties based on the construction and operation of the machine. Ultimately the selection of the PMDC machine is due to its viability with the operational range of the turbine system and its capacity to operate in non-linear regions for considerable periods of time.

Appendix C   Calibration

The calibration for the subcomponents for the counter-torque mechanism is outlined which include the generator, the IMU, and the DataTaker acquisition unit. Individual testing of each subcomponent is established in its relevant environmental condition for proper integration to scale model.

C.1   Generator

The Pittman DC gear-motor model GM8212-21-SP is calibrated with a drill press acting as the prime mover with a 35 Ω rheostat acting as the variable load. The DataTaker acquisition unit collects data on the RPM of the generator (monitored by a reed switch), the voltage drop across the rheostat, and the current drawn (by a shunt resistor). A K-type thermocouple operated by a MasterCraft 5N41 multimeter monitors the temperature of the generator, ensuring it does not exceed the $155°C$ maximum winding temperature [88]. Figure 70 illustrates the calibration setup. The temperature and maximum current drawn are monitored to keep operating region of the generator within its linear range based on its data-sheet.

Three different RPMs were tested on the generator by changing the belt drive on the drill press. This is shown in Figure 71 which consists of an average RPM of 234, 360, and 403 for test one, two, and three respectively. During the test, the load on the generator is decreased from 35 Ω to the lowest allowable limit based on the restrictions of the output current and maximum armature temperature. Each load is held constant for 30 *sec* which is shown in Figure 72. As the load decreases the current drawn increases which is proportional to the torque on the generator. Since the drill press output torque is higher than the generator, the RPM is held relatively constant, as a result the power drawn increases with higher torque while the RPM remains relatively constant.

The drop in the terminal voltage is due to the armature resistance which is detailed in Table 14. The higher current generated results in greater heat dissipation from the armature,
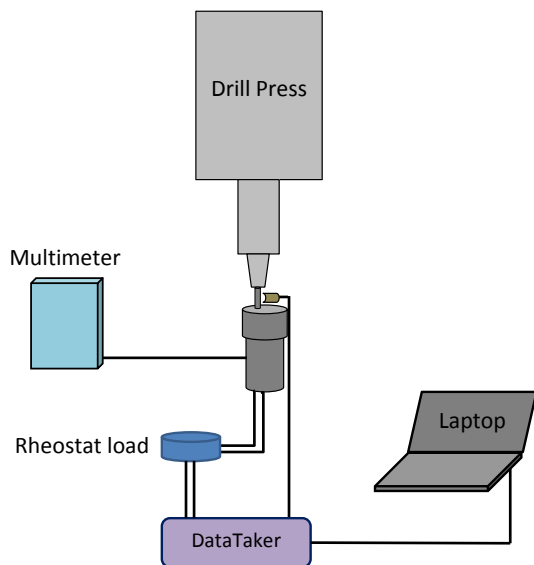
(a) Motor calibration setup

(b) Fixture with loose fit on motor

Figure 70: Motor calibration performed with stronger motor capable of sustaining RPM even when load on generator is increasing. (a) Layout of calibration with similar setup to that of water tunnel experiment. (b) Loose fitting for fixture is necessary since imperfect alignment between chuck and generator shaft causes small vibrations in motor which the fixture accounts for.

Table 14: Test cases for the Pittman motor calibration. Armature resistance is calculated based on 2 operating points as a result of the approximate linear operating region of the generator. This is later compared to the 10.8 Ω armature resistance available from motor's data-sheet.

Test case	RPM	Average max current drawn [mA]	Calculated terminal resistance [Ω]	Percent difference from datasheet
1	234	490	14	32.2%
2	360	530	16	38.8%
3	403	540	17	44.6%

the voltage drop the terminal resistance can be calculated to be approximately 15.7 Ω which is 37% off from the data-sheet's value of the winding resistance of 10.8 Ω. It should be noted
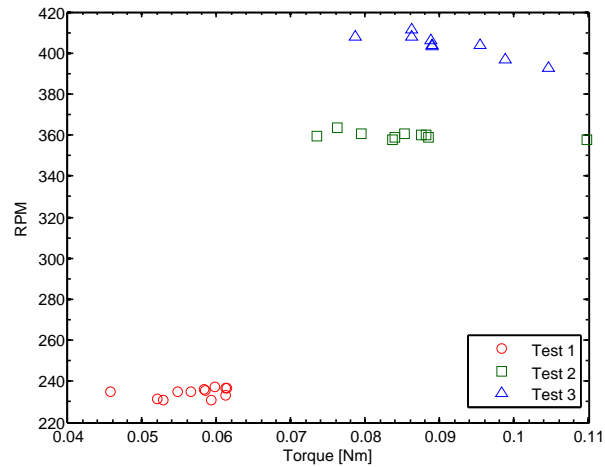
Figure 71: Generator calibration performed at constant RPM by using a stronger motor as the prime mover. Three different RPMs are tested at an average of 234, 360, and 403 for test one, two, and three respectively.
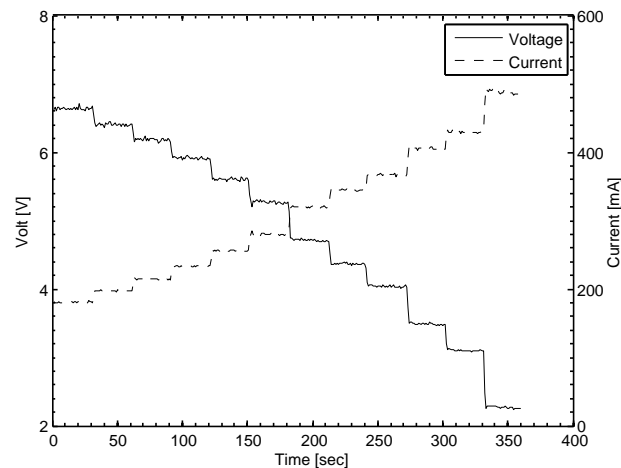

Figure 72: Voltage and current profiles for test case one. As the load on the generator is decreased a larger current is drawn which results in a larger torque extracted from the drill press. The drop in the terminal voltage is attributed mostly to the copper losses in the generator's windings.

that the drop in voltage is also partially contributed from the small deviations in the RPM of the generator which can also produce an artificially higher terminal resistance. Under ideal conditions, if the RPM is kept constant then the drop in the terminal voltage can be attributed almost entirely to the copper losses from the windings.
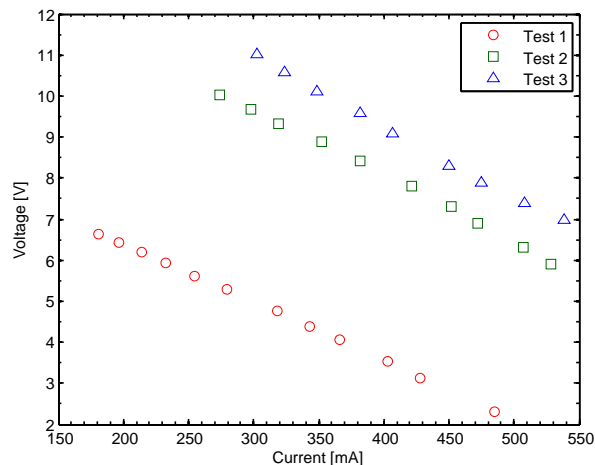
Figure 73: Different belt configurations on the prime mover resulted in three different test cases with three different torques outputted. Note the approximately linear drop in the voltage can be used to calculate the terminal resistance which is further outlined in Table 14.

C.2 Inertial measurement unit

The IMU used to measure the inclination angle of the system uses a fusion algorithm to combine the output of a gyroscope and an accelerometer to determine its inclination angle. A zero rate calibration is performed at the beginning of each initialization of the program which involves keeping the sensor leveled and stationary while 100 data points are measured. This establishes the filter threshold for the program to use as the minimum required angular acceleration to record valid changes in its angular position [128]. Changes in temperature can cause a drift in the zero rate output which can be compensated for by using a moving average filter which could not be implemented for this application as it requires the IMU to be stationary in the middle of operation for recalibration. Calibration of the zero rate angular velocity is conducted once at the beginning of each test.

C.3 DataTaker

The data acquisition unit has an on-board diagnostic tool which is conducted before each test. The diagnostic involves a self-calibration which is followed by testing the internal memory backup, the voltage and current supplies of the on-board battery, and the minimum voltage

response of each of the input pins. During operation the pins are measured periodically for their internal voltage offsets which is influenced by temperature changes. The offset is adjusted into the readings of the pins which allows for a more accurate representation of the pin's voltage readings [94].

Appendix D   Design process

During the design process alternative concepts were investigated for their applicability in providing the counter-torque required to stabilize the single rotor turbine. One of these concepts involved using air as the sole means of counter-torquing the rotor. This would require a much longer moment arm due to the smaller specific gravity of air when compared to stainless steel. The buoyancy force of the air would provide the required counter-torque to stabilize the turbine during operation. Figure 74a illustrates the free body diagram of the model with a closed tube around the turbine which would be filled with water and a small amount of air. A check valve is used to supply air into the tube and an exit hole allows for the water to be displaced out of the tube. The tube is blocked off half way to constraint the air to one part such that at greater inclination angles the moment arm increases. The benefit of this design is in its use of air as the only means of counter-torquing which can be readily supplied by an air line extended to the turbine underwater. The deployment and retrieval of the turbine can be controlled remotely by placing an electrically controlled valve on the tube exit which would allow the control of water and air. During retrieval the air supply line coupled with the power conduit would fill the entire tube with air to raise the turbine from the water column, water inside the tube would be forced out from the high pressure air. During deployment, air would be evacuated out of the tube and water would be allowed to fill the space which would increase the system's overall density and descent the turbine into the water column. A bridle connection would be join three mooring lines from the tube to tether the turbine in the flow. A ball joint at the bridle would allow the turbine to rotate 360° in case of failure if the counter-torque is insufficient to balance the torque on the rotor. The conceptual design operated successfully during testing although the zero counter-torque test was not successfully passed. This test involved removing all of the air in the tube and allowing the system to rotate freely when the torque on the rotor shaft was increased. This test was not successful as the system remained in equilibrium even without any air in the tube. Further investigation into the operation of the system indicated that the generator

being used for this prototype absorbed an insufficient amount of torque from the flow and thus did not require any significant counter-torque to keep it stable. This design allowed for further investigation into the requirements of the DC machine and the corresponding torque output the generator is required to have for extracting the appropriate amount of torque from the flow.
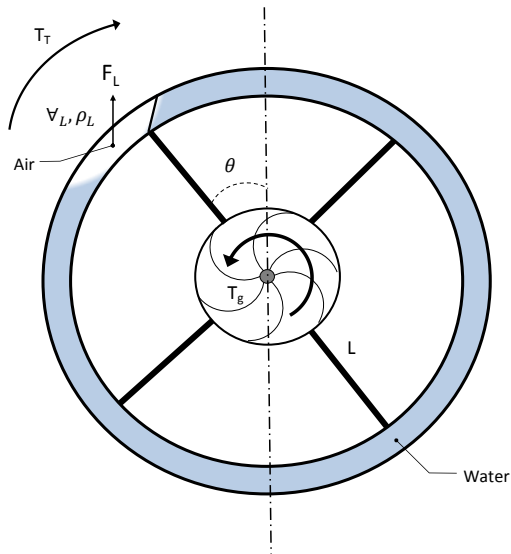
(a) Force balance for prototype one
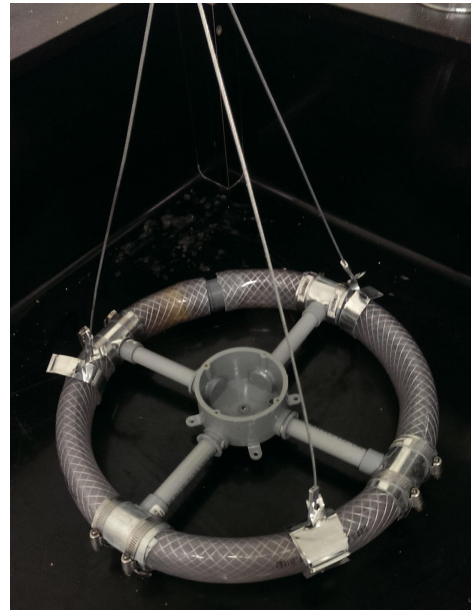
(b) Photo of initial prototype

Figure 74: The first prototype designed consisted of only a single closed tube with a blocked off inner section to capture air in one side of the tube. (a) Due to the lower specific gravity of air compared to stainless steel, a longer moment arm L is required. (b) The central cavity serves as a fixture for the generator.

Appendix E   Technology readiness level criteria

The TRL is a one dimensional metric established by NASA in the 1980's which helps to assess the maturity of a project [129]. It was later adopted by the Department of Defense and the Department of Energy in U.S.A. to ascertain if a project or technology is ready to be implemented into their department. The metric that was modified by the Department of Energy will be applied to this thesis to quantitatively determine its contributions.The criteria for the Technology Readiness Level outlined by the Department of Energy in [130] has 9 levels of maturity. Level one being the basic principles of the technology established, to level nine being complete implementation of the project in a full scale environmental setting. Table 15 demonstrates the metric criteria and the description of the maturity at each level.

Level	Definition	Description
TRL 9	Full system operation in expected environmental conditions.	Technology is in its completed form and operates at full capacity with all of the intake and waste products normal to its operation.
TRL 8	Final system completed with demonstration testing completed.	Technology is in full working order with almost all test cases demonstrated and functional. Evaluation of system performance and waste management is also set.
TRL 7	Full-scale prototype functional in relevant environment.	Commissioning of actual system in relevant environmental scenario with simulated physical inputs prior to full testing. Final design is virtually complete.
TRL 6	Complete testing of prototype in similar environmental conditions	Development of prototype and testing of scaling parameters for establishing functional design components for large scale application.

Level	Definition	Description
TRL 5	Approximate prototypical scale model and developed testing	Subsystem components compiled together and established testing in relevant environmental laboratory conditions with functional outputs and waste.
TRL 4	Preliminary scale model with initial testing in laboratory	Initial scale testing of proven scientific concept with experimental results indicating difference between numerical, analytical, and experimental results.
TRL 3	Proof of concept and finalized design of prototype	Individual subcomponents are tested independently for validity for eventual integration into scale model.
TRL 2	Conceptual idealization	Support and references for conceptual idea is established and basic principles of operation is observed in similar concepts.
TRL 1	Basic principles	Initial studies into concept and preliminary investigations into governing principles and equations. Basic paper trails of ideas and progress is tracked for eventual prototype.